IMAGING THE SPATIOTEMPORAL EVOLUTION OF INJURY-INDUCED DYSFUNCTION IN ARTICULAR CARTILAGE

A Dissertation
Presented to the Faculty of the Graduate School
of Cornell University
in Partial Fulfillment of the Requirements for the Degree of
Doctor of Philosophy

by
Lena Renee Bartell
May 2018

For him that stealeth a Book from this Library, let it change to a Serpent in his hand and rend him. Let him be struck with Palsy, and all his Members blasted. Let him languish in Pain, crying aloud for Mercy and let there be no surcease to his Agony till he sink to Dissolution. Let Book-worms gnaw his Entrails in token of the Worm that dieth not, and when at last he goeth to his final Punishment let the Flames of Hell consume him for ever and aye.

– Pearson, E. *The Old Librarian's Almanack*. (1909).

IMAGING THE SPATIOTEMPORAL EVOLUTION OF INJURY-INDUCED DYSFUNCTION IN ARTICULAR CARTILAGE

Lena Renee Bartell, Ph.D.

Cornell University 2018

Articular cartilage is a fascinating biological material wherein a careful balance of mechanical and biological homeostasis ensures healthy joint function over decades of normal loading. Injurious loading, however, can upset this balance, inducing cartilage's chondrocyte cells to dysfunction and leading to both the degradation of the tissue and, ultimately, the debilitating joint disease osteoarthritis. Understanding how injury causes dysfunction is important not only for understanding disease pathogenesis, but also for targeting treatments to protect and preserve cartilage. Previous studies have explored both the mechanical and biological deterioration of cartilage after injury, observing cracks in the extracellular matrix and a complex wave of cellular responses, including respiratory dysfunction and death. However, many open questions remain regarding the link between injury mechanics and cartilage dysfunction. In the first part of this thesis, I explore the spatiotemporal evolution of cellular dysfunction after impact injury in order to relate this dysfunction to the mechanics of injury and elucidate promising therapeutic targets. First, I present a custom impact device to injure cartilage explants while interfacing with microscopy. Analyzing such imaging data, I found that injury induces a wave of mitochondrial dysfunction within 15 minutes of impact and cell death within 3 hours. Both measures are highly correlated with the local strain experienced during injury, showing that injury mechanics dictate peracute cellular dysfunction. Consequently, cartilage's compliant surface layer may serve to protect underlying cells by absorbing excess strain. Remarkably, I also found that treating samples with the mitoprotective peptide SS-31 completely eliminated the strain-dependent mitochondrial dysfunction after impact. These results have important clinical implications for understanding the very first changes in cartilage after injury and targeting these responses with clinically-relevant treatment. In the next part of this thesis, I explore one commonly-observed form of mechanical deterioration induced by cartilage injury: cracks. In particular, I present a method to indent cartilage with a sharp blade while simultaneously tracking bulk and local mechanics. Results showed significant dependence across physiologically relevant rates and were modified by cartilage's layered structure. Taken together, this study highlights the importance of rate and inhomogeneity in governing cartilage failure and suggests important parallels between failure in cartilage and in high-toughness double-network hydrogels. Finally, I close by exploring spatiotemporal mechanics and indentation failure in an entirely new system: protective glass coatings. Tracking embedded fiducial markers in polymeric coatings with rapid 3D confocal videos, I show that incorporating nanosilica beads in the coatings modulates their adhesion and indentation response, with important implications for their ability to protect the underlying glass. Overall, this thesis champions the utility of imaging in concert with spatiotemporal analysis in order to relate the complex mechanical behavior of a system, such as articular cartilage, to its function and dysfunction.

BIOGRAPHICAL SKETCH

Lena Bartell was raised in Lyndell, PA and attended school in the Downingtown Area School District, where she graduated from high school in June 2007. Enjoying math and physics, she pursued her bachelor's degree in Physics in the Schreyer Honors College at Pennsylvania State University. While at Penn State, Lena worked in Professor Doug Cowen's lab, part of the IceCube Neutrino Observatory project. Through the AAPM fellowship program, Lena also studied X-ray dosimetry with Professor Andrew Maidment in the Department of Radiology at the University of Pennsylvania. Lena then spent a semester abroad at Victoria University in Wellington, New Zealand before graduating from Penn State in May 2011 with Honors in Physics and minors in Math and Biomedical Engineering. Lena continued her education at Cornell University where she is currently pursuing a PhD in Applied Physics, with a minor in Biomedical Engineering. Beyond science, Lena enjoys outdoor activities, especially backpacking, and sharing a beer with friends.

To Mr. Hopson & Mrs. Spano, who inspired me

To Dr. Robinett & Dr. Maidment, who saw the best in me

To friends old and new, who strengthened me

To Mom, Dad & Harry, who never doubted me

and most of all

To Jason, my love, my rock, my partner-in-crime

ACKNOWLEDGMENTS

Funding sources for projects are acknowledged within each chapter, but I would like to extend special thanks to the Cornell Presidential Life Science Fellowship, the NSF Graduate Research Fellowship Program, and the NIH F31 Fellowship Program for their generous support during my graduate career.

Beyond funding, my education at Cornell was shaped by many talented, brilliant, and kind people without whom I would not be the scientist or person I am today. It is perhaps impossible to acknowledge all the individuals that have influenced my education and life over the past years, yet try I will:

First, I would like to acknowledge the continuous support, constructive criticism, professional mentorship, and scientific inspiration I received from Profs. Itai Cohen, Lawrence Bonassar, Warren Zipfel, and Lisa Fortier. Together, these talented professors provided me with a more diverse, holistic, and enjoyable graduate education than I ever hoped for. To Itai: thank you for being open minded, for encouraging me to value communication, and for pushing me to be independent. To Larry: thank you for training me to craft meaningful hypotheses and for welcoming me into your lab with open and honest collaboration. To Warren: thank you for fostering my love of imaging and providing a playground in which to learn more about it. To Lisa: thank you for not only exemplifying a strong, smart, and successful woman, but also for your words of affirmation along the way.

To every member, past and present, of the Cohen, Bonassar, Fortier, and Zipfel labs: Thank you for your guidance and camaraderie. Your acceptance across campus and across disciplines has made my education richer and my life fuller. In the Cohen lab, to Brian Leahy: thank you for expanding my world of knowledge, for helping solve so many of my problems, and for all the drinks and baking competitions we shared along the way. To Meera Ramaswamy and Sam Whitehead: thank you for listening to my ideas, commiserating, and inspiring me to work harder. To Monica Xu and Thomas Wyse Jackson: thank you for joining the cartilage project; it was both more successful and more enjoyable for your presence. To Yunus Kinkhabwala, John Mergo, and everyone else: thanks for your friendship and support; our discussions within lab and without kept me on-track and sane. In the Fortier lab, to Michelle Delco: thank you for reminding me how impactful science can be and for encouraging the best in me. In the Bonassar Lab, to the cartilage mechanics crew, especially Eddie Bonnevie, Chris DiDomenico, Alex Boys, Jill Middendorf, and Becka Irwin: thank you for sharing my love of biomechanics and accepting me into your group. To my conference and hiking companions, Mary Clare McCorry, Katie Hudson, Chris, Alex, and Jill: thank you for all the trips we shared, both in conference centers and on hiking trails; life's more fun if you climb a mountain every now and then! To Corinne Henak: thank you for your mentorship and for being my role model, both as a scientist and a person.

I would also like to thank all the staff I interacted with at Cornell for their technical and personal support, especially Cynthia Reynolds, Nate Ellis, Jonathan Fuller, Todd Pfeiffer, Susi Varvayanis, Lynn Johnson at the Cornell Statistical Consulting Unit, and the BRC Imaging staff, especially Becky Williams.

To my D-town crew, especially Katharine Schor and Rosalind Hayes: Thank you for your friendship and cheerleading; whether near or far, we always have each other, and your strength continues to inspire me. To my “Fallen Creek” family, Greg Stiehl, Summer Saraf, Ed Lochocki, Coralie Salesse-Smith, Evan MacQuarrie, Eamonn O'Shea, Sam Ahles, and Jessica Abueg: What can I say? It has been fantastic and hilarious and humbling and insane and I have loved every minute.

Last but not least, I’d like to thank my family. To Rod, Kathy, and Nathan Bartell: Thank you for welcoming me into your family. Your support has strengthened me and I have learned so much from each of you. To my grandparents, Tudor and Laura Bradley, and Anthony DiEgidio: Your pragmatism, generosity, and strength inspired me. I miss you every day and wish I could thank you in person. To Harrison Bradley: You have always been and continue to be my role model. You are brilliant and kind and I strive every day to live up to your example. To Mom and Dad: All I am today is because of your love and endless support. You have always believed in me, unfailingly, even at my worst. Thank you for all you have done to give me the life I have had the privilege to lead. And finally, to Jason Bartell: I cannot begin to thank you for all the ways you have saved me, enriched my life, and inspired me to be a better person. Suffice it to say, I simply would not have survived without you. Thank you for making this chapter of our story so wonderful – one of many more to come.

TABLE OF CONTENTS

LIST OF FIGURES

LIST OF TABLES

CHAPTER 1. INTRODUCTION

1.1 Guide to the thesis

At its heart, science is an observation and a curiosity. No matter the specialty, the goal has always been to understand this world and the principles that guide it. The five senses, however, are rarely adequate devices in the pursuit of knowledge - human eyes cannot see infrared light or observe organelles in a cell. The challenge of the modern scientific pursuit, then, is to observe the unobservable. Each experiment has the opportunity, if not the duty, to enhance our senses, revealing a unique perspective on nature and the universe. It is not until we can see our world in a new light that we open the door to learn more than ever before. This search for innovative perspectives has proven to be the fundamental truth driving my education and fascination with the world, and it is the guiding principal connecting the works presented here.

Stated one way, the focus of this thesis is to develop and utilize novel techniques for visualizing mechanical behavior, especially in inherently multidisciplinary systems where such mechanics are central to the system's function and dysfunction. In particular, the chapters below present multiple related approaches that synthesize imaging modalities with other core ideas in the system at hand in order to broaden our understanding of what drives that system towards success or failure.

In the first part of this thesis, Chapter 2-Chapter 4 explore the interplay between mechanics and biology that underlies the development of injury-induced joint deterioration and disease. Here, the system of interest is the articular cartilage tissue within mammalian joints that lines the end of long bones, dissipating load and providing a low friction surface for joint motion[1]. The physiologic health and stability of articular cartilage relies on a fascinating interplay between the mechanical behavior of the tissue and the biological homeostasis of its embedded cells, known as chondrocytes[2]. Indeed, traumatic mechanical disruption – such as a sports injury that causes an ACL tear – upsets this careful balance and can induce a downward spiral toward the common and debilitating joint disease osteoarthritis[3–5]. In these three chapters, we develop and present methods that enable us to directly probe the complex relationship between mechanics and biology in articular cartilage at a newfound level of detail, especially in the immediate aftermath of an injury, where cartilage damage and deterioration are poorly understood[2–6]. Stated shortly, we explored the question “What goes wrong first?” after traumatic cartilage injury.

In the second part of this thesis, Chapter 5, we move beyond the world of cartilage biomechanics to explore mechanics in a new system: protective glass coatings[7–10]. Broadly, this chapter highlights the versatility and utility of imaging data for understanding the detailed interplay between damage and mechanics, even outside of biological systems. Specifically, we present a method for tracking the microscale flow of polymer coatings on glass in order to understand their 3D flow and time-evolution during indentation. In collaboration with Corning Incorporated, we applied this method to explore the differences in behavior between two formulations of polymer coatings that may be used to protect glass in real-world applications. In particular, we embedded fluorescent particles into the coatings and used these spheres as fiducial markers to track the 3D microscale strain and stress in the coatings during traditional Vickers indentation testing. Comparing the two coatings, we observed important differences in slip at the coating-glass interface which may influence their fundamental ability to absorb load and protect the underlying glass from damage. Moreover, this method provides an experimental complement to the existing theoretical and modeling approaches for studying indentation in layered systems[11–15].

Overall, in this thesis we develop and apply novel methods to explore the spatiotemporal interaction between mechanical injury and biological dysfunction in articular cartilage disease, as well as the spatiotemporal behavior of coatings used to protect glass surfaces. By using these methods, we reveal a unique perspective on what drives these systems – articular cartilage, protective glass coatings – toward success or failure, whether in your knee or on your mobile phone.

1.2 Articular cartilage and injury-induced dysfunction

The joint disease arthritis is a major healthcare problem that causes pain and disability in 23% of adults. Osteoarthritis (OA) is the most common form of arthritis which affects about 10% of adults in the United States, with a growing prevalence as the population ages[16,17]. Often, OA develops after an injury such as a sports injury or car accident, and in those cases is referred to as post-traumatic OA (PTOA)[3]. One hallmark of joint damage and disease, including OA, is the degradation and loss of the smooth articular cartilage tissue that lines the ends of bones in diarthroidal joints, dissipating load and facilitating joint motion[18]. However, there is no cure or effective treatment for OA and many open questions remain regarding the pathogenesis of injury-induced cartilage damage.

Cartilage tissue is composed of relatively few cells surrounded by an extracellular matrix (ECM) which has a complex double-network structure that also has depth-dependent anisotropy and inhomogeneity[1] (Figure 1.1, Figure 1.2). The first network of the ECM is composed of collagen fibrils (primarily collagen II) which are covalently bonded to form a network that can withstand tensile forces. The second network is composed of proteoglycans entangled in the collagen network. These proteoglycans are highly charged and thus resist compressive loads. These charges also draw in fluid and ions which provide further compressive support and establish an additional poroelastic behavior in cartilage[19–21]. In particular, cartilage volume changes require fluid flow and there is an associated poroelastic timescale required for this flow that depends on both the porous structure and the geometry of the sample and loading environment. In addition to this network structure, cartilage tissue has depth-dependent anisotropy and inhomogeneity. Within the first 10-50 µm of the articular surface, collagen fibrils are preferentially aligned in-plane, with an additional in-plane alignment known as the split-line pattern[22–24]. Below the surface, in the intermediate tissue, the collagen network is more randomly aligned. In mature cartilage, collagen fibrils in the deepest part of the tissue near the bone are preferentially aligned perpendicular to the bone. Separately, cartilage also exhibits depth-dependent material properties. In particular, the first 250-500 µm, known as the surface layer of cartilage, is much more compliant than the bulk of the tissue, both in compression and shear[25,26]. In addition to its complex material structure, cartilage also functions as an important tissue in joints. Unlike many other tissues, cartilage is composed primarily of ECM with relatively few embedded cells, known as chondrocytes. These chondrocytes are important for producing and maintaining the surrounding ECM. They also respond to their mechanical loading environment, with healthy responses to normal loads but adverse and detrimental responses to excessive or injurious loads[5,27].

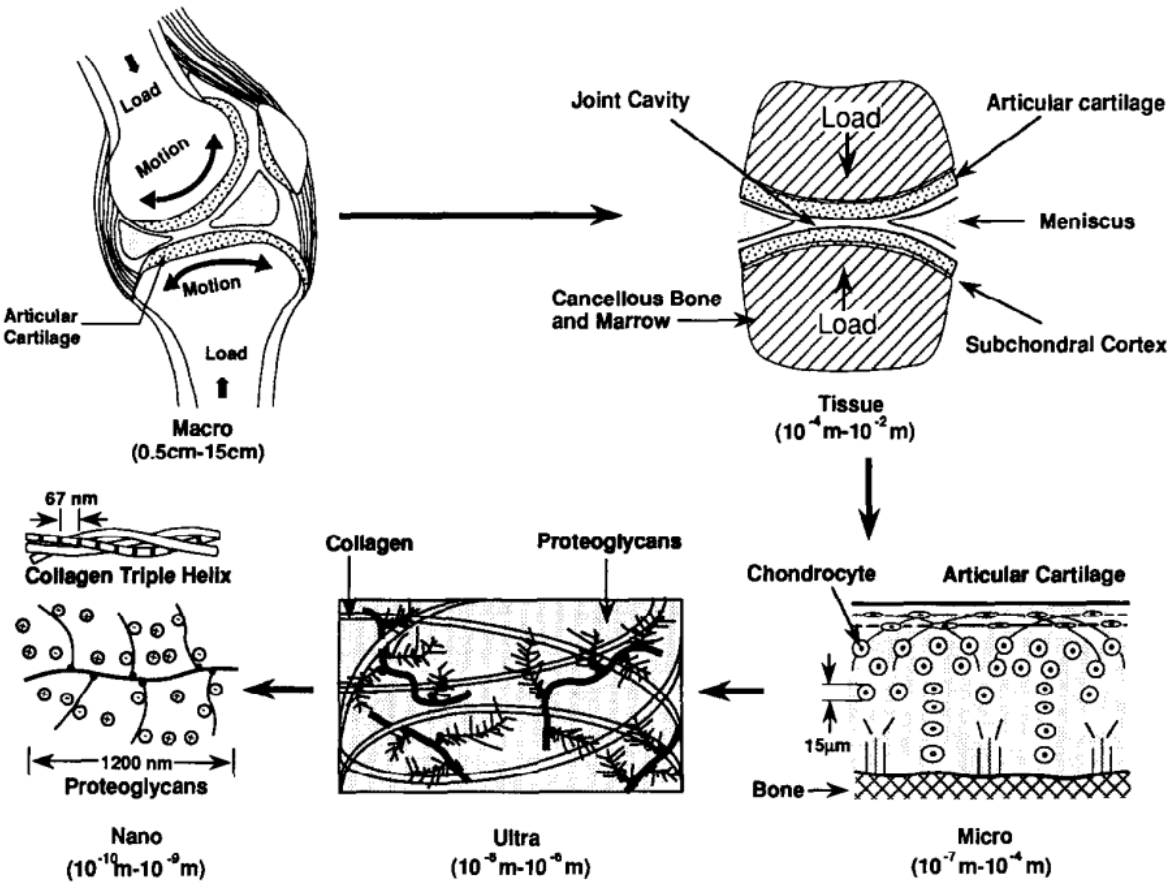

Figure 1.1. Some of the important structural features found in a typical joint and the relevant length scales. Copied from Mow et al. 1992.[1]

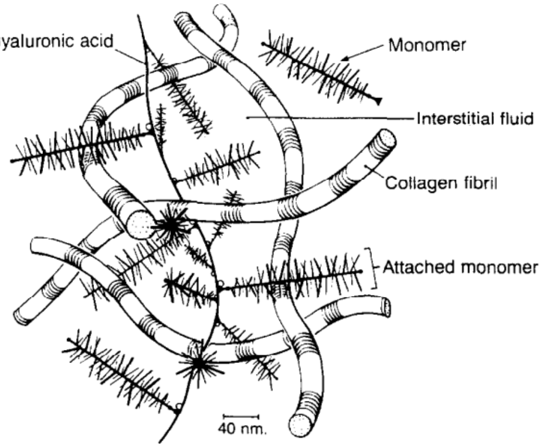

Figure 1.2. The collagen network interacting with the proteoglycan network in the extracellular matrix forming a fibre-reinforced composite. Copied from Mow et al. 1992.[1]

In general, joints experience a wide range of loading rates, and an even wider range of time scales are relevant for cartilage injury and disease. During normal, physiologically-relevant loading, cartilage must withstand loading rates ranging from rapid loading during exercise (e.g. running ~4 Hz) to static loading during other activities (e.g. sitting ~0 Hz). Moreover, injurious loading must be super-physiologic to be considered an injury and thus usually involves even faster loading rates, ~1000 Hz or ~10^{-3} s[28]. However, traumatic joint injury may not develop into osteoarthritis for many years after injury (~10^{9} s), leaving many decades of time scales that are relevant for understanding PTOA. While much is known about the later stages of joint disease, relatively little is known about what occurs in cartilage during and immediately after an injury and there are few techniques to observe the relevant phenomena on these time scales.

Joint injury and disease induce many mechanical and biological changes in articular cartilage. In the later stages of osteoarthritis, cartilage tissue has worn away from the surface, either particular or entirely, and the tissue often develops fractures and fissures in the surfaces[5]. Moreover, the chondrocyte cells exhibit widespread apoptosis and induce matrix degradation and associated loss of material properties. In cartilage, the current understanding is that injurious loading induces a complex wave of responses over the days and weeks after an injury, including necrosis, apoptosis, inflammatory signaling, and anabolic and catabolic responses[2] (Figure 1.3). However, studies have not extensively explored the evolution of ECM and chondrocyte changes in cartilage in the peracute timeline after an injury (minutes-to-hours). Moreover, no studies have explored the microscale deformation of cartilage tissue in responses to such a fast, injurious loading. As such, many open question remain regarding how injury mechanics affect biological function, what goes wrong first, and to what degree we can predict or prevent or treat such damage.

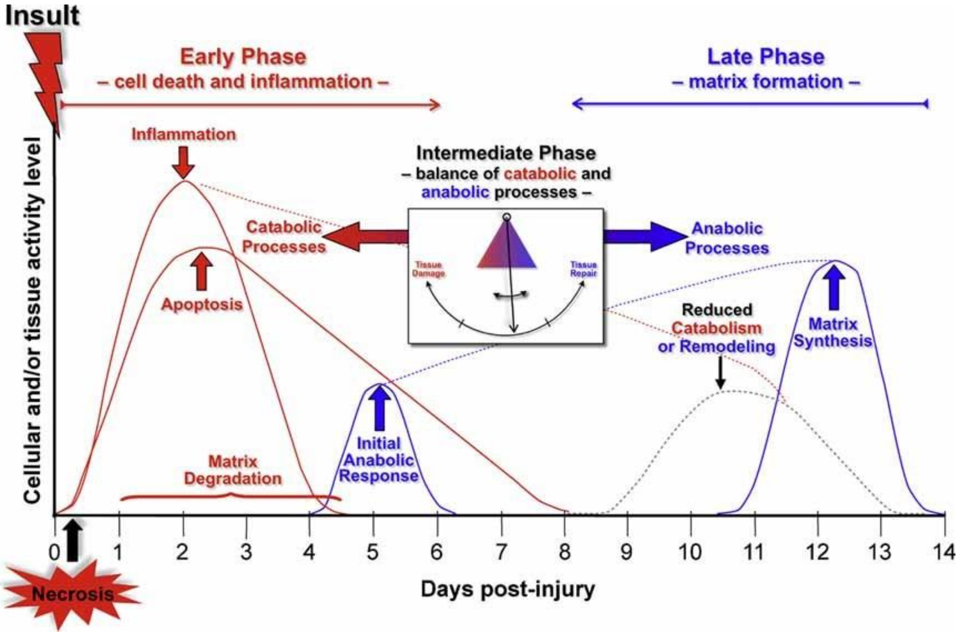

Figure 1.3. This conceptual framework depicts the immediate cellular responses to acute joint trauma and facilitates the identification of targets for early interventions. Catabolic and anabolic processes are involved in the response to the injury and overlap with one another. Copied from Anderson et al. 2011.[2]

Broadly, the open questions surrounding injury-induced dysfunction in articular cartilage, especially those addressed in this thesis, involve the important and complex interplay between mechanics and biology. As such, these questions can be grouped based on the biomechanics and mechanobiology perspectives. One on hand, biomechanics involves the study of how tissue structure influences its mechanical behavior. On the other hand, mechanobiology seeks to understand and explain how cells respond to their mechanical environment. In the first part of this thesis, we present studies that address both perspectives. In particular, Chapter 4 explores cracks, a mechanical consequence of injury in cartilage, from the perspective of biomechanics, while Chapter 2 and Chapter 3 explore cellular dysfunction and the biological consequences of injury from the mechanobiology perspective. In combination, both biomechanics and mechanobiology are both equally useful and important for understanding and treating injury-induced dysfunction in articular cartilage.

CHAPTER 2. MEASURING MICROSCALE STRAIN FIELDS IN ARTICULAR CARTILAGE DURING RAPID IMPACT REVEALS THRESHOLDS FOR CHONDROCYTE DEATH AND A PROTECTIVE ROLE FOR THE SUPERFICIAL LAYER

Bartell, L. R., Fortier, L. A., Bonassar, L. J. & Cohen, I. *Journal of Biomechanics* **48,** 3440-3446 (2015).

2.1 Abstract

Articular cartilage is a heterogeneous soft tissue that dissipates and distributes loads in mammalian joints. Though robust, cartilage is susceptible to damage from loading at high rates or magnitudes. Such injurious loads have been implicated in degenerative changes, including chronic osteoarthritis (OA), which remains a leading cause of disability in developed nations. Despite decades of research, mechanisms of OA initiation after trauma remain poorly understood. Indeed, although bulk cartilage mechanics are measurable during impact, current techniques cannot access microscale mechanics at those rapid time scales. We aimed to address this knowledge gap by imaging the microscale mechanics and corresponding acute biological changes of cartilage in response to rapid loading. In this study, we utilized fast-camera and confocal microscopy to achieve roughly 85 μm spatial resolution of the cartilage deformation during a rapid (~3 ms), localized impact and the chondrocyte death following impact. Our results showed that, at these high rates, strain and chondrocyte death were highly correlated ($p<0.001$) with a threshold of 8% microscale strain norm before any cell death occurred. Additionally, chondrocyte death had

developed by two hours after impact, suggesting a time frame for clinical therapeutics. Moreover, when the superficial layer was removed, strain – and subsequently chondrocyte death – penetrated deeper into the samples ($p<0.001$), suggesting a protective role for the superficial layer of articular cartilage. Combined, these results provide insight regarding the detailed biomechanics that drive early chondrocyte damage after trauma and emphasize the importance of understanding cartilage and its mechanics on the microscale.

2.2 Introduction

Osteoarthritis involves the degradation of articular cartilage in joints and is a leading cause of disability[29–31]. Clinically, 12% of osteoarthritis is post-traumatic (PTOA), wherein initiation stems from a distinct mechanical insult[3] and trauma is known to initiate progressive cartilage degradation[2,3,5,32–35]. After decades of research, PTOA initiation is poorly understood and a cure remains elusive[2,4–6].

Understanding PTOA has proven difficult, due in part to the complexities of cartilage material properties and the scope of the disease. For example, cartilage has a distinct superficial layer that is more compliant and dissipates more shear energy than the bulk[25,26,36–38]. Additionally, a traumatic, pathologic event can deliver forces over a fraction of a second (10^{-3} s)[28], while a patient may not present with symptoms for years (10^{8} s)[6]. This represents ten orders of magnitude in time that are important to the problem. Currently available animal and explant models can monitor bulk cartilage mechanics on injury time scales (10^{-3} s) and investigate biomechanical effects of trauma over hours to months (10^{1} – 10^{6} s)[6,39–43]. Studies have also investigated mechanics at the cellular level[44–46]. Although loading rate affects cellular response[47], methods to measure microscale mechanics (e.g. 10-100 µm) at physiologic time scales (e.g. $10^{-1} - 10^{0}$ s) have only recently been developed (Buckley et al., 2010). This leaves an important, unexplored gap in understanding microscale cartilage changes during and immediately following rapid traumatic injury.

The purpose of this study was to design and implement techniques to investigate the microscale mechanics of articular cartilage during rapid impact and to statistically describe the acute chondrocyte response. In particular, our method correlated microscale tissue strains during rapid impact (85 µm and 1 ms resolutions) with the microscale, time-dependent decrease in cell viability following that impact (85 µm and 10 min resolutions). This correlation enabled identification of microscale thresholds and sensitivities of chondrocytes to microscale deformation. Additionally, we tested for mechanical and biological changes in response with the superficial layer removed. This directly linked the mechanics of rapid cartilage impact to acute biological changes, giving new insight on the mechanisms of PTOA initiation.

2.3 Methods

A custom method enabled the correlation of chondrocyte death and microscale mechanics: chondral explants were impacted while a fast-camera recorded their rapid deformation; subsequent cell death was captured via confocal microscopy.

2.3.1 Impact device

The setup consisted of a custom impact device on an inverted confocal microscope (LSM 5 LIVE, Carl Zeiss Inc., Jena, Germany) (Figure 2.1) with a 10× objective. The confocal housing interfaced with a high-speed camera (v7.1, Vision Research, Wayne, NJ) and a mercury arc lamp (HBO 100, Carl Zeiss Inc., Germany) to enable epi-fluorescence microscopy at 1,000 frames per second.

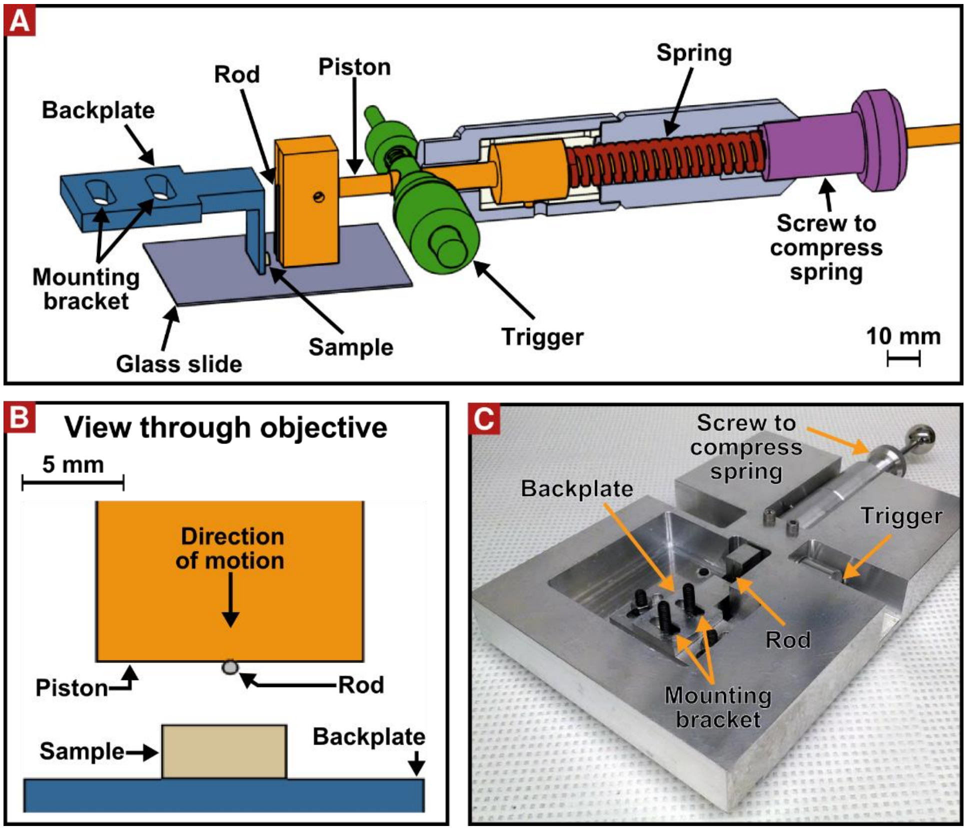

Figure 2.1. A technique for rapid impact microscopy was developed. A custom impact device (A,B) included a compressed spring which was released by a trigger to drive the piston and attached rod into the sample. The sample, which was mounted on the backplate, was immersed in PBS to maintain tissue hydration during testing. The cantilevered backplate was mounted to the stable body of the impact device via a mounting bracket. A glass slide allowed the sample to be viewed from below. The impact device was designed to mount on an inverted confocal microscope such that the objective looks up through the glass slide, as depicted (B). The microscope also interfaced with a mercury arc lamp and high-speed camera (not shown) to allow epifluorescence imaging at 1,000 frames per second. (C) A photograph of the impact device.

The custom impact device (Figure 2.1A) includes a spring (2.96 kN/m, McMaster-Carr, Elmhurst, IL) of adjustable compression which, upon triggering, drives a aluminum piston and attached 0.8 mm diameter steel rod (McMaster-Carr, Elmhurst, IL) into the sample (design inspired by Alexander et al.[48]). All impacts were energy-controlled at ~0.12 J (8.9 mm spring compression) to consistently cause cell death without micro-cracking and thus can be considered moderately pathologic[28]. Each sample was glued, as described previously[49], to a cantilevered aluminum backplate with the articular surface facing the impact tip. Impacts were observed from below through a glass slide, showing the rod's circular cross section approaching the sample (Figure 2.1B). Samples were mounted 2 mm above the glass slide, leaving a fluid layer in between. Using known weights, the backplate was calibrated as a cantilevered spring (152 kN/m). Backplate motion during impact was tracked using intensity-based image correlation in MATLAB (The MathWorks Inc., Natick, MA) and used to measure impact force. Peak force was combined with area of impact indentation to estimate peak bulk stress.

2.3.2 Sample preparation

Eighteen full-thickness, 6 mm-diameter chondral explants (without bone) were harvested sterilely from the outer rim of the tibial plateau of 6 neonatal calves (sex unknown, assumed random; Gold Medal Packing, Oriskany, NY). Explants were immersed in phenol red-free DMEM with 10% FBS (Invitrogen, Waltham, MA) and 1% antibiotics (100× penicillin-streptomycin, Mediatech, Manassas, VA) and stored at 4°C for up to 48 hours. Using tissue slicer blades (Stadie-Riggs, Thomas Scientific, Swedesboro, NJ), explants were cut in half to create two hemi-cylinders and trimmed to approximately 2.5 mm deep. Paired hemi-cylinders were used as control and impacted samples. For eight explants, 1 mm was removed from the articular surface, maintaining the 2.5 mm thickness, creating two sample populations: surface-intact and surface-removed.

2.3.3 High-speed deformation imaging

A fluorescent stain with a photobleached grid was used to visualize tissue motion during impact. All samples were stained in 28 µM 5-DTAF (ex/em 492/516 nm; Invitrogen, Waltham, MA) for 45 minutes followed by a 10-minute PBS rinse to provide general cartilage staining (Buckley et al., 2010; Silverberg et al., 2014). Using a precision wire mesh (TWP Inc., Berkley, CA) a 120 µm grid was photobleached on the samples. This grid size was chosen to be resolvable over motion blur, ensure adequate cell counting statistics (>50 cells/grid box), and capture tissue mechanical inhomogeneities. Paired control and impact samples were mounted side-by-side to the backplate and surrounded by PBS. Upon impact triggering, cartilage deformation was recorded using the fast camera.

2.3.4 Cell viability imaging

Chondrocyte death after impact was imaged. 2 uM ethidium homodimer (EthD) (Invitrogen, Waltham, MA) was added to the cavity, staining for 30 minutes before impact. Dead cells were imaged every 10 minutes for 3 hours following impact. Preliminary, 12-hour studies demonstrated that nearly all cell death occurred within 3 hours. To measure total cell density, paired control samples were frozen after experimentation, thawed in PBS, re-stained with EthD and re-imaged[50]. This produced confocal images of three treatment groups showing: (1) cell death in the impacted sample as a function of time (“impact”), (2) cell death in the control sample as a function of time (“control”), and (3) all cells in the frozen control sample (“frozen”), a measure of the total cell density in that sample. All confocal images were taken in a z-stack spaced at 10 µm to capture dead cells within 40 µm of the cut surface. This spacing was chosen to match the axial resolution of the confocal imaging setup. Images were collapsed in z, normal to the cut surface, before analysis.

2.3.5 Microscale deformation analysis

To extract microscale cartilage deformation during impact, fast-camera videos were analyzed in MATLAB. The image taken at peak indentation was used as the deformed configuration, with the image just before impact as its reference configuration. For bulk mechanics, displacement of the tissue surface under the impact rod was tracked manually to calculate bulk strain, correcting for backplate displacement. For microscale mechanics, template matching was used to find “bright cross” and “dark square” grid points (blue and yellow circles in Figure 2.2A-B). Using nearest-neighbor grid points, the Lagrange strain tensor $\boldsymbol{E}(x, y)$ was calculated with a spatial resolution of roughly 85 µm, where the y-axis is perpendicular to the articular surface (§2.7.1). To represent strain as a scalar field, two quantities were computed: the spectral norm of the strain, $\|\boldsymbol{E}\|$ (strain norm), and the magnitude of the shear component, $|E_{xy}|$ (shear strain).

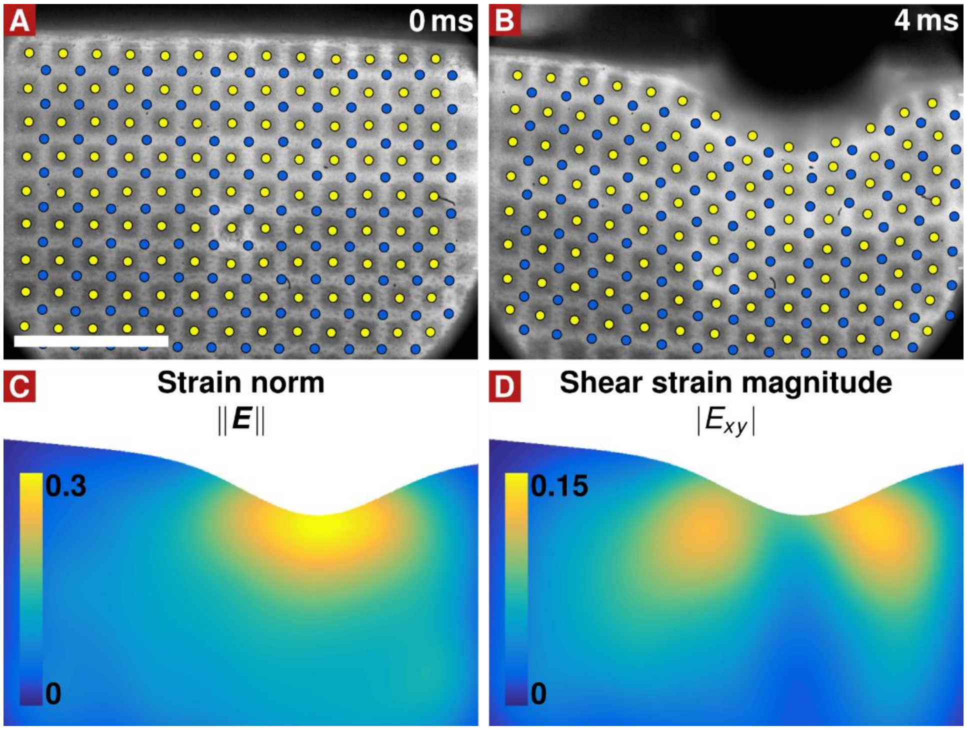

Figure 2.2. Representative fast-camera images of rapid cartilage impact and associated microscale strain fields. Fast-camera images taken before impact (A) and at peak indentation (B) were processed to extract grid-point locations (blue and yellow circles). This grid was divided into nearest-neighbor triangles, which were tracked between frames and used to extract the microscale Lagrange strain tensors. Note that dark triangles in the bottom left and right of (A,B) are the edge of the circular field of view, while the flat edge at the top is the surface of the sample. Representative maps of the spectral norm of the Lagrange strain (C) and the magnitude of the Lagrange shear component (D), both shown with respect to deformed spatial coordinates, demonstrate characteristic patterns of strain localization. The scale bar is 500 µm and applies to all plots.

To characterize the shear strain fields' size and orientation, principal component analysis was performed on the (x, y) points, with a binary weighting based on the shear strain value: 1 for shear strain above 50% of the sample's maximum and 0 otherwise. The first principal component and its orientation relative to undeformed coordinates were extracted, representing the size and orientation of the strain pattern, respectively.

2.3.6 Cell viability analysis

Confocal images were processed in MATLAB to find (x, y) locations of all dead cells (§2.7.2). Through comparison with manual counting, cell counting uncertainty was estimated as 7%. Using Sobel edge detection, the sample surface was identified and fit to a second-order polynomial function of lateral displacement, enabling a correspondence between spatial coordinates, (x, y), and depth coordinates, (x, d), where d is depth. The same technique was used to compute the depth of each grid point in fast-camera images.

Cell locations were binned to calculate microscale probability of death due to impact as $P(x, y, t) = \frac{\rho_{\text{impact}}(x,y,t) - \rho_{\text{control}}(x,y,t)}{\rho_{\text{frozen}}(x,y) - \rho_{\text{control}}(x,y,t)}$, where $\rho_i(x, y, t)$ is the area number density of dead cells in each treatment group, i (§2.4), as a function of bin location, (x, y), and time after impact, t. Control densities were subtracted from the numerator and denominator to remove death due to causes other than impact. Roughly 100% cell death was observed at the surface ($\rho_{\text{frozen}} - \rho_{\text{control}} \cong 0$), invalidating analysis there. Thus, data less than 200 µm deep were discarded.

To highlight the time evolution, cells in a 400 µm wide region centered about the impact location were binned at 50 µm in depth (collapsing along the x direction) and used to calculate $P(d, t)$, the probability of death due to impact as a function of depth and time after impact. Trends in $P(d, t)$ were averaged across all samples in each population, where the standard deviation of sample-to-sample variation was roughly 25 percentage points. In MATLAB, a mixed-effects linear regression model was implemented to test for significant differences between data from surface-intact and surface-removed samples. In the model, the response variable was P, while d, t and surface treatment (i.e. intact or removed) were fixed-effect predictor variables, including interaction terms. An independent random effect was added to account for sample to sample variation. Residuals were checked for normality, confirming the model's validity.

2.3.7 Correlating microscale deformation and viability

Impact deformation and viability following impact were correlated on the microscale. Fast camera grid points in the undeformed configuration (§2.5) were projected onto the confocal image of the same sample at 3 hours after impact. Nearest-neighbor grid points were used as bin boundaries to calculate the microscale probability of cell death due to impact (§2.6). Accordingly, at each grid point (x, d), a correspondence was established between strain norm, $\|\boldsymbol{E}\|$ (§2.5), and probability of death due to impact, P. Fields of $\|\boldsymbol{E}\|$ and P were averaged across sample populations (§2.7.3).

A mixed-effects linear regression model tested for the dependence of P on $\|\boldsymbol{E}\|$ and surface treatment. The response variable was P, while d, t, $\|\boldsymbol{E}\|$, and surface treatment were fixed-effect predictor variables, including interactions. In an additional model, $\|\boldsymbol{E}\|$ was used as the response, with d, t, and surface treatment as predictors. In both models, an independent random effect was added to account for sample to sample variation. In all analyses, residuals were checked for normality, confirming the models' validity.

2.4 Results

2.4.1 *Bulk mechanics*

A custom device (Figure 2.1) impacted cartilage samples rapidly and consistently (Video 1). Impacts lasted 8 ms, with a time to maximum indentation of 3.7 ± 0.7 ms (mean ± standard deviation). Peak bulk strain and strain rate were 13 ± 4% and $4 \pm 1 \times 10^3$ %/s. Peak force, bulk stress, and bulk stress rate were 8 ± 3 N, 2.3 ± 0.9 MPa, and $7 \pm 3 \times 10^2$ MPa/s. Impact time, strain, force, and stress were not significantly different between surface treatment populations, as determined using unpaired, two-tailed t-tests ($p = 0.7; 0.04; 3; 0.9$, respectively). No tissue swelling was observed over the 3-hour experiment.

2.4.2 *Microscale deformation*

Microscale strain norm and shear strain during impact were computed from fast-camera images, revealing characteristic maps of each (Figure 2.2). Strain norm was highly concentrated near the impact and shear strain fields had two characteristic lobes (Figure 2.2C,D). Peak shear strain was lower than peak strain norm. When the superficial layer was removed, strain fields had similar trends but lower values overall (Figure 2.3). Shear strain lobes were longer ($p = 0.006$) and oriented more vertically ($p = 0.001$) for surface-removed samples.

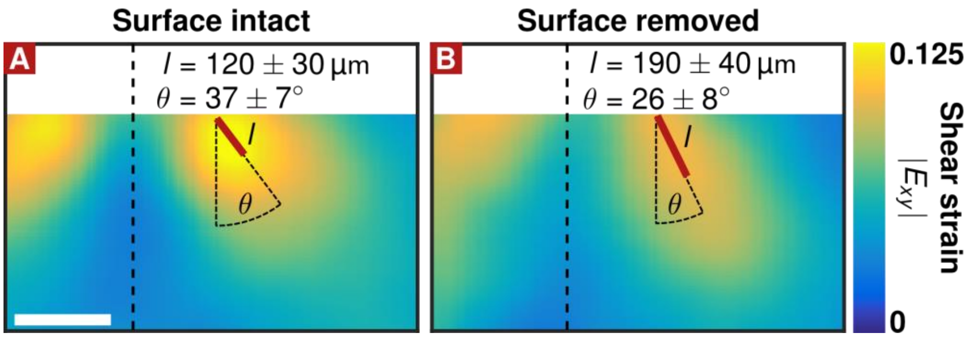

Figure 2.3. Average microscale shear strain patterns show variations with surface treatment. As compared to surface-intact samples (A), the lobes in surface-removed samples (B) became significantly more elongated ($p = 0.006$) and more vertically aligned ($p = 0.001$), based on principal component analysis. The dashed line indicates the axis of impact in each plot. The scale bar is 250 µm and the color and scale bars apply to both plots.

2.4.3 Cell viability

Cell death increased dramatically after impact, showing complex spatial and temporal evolution (Figure 2.4). For both sample populations, average probability of death due to impact in the region of interest (orange box) was highest near the surface (Figure 2.4C,D). This probability increased with time, though most cell death occurred by 2 hours. Regression modeling confirmed that time, depth, and their interaction were significant predictors of probability of death ($p = 9 \times 10^{-292}; 4 \times 10^{-30}; 4 \times 10^{-193}$, respectively). Cell death in control samples increased over 3 hours, but only 15 percentage points. No dispersal of the EthD stain was observed after freezing.

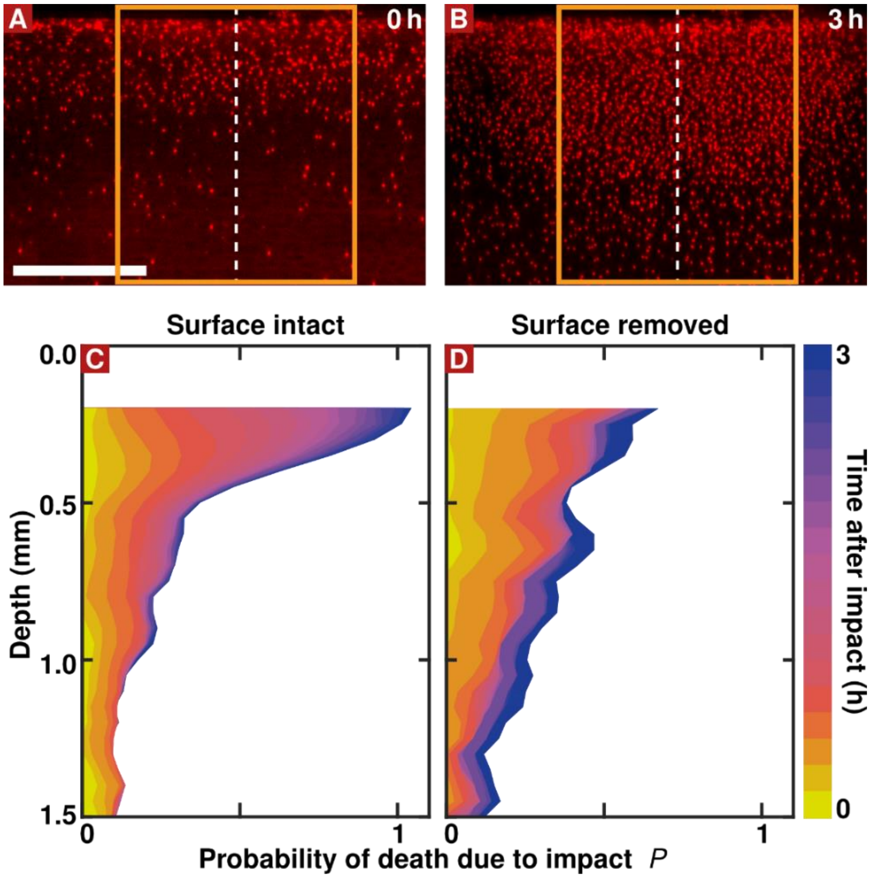

Figure 2.4. Spatial and temporal evolution of chondrocyte death after impact. A representative confocal image sequence shows dead chondrocytes in an impacted, surface-intact sample immediately following impact (A) and 3 hours after impact (B). Both images show the same location and the dashed line indicates the axis of impact. Plots (C,D) reflect the time- and depth-dependent increase in probability of cell death after impact, calculated from the region of interest (orange box) and averaged over all samples for surface-intact (C) and surface-removed (D) sample populations. With the surface intact, the peak is more confined to the superficial layer ($p = 2 \times 10^{-17}$). Depths less than 200 µm were excluded because this region exhibited nearly 100% death, invalidating analysis at these points. The scale bar is 250 µm.

Comparing surface treatment populations, the peak probability for surface-intact samples was confined to the surface layer while the pattern extended deeper for surface-removed samples ($p = 2 \times 10^{-17}$). Time evolution did not vary significantly between surface treatments ($p = 0.6$).

2.4.4 Strain and viability correlation

Average strain and probability of death due to impact showed strikingly similar patterns within but not across surface treatment groups (Figure 2.5A-D). Both patterns were concentrated near the impact but penetrated deeper with the surface removed ($p = 3 \times 10^{-7}; 2 \times 10^{-6}$, for strain norm and probability of death comparisons). The clear relationship between strain norm and probability of death due to impact ($p = 2 \times 10^{-68}$) was apparent in correlation plots (Figure 2.5E,F). This correlation varied slightly, albeit significantly, with depth and surface treatment ($p = 2 \times 10^{-46}; 1 \times 10^{-13}$). For both populations, linear fits revealed a threshold of 8% microscale strain before any cell death occurred and a sensitivity of ~18% strain to produce ~50% probability of cell death at 3 hours.

Figure 2.5. Microscale patterns of strain norm (A,B) and probability of death (C,D) averaged over all samples in each surface-treatment population show strikingly similar patterns within a given population. Average patterns are shown for both surface-intact (A,C) and surface-removed (B,D) populations and all data are plotted with respect to undeformed spatial coordinates. Both strain and chondrocyte death penetrated deeper into the samples when the superficial layer of cartilage was removed ($p = 3 \times 10^{-7}; 2 \times 10^{-6}$). The dashed line indicates the axis of impact in each plot. Additionally, the probability of cell death after impact was strongly correlated with the microscale strain norm for all samples with the surface intact (E) or removed (F) ($p = 2 \times 10^{-68}$). In these plots, each data point represents one point from the tracked fast-camera grid of one sample and takes on values corresponding to the microscale strain and probability of death due to impact in the corresponding region of that sample. Points are color-coded based on their depth from the sample surface. Linear fits are shown for each population and the text indicates the strain-axis intercept (threshold), the slope (sensitivity), and the coefficient of determination (R^2) of the fit. As before, data within 200 μm of the surface were omitted. The scale bar is 250 μm and applies to A-D.

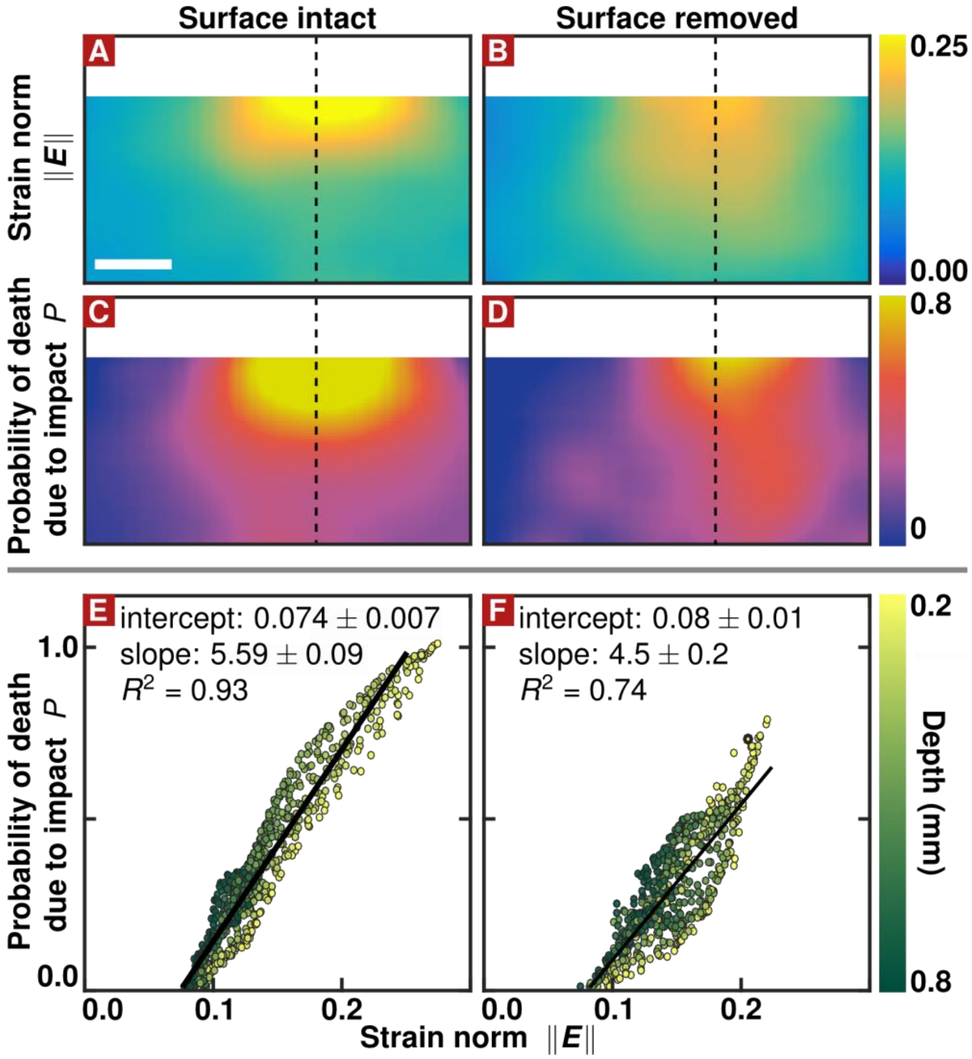
Surface intact
Surface removed
A
B
C
D
E
F
Strain norm $\|E\|$
Probability of death due to impact P
0.25
0.00
0.8
0
intercept: 0.074 ± 0.007
slope: 5.59 ± 0.09
R^2 = 0.93
intercept: 0.08 ± 0.01
slope: 4.5 ± 0.2
R^2 = 0.74
1.0
0.0
0.0
0.1
0.2
0.0
0.1
0.2
0.2
Depth (mm)
0.8

Correlation was also performed using other Lagrange strain scalars (§2.7.4). Some correlations were similarly high ($R^2 = 0.91; 0.94; 0.95$, for the determinant, P2 norm, and deviatoric spectral norm, respectively) while others were lower ($R^2 = 0.11; 0.05$, for shear strain and trace, respectively).

2.5 Discussion

The goal of this study was to understand the relationship between the microscale mechanical environment in cartilage during rapid loading and subsequent changes in chondrocyte viability. Additionally, we investigated how mechanical heterogeneity mediated chondrocyte response. Thus, a custom method was developed, integrating fast camera and confocal microscopy with spring-loaded impact. This method allowed chondrocyte death to be correlated with rapid tissue deformation on the microscale.

Results showed that, as depicted in Figure 2.5, the probability of cell death due to impact was highly correlated with the Lagrange strain norm, enabling the threshold and sensitivity of cells to microscale mechanics to be determined. This correlation was similarly strong for both surface-intact and surface-removed samples, revealing that, for loading at these high rates, strain norm – rather than any depth-dependent cellular sensitivity, for example[51] – explains a large majority of the variation in chondrocyte death (93%, for surface-intact samples).

The results further revealed a protective role for the superficial layer. The superficial layer of cartilage is more compliant than the bulk[25,36,38,49,52,53], and thus strain was concentrated in this region, as reflected in Figs. 2 and 3. Since cell death was so highly correlated with strain, it, too, was concentrated in the superficial region of surface-intact samples, as observed previously[54–58]. However, because impacts were energy controlled, surface-removed samples experienced lower strains at their surface, potentially explaining their lower peak probability of death (Figure 2.4C,D). Overall, however, both strain and cell death penetrated significantly deeper after surface removal, reflecting the more homogeneous mechanical properties of the remaining tissue. Thus, by concentrating the strain, the compliant surface layer of healthy cartilage protects the deeper tissue. This novel design principal may be important for the robustness of cartilage and could potentially be applied in other engineering applications, including tissue engineering.

These results may also be useful when interpreting in the context of injury mechanics across many spatial scales. For example, recent studies have incorporated cartilage's mechanical inhomogeneities into models, translating bulk loading into the microscale loading environment[59–62]. Given the results of this study, subsequent cell death can be inferred from microscale mechanics at high rates without invasive procedures.

Temporal trends of cell death were also studied. After impact, cell death saturated in about 2 hours (Figure 2.4C,D), suggesting a time window following joint trauma in which drugs or therapeutics could be most effective. Notably, as determined by preliminary experiments, EthD could diffuse and stain compromised cells within a few minutes, while an apoptotic response typically develops in hours or days[63,64]. Thus, the acute chondrocyte death observed here was most likely necrotic, in agreement with Chen et al.[50] (§2.7.5).

One limitation of this study is the use of immature cartilage, which may be more susceptible to damage[56,65]. However, immature and mature tissues are mechanically similar[49] and immature tissue provides a consistent framework for studying injury[66,67]. Samples also exhibited extensive cell death at the surface, masking surface chondrocytes which may respond differently to loading and potentially altering the sensitivity of nearby, viable cells. This limitation may be overcome by storing samples in culture conditions. Additionally, the impact geometry and the material of the impacting rod did not directly mimic *in vivo* loading. Instead, the unconfined compression and small-diameter impacting rod were used to impose a wide range of strains in the field of view, enabling strain and cell death correlations to be rigorously investigated. Translating loading from the bulk scale to the microscale will depend strongly on the geometry and boundary conditions, potentially affecting cartilage response[68,69]. However, as a physical property, the microscale strain thresholds would not be expected to change with loading and geometry. Though the source of the strain may not be observed *in vivo*, the general relationship between strain and cell death should hold for a broader variety of loading scenarios at similar rates. It should be noted that, at these length scales, this study cannot measure cellular strains or mechanotransduction mechanisms, but instead measures strain and cell death as continuous distributions on the scale of tissue inhomogeneity[70].

Previous studies have similarly linked impact mechanics to cartilage damage, both mechanical (e.g. fissuring) and biological (e.g. chondrocyte death)[40,42,43,58,71–74]. In this study, impacts (0.1 J energy, 2 MPa stress) caused chondrocyte death without fracture, implying that bulk cell death thresholds are below this level while fissuring thresholds are above. This energy is in agreement with cell death thresholds implied or observed previously[40,73], while stress thresholds are typically much higher[42,74].

More broadly, previous cartilage impact studies have failed to establish consensus regarding the thresholds and sensitivities of any damage measure to a given loading profile. Existing discrepancies (e.g., studies by Haunt. et al., Natoli et al., and Newberry et al.[41,75,76]) may reflect the large variety of impact protocols, geometries and boundary conditions. Moreover, tests in sufficiently different loading scenarios with respect to material behavior (e.g. gel diffusion rate[77]) cannot be reliably compared. Bulk measures are also limiting. Because cartilage is spatially inhomogeneous[78], they may not adequately portray the local cartilage environment. Indeed, even if damage spreads, it is initiated locally – on the cellular scale for biological damage or on the fiber scale for matrix damage.

The method presented here helps clarify how rapid mechanical signals correlate with cell responses. Fast-camera imaging enables the response of a true impact – rather than only the slower, so-called injurious compression – to be investigated on the microscale[28], statistically linking strain and cell viability. Future studies will exploit these higher spatial and temporal resolutions to better understand damage initiation in cartilage. By varying microscale impact mechanics and geometry (e.g. strain, strain rate, rod size), thresholds and sensitivities of both biological changes and mechanical damage after impact can be determined. Additionally, this setup can address the effectiveness of various drugs and dosage protocols for preventing or reducing acute chondrocyte death. Overall, by studying micrometer- and millisecond-scale responses, this experimental approach provides a powerful tool for clarifying the details of cartilage injury response and PTOA initiation after trauma.

2.6 Acknowledgments

This work was supported in part by the National Science Foundation under award No. DMR-1056662, in part by the National Institutes of Health under award No. R21-AR062677, and in part by the Harry M. Zweig Fund for Equine Research. L.R.B. acknowledges support from the NSF Graduate Research Fellowship, No. DGE-1144153. The authors wish to thank Michelle Delco, Corinne Henack, Tsevi Beatus and Brian Leahy for helpful discussions and support with this study.

2.7 Supplemental information

2.7.1 Analysis of fast-camera images

Two frames from fast camera videos were analyzed to extract microscale deformation patterns. Each frame was analyzed in MATLAB, using template matching to find the (x, y) locations of the many “bright cross” and “dark square” parts of the photobleached grid, where $(0,0)$ corresponds to the impact center, i.e. the first point of contact between the impact tip and the sample. Combined, these grid points produced a diagonal square lattice of coordinates, as shown by blue and yellow circles (Figure 2.2 and Figure 2.6). These points were tracked between frames to visualize the cartilage deformation. Neighboring points were separated by roughly 85 µm, thus setting the spatial resolution. This lattice was divided into triangles of nearest neighbors. Note that each point has four associated triangles, except for those points at the edge of the field of view, which have fewer. In Figure 2.6, the four nearest-neighbor triangles of one point are outlined, showing the microscale reference (Figure 2.6A) and deformed (Figure 2.6B) configurations around that point. For each frame, each nearest-neighbor triangle was recast as two vectors, $\boldsymbol{v}^{(1)}$and $\boldsymbol{v}^{(2)}$, which give the position of the second and third vertices relative to the first. Using these vectors, the 2D deformation gradient tensor $\boldsymbol{F}$, which maps material points between states of deformation and is the fundamental measure of deformation in continuum mechanics, was calculated using Equation. 2.1 As implied by the notation, the first frame, just prior to impact tip collision, was taken as the undeformed, or reference, configuration ($t = t_0$), while the frame taken at peak indentation ($t = t_1$) was used as the deformed configuration.

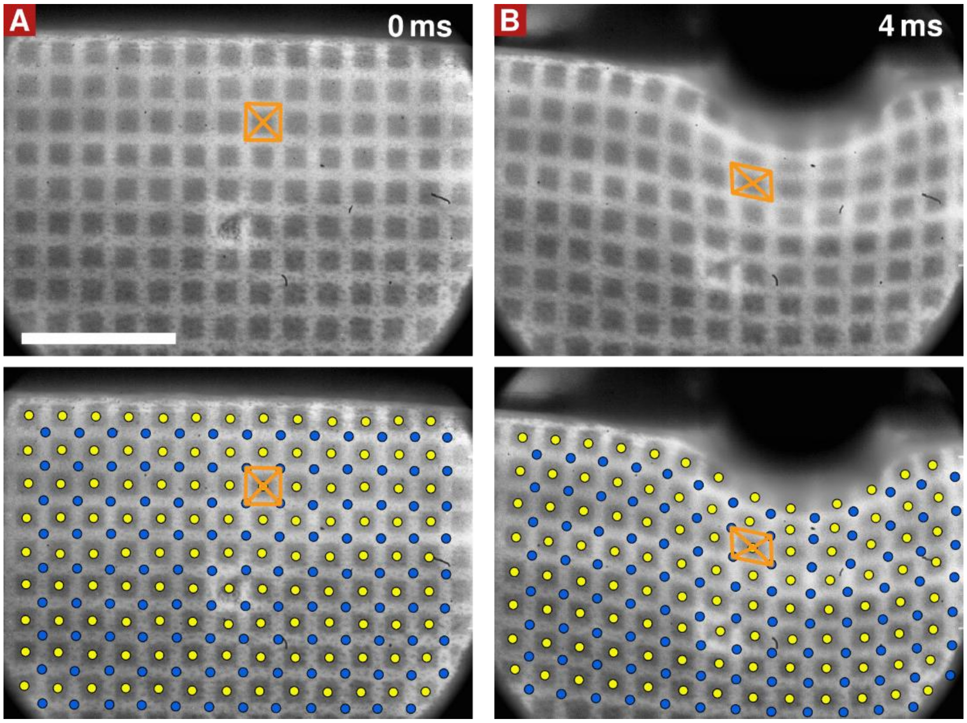

Figure 2.6. Fast-camera images show the cartilage photobleached grid just before impact (A) and at peak indentation (B). In the bottom frames, tracked grid points are overlaid on the original images. The orange box highlights local deformation in one part of the grid by outlining the four triangles formed by connecting one yellow point with its four nearest neighbors. The scale bar is 500 µm.

$$\boldsymbol{F}(x,y) = [\boldsymbol{v}^{(1)}(x,y,t_1) \quad \boldsymbol{v}^{(2)}(x,y,t_1)]\,[\boldsymbol{v}^{(1)}(x,y,t_0) \quad \boldsymbol{v}^{(2)}(x,y,t_0)]^{-1} \tag{2.1}$$

For each triangle, the deformation gradient tensor was subsequently used to calculate the Lagrange strain tensor at peak indentation (Equation 2.2). Two scalar measures of the Lagrange strain were calculated for each triangle: the spectral norm and the magnitude of the shear component. At each grid point, (x,y), scalar quantities of the norm and shear strain from the four nearest-neighbor triangles were averaged together.

$$\boldsymbol{E}(x,y) = \tfrac{1}{2}(\boldsymbol{F}^{\mathrm{T}}\boldsymbol{F} - \boldsymbol{1}) \tag{2.2}$$

Note that optical aberrations were observed to have no noticeable affect the positions of the grid points. This was confirmed by analyzing the grid spacing with the sample flat on the glass slide and elevated in the impactor with a fluid layer in-between. Grid spacings were not significantly different between the two configurations ($\mathrm{p} = 0.93$, as determined by a student's T-test).

As noted in the main text, strain norm and shear strain magnitude were extracted from the Lagrange strain tensor at each point in space. Error in both strain measures was estimated to be 0.01 strain, with an additional offset bias of 0.01 strain since these are positive quantities. Error was estimated via deformation analysis of an un-impacted sample with a static grid and via deformation analysis for an impacted sample performed multiple times.

Data from multiple samples were combined to produce average scalar strain fields for surface-intact and surface-removed sample populations (see §2.7.2). For both scalar measures, the standard deviation of sample-to-sample variation was 0.03 strain.

2.7.2 Image algorithm to locate cells in confocal images

Confocal images of EthD signal were processed in MATLAB to find the (x, y) locations of dead cells. The algorithm consisted of the following steps: First, the highest 10% and lowest 5% of grayscale values were discarded (i.e. set to high or low saturation values). Then, a median filter (MATLAB function `medfilt2`) was used for background subtraction, followed by adaptive histogram equalization (`adapthisteq`) to remove intensity variations across the image. Grayscale morphological dilation (`imdilate`) with a disk shape (`strel`) was then performed to extend regions of local maxima. Finally, connected regions of constant grayscale value were segmented, discarding regions with extreme areas or low intensities. For each segmented region, or cell, the spatial location was calculated as the region's centroid weighted by the intensity of the original image (`regionprops`), where $(0,0)$ corresponds to the impact center. For all filtering described, the window size was approximately equal to the diameter of a chondrocyte (10 pixels, in this case). Figure 2.1 shows an example confocal image (surface intact sample, at 3 hours after impact). White dots are overlaid to highlight cell positions located by the algorithm.

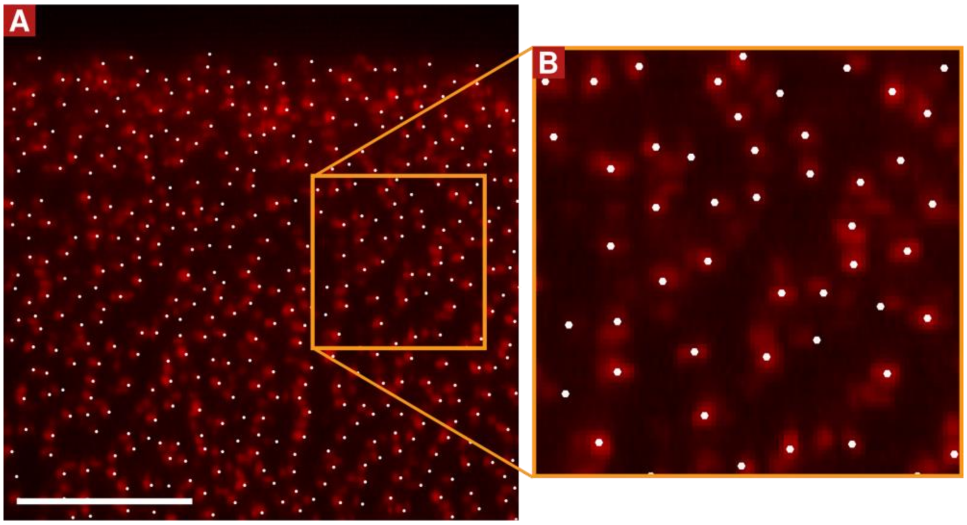

Figure 2.7. (A) A section of one confocal image shows dead cells in a surface-intact sample 3 hours after impact. Cell locations found using the image processing algorithm as indicated by white dots. (B) A zoomed view clearly shows individual dead cells. The scale bar is 100 µm.

2.7.3 *Averaging scalar fields across multiple samples*

Scalar fields (i.e. 2D spatial maps) of shear strain, strain norm, or probability of death due to impact were averaged across multiple samples to produce average scalar fields of each quantity (e.g. Figs. 2,4). The same method was used to average each of these scalar fields: To combine fields from multiple samples, the fields were first represented as a scatter of points (x, y, z), where (x, y) are the spatial dimensions and z is the scalar measure of interest (i.e., shear strain, strain norm, or probability of death due to impact). Second, these points were all plotted together and interpolated onto a regularly spaced grid. Thirdly, these points were smoothed using a Gaussian filter with a window size and standard deviation of 250 µm and 80 µm, respectively. Finally, this smoothed field was resampled at the original (x, y) points, producing a scatter of points $(x, y, \bar{z})$ representing the average, smoothed field of the scalar measure of interest.

2.7.4 Microscale patterns and correlations for all Lagrange strain components

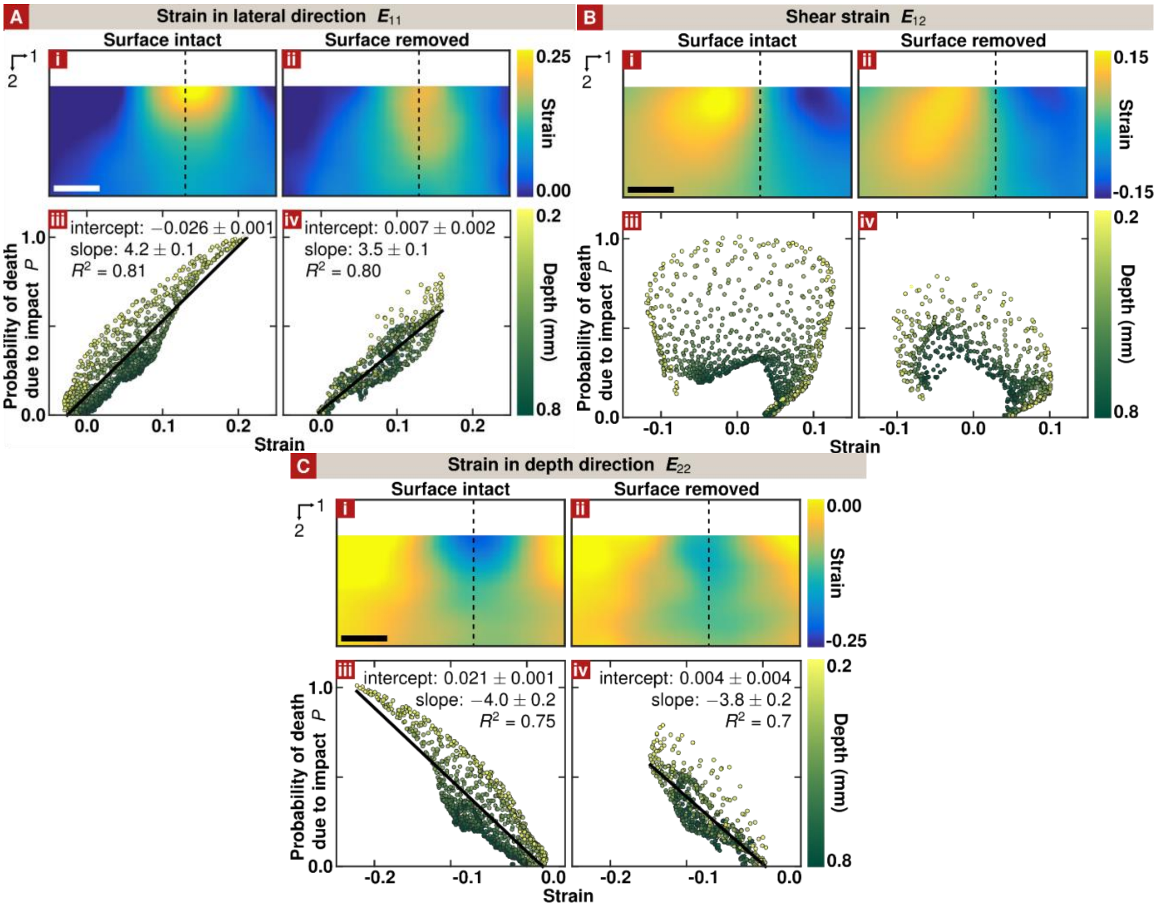

Figure 2.8. Average microscale strain patterns (i,ii) and their correlation with the probability of cell death due to impact (iii,iv) for the three components of the Lagrange strain tensor: strain in the lateral direction (A), shear strain (signed) (B), and strain in the depth direction (C). Any correlation with shear strain is clearly nonlinear and so regression lines and equations are not shown for (B). As before, data within 200 µm of the surface were omitted. The scale bar is 250 µm and applies all strain patterns.

2.7.5 Transient chondrocyte permeability

Ethidium homodimer-1 (EthD), the nuclear stain used to identify dead chondrocytes in these experiments, is well established and has been used to identify dead cells in myriad contexts[79–81]. The staining mechanism for this dye, as well as many other common "dead cell" stains, relies on the fact that the molecule is cell-impermeant and cannot normally penetrate into a cell's membrane. Only when a cell becomes abnormally permeable (e.g. if it breaks apart) can EthD enter the cell and bind to DNA, eliciting a conformational change which results in the observed red fluorescence. One issue associated with the method described in this paper is the fact that once stained with EthD, a cell cannot generally "un-stain". Thus, there is the potential that cells are only transiently permeable and that some of the cells stained as "dead" actually recover their membrane impermeability, either during the 3-hour window observed here or over longer time scales.

To check for transient permeability, three test samples were dissected and immediately impacted in sterile conditions, following the impact protocol described in this paper. Following impact, samples were returned to sterile media and incubated. At 24 and 48 hours after impact, samples were subsequently stained with "dead cell" stains, YOYO-1 and TOTO-3 (Molecular Probes, Eugene, OR), which also rely on membrane impermeability but fluoresces at different wavelengths. If, during the two days after impact, a cell recovered its membrane integrity, then that cell would stain in one image but not in one of the subsequent images. Thus, the EthD images taken at 3 hours after impact were registered to and manually compared with images of the same sample taken with the different stains at 24 and 48 hours after impact. It was found that less than 1% of cells indicated any signs of transient permeability. Although this is not an exhaustive proof, it provides strong evidence for the fact that chondrocytes stained during the impact experiments described in this paper are, in fact, dead and remain so during and after the experiment.

CHAPTER 3. TRACKING CHONDROCYTE FATE REVEALS THAT MITOPROTECTIVE THERAPY ELIMINATES PERACUTE, STRAIN-DEPENDENT MITOCHONDRIAL DYSFUNCTION AFTER ARTICULAR CARTILAGE IMPACT

Bartell, L. R., Fortier, L. A., Bonassar, L. J., Cohen, I., Delco, M. L. *In preparation*.

3.1 Abstract

Post-traumatic osteoarthritis involves the mechanical and biological deterioration of articular cartilage within joints after injury and is a growing problem in healthcare. Recently, mitochondrial dysfunction and altered cellular respiration have been associated with acute cartilage deterioration after injury. This finding is particularly important because recently-developed mitoprotective drugs, such as SS-peptides, have shown success for preserving mitochondrial structure and function in other mitochondria-mediated diseases. It is not known, however, if cartilage injury induces structural changes within the mitochondria, to what degree mitochondrial dysfunction in cartilage depends on the mechanics of injury, or the time frame over which such dysfunction develops. Similarly, it is unknown if SS peptide treatment can preserve mitochondrial structure and function after cartilage injury. Here, we combined rapid indentation, fast-camera elastography, and longitudinal fluorescence assays to show that impact induces mechanically-dependent mitochondrial depolarization within 15 minutes after injury. Using electron microscopy, we further show that impact induces rapid structural changes in mitochondria that are related to reduced mitochondrial function, namely swelling and loss of cristae structure. Remarkably, we find that

SS-peptide treatment prior to impact protects mitochondrial structure and preserves mitochondrial function at a level comparable to that of un-impacted control samples. As such, this study reveals the peracute kinetics of mitochondrial dysfunction and shows that the preservation of mitochondrial structure is a promising therapeutic target for peracute, injury-induced cartilage damage.

3.2 Introduction

Post-traumatic osteoarthritis (PTOA) is a common cause of disability and the prevalence of OA is growing as the population ages, yet no treatments are available to prevent this joint disease[82,83]. A hallmark of OA is the mechanical and biological deterioration of articular cartilage, the soft tissue that provides load dissipation and a low friction surface for joint motion[1]. Articular cartilage is composed primarily of a dense, poro-viscoelastic extracellular matrix and chondrocytes, the sole cell type in cartilage. Despite their small numbers, chondrocytes are primarily responsible for maintaining cartilage homeostasis[63,81]. Chondrocyte function is regulated in part by mechanical stimuli, where moderate loading is beneficial, but rapid or excessive loading induces cell death and initiates catabolic responses that lead to cartilage matrix degradation[5,27]. These responses to injurious loading can develop over acute time scales (hours to days) or longer[2]. Recently, a peracute (minutes to hours) necrotic response was also revealed, and this rapid cell death was correlated with the strain experienced during an *ex vivo* injury[84]. Despite these important observations, the mechanism by which mechanical signals lead to the peracute progression of cartilage damage after injury has not been fully established.

Importantly, mounting evidence suggests that mitochondria are a central mediator of the peracute injury response in articular cartilage, but much remains unknown about the relationship between cartilage injury and mitochondrial dysfunction. Mitochondrial and respiratory dysfunction are known to occur in late stage OA and early-chronic OA[85–88], and have been observed within six hours after injury[89]. Oxidative stress and apoptosis have also been observed as acute responses to cartilage injury and can be mediated by mitochondria via the caspase cascade[2,90–96]. However, the kinetics of mitochondrial dysfunction in the peracute time frame after injury remain unknown. Additionally, mitochondria are mechanically connected to their intra- and extra-cellular environment, and thus could act as mechanotransducers of cartilage injury[93]. One *ex vivo* wear model revealed that acute mitochondrial dysfunction is related to sliding strain[96], but it remains unknown if a similar response develops after rapid injurious loading or to what degree such mitochondrial dysfunction depends on the injury mechanics, especially peracutely.

Injury-induced mitochondrial dysfunction in cartilage is especially interesting because it may present a promising therapeutic target. Broadly, mitochondria rely on the efficiency of the electron transport chain (ETC) to build an electrochemical gradient, or polarization, across their inner membrane, which in turn drives energy production. As such, loss of membrane structure and polarity are hallmarks of mitochondrial dysfunction and altered cellular respiration[97]. If such structural and functional mitochondrial changes are mediators of injury-induced dysfunction in articular cartilage, they may be a druggable target. In particular, recently-developed mitoprotective SS-peptides are known to localize to the inner mitochondria membrane, where they stabilize and protect membrane structure[98]. Indeed, SS-peptides have shown promise for treating other mechanically-induced, mitochondria-mediated diseases and are currently in clinical trials for treating ischemia reperfusion injury[99–101]. One initial study suggests that SS-peptides can reduce cell death and matrix degradation 24 hours to 1 week after cartilage injury[89]. However, it is unknown if SS-peptides can prevent impact-induced mitochondrial dysfunction, especially peracutely. Similarly, the mechanism of action for SS-peptides in cartilage is also unknown. As such, determining if mechanical injury of cartilage induces loss of mitochondrial structure and polarity, and testing SS-peptides to reverse such dysfunction, would show that these changes present a druggable target for cartilage injury.

Understanding how chondrocyte mitochondria respond to their mechanical environment during injury requires observing both the mechanical and biological response of cartilage at high spatial and temporal resolutions, which presents a challenge experimentally. Impact loading must be fast to be considered injurious[28] and cartilage material properties vary over tens of microns[26,102]. Thus, to observe local tissue deformation *in situ* during injurious loading, data must be collected at rates around 1,000 points per second and with micon-scale spatial resolution. A fast-camera elastography technique was recently developed to enable this rapid mechanical analysis[84]. Additionally, to observe peracute chondrocyte and mitochondrial function, individual cells' behavior must be tracked over time with a temporal resolution of minutes, which could be accomplished using optical microscopy and fluorescent probes. However, optical microscopy cannot resolve the morphology and internal structure of individual mitochondria and so electron microscopy is commonly utilized to observe mitochondrial structure in fixed samples[103]. Testing the mechanical dependence of peracute mitochondrial dysfunction after cartilage impact would require combining all of these techniques to observe chondrocytes *in situ* during injurious loading.

In this study, we considered two hypotheses: first that impact injury induces rapid, mechanically-dependent dysfunction and structural degradation of chondrocyte mitochondria and second, that SS-peptides protect the mitochondrial structure and prevent this dysfunction. To test these hypotheses, we combined advanced techniques from both mechanics and biology to reveal the complex relationship between injurious loading and individual chondrocyte behavior. In particular, we used longitudinal confocal microscopy with computer vision analysis to track a large number of individual chondrocytes in an *ex vivo* injury model and correlated their behavior with local injury mechanics obtained via fast camera elastography. We further utilized electron microscopy to confirm structural and morphological changes in mitochondria and observed how all of the responses changed with SS-31 treatment.

3.3 Results

3.3.1 Temporal evolution of mitochondrial depolarization after impact

In order to study mitochondrial depolarization after cartilage injury, we developed a longitudinal microscopy technique to automatically track thousands of individual cell fates over time and space using computer vision, and applied this method in an established *ex vivo* injury model[84,104]. Paired hemi-cylindrical cartilage explants were mounted side-by-side on a cartilage impact device in a shared PBS bath (Figure 3.1). One hemi-cylindrical sample was impacted with a 0.8 mm diameter rod while the second served as a no-impact control. This geometry exposed the tissue to a wide range of strains in a relatively small field of view, enabling correlations between cellular dysfunction and injury mechanics to be rigorously investigated. To track temporal changes in cellular function after injury, samples were stained with a 3-stain fluorescence assay, directly visualizing both the polarity of the inner mitochondrial membrane and non-specific cell death. Samples were imaged at multiple locations longitudinally, before and up to 60 minutes after impact. At each time point, segmented cells were classified into one of 3 possible states: polarized mitochondria, depolarized mitochondria, or dead, based on each stain's intensity distribution in the given cell (Figure 3.2). In a subset of experiments, paired samples were treated with 1 µM SS-31 peptide 30 minutes prior to impact in order to test the proposed treatment mechanism. SS-31 treatment remained in the bath surrounding both samples throughout the experiment.

Cartilage samples showed a rapid and pronounced wave of mitochondrial depolarization after impact that was suppressed by SS-31 treatment. In untreated samples, the fraction of chondrocytes exhibiting mitochondrial depolarization increased rapidly within 15 minutes after impact, followed by a more gradual rise for the duration of the experiment (Figure 3.3, black lines). For these untreated samples, cell death also increased gradually over the experiment, in agreement with previous results[84]. Indeed, without treatment, both mitochondrial dysfunction and cell death were each higher in impacted samples, as compared to no-impact controls ($p<1.2\times10^{-6}$ for all $t>0$ min against the null hypothesis that impact does not affect the response). As expected, the no-impact control groups showed only slight depolarization at the end of the experiment and negligible cell death throughout, regardless of treatment ($p>0.01$ for all $t>0$ min, against the null hypothesis that, without impact, treatment does not affect response). After treatment, while impact still induced more mitochondrial dysfunction ($p<1.8\times10^{-8}$ for $t>0$ min) and cell death ($p<2.6\times10^{-11}$ for $t>3$ min) as compared to no impact, the level of dysfunction was dramatically lower. In fact, treatment with SS-31 peptide significantly suppressed both the mitochondrial depolarization and cell death observed after impact (Figure 3.3, blue lines; $p<1.1\times10^{-3}$ for all $t>0$ min against the null hypothesis that treatment does not affect depolarization in impacted samples; $p<4.5\times10^{-3}$ for $t\subset[9, 30]$ min against the null hypothesis that treatment does not affect cell death in impacted samples).

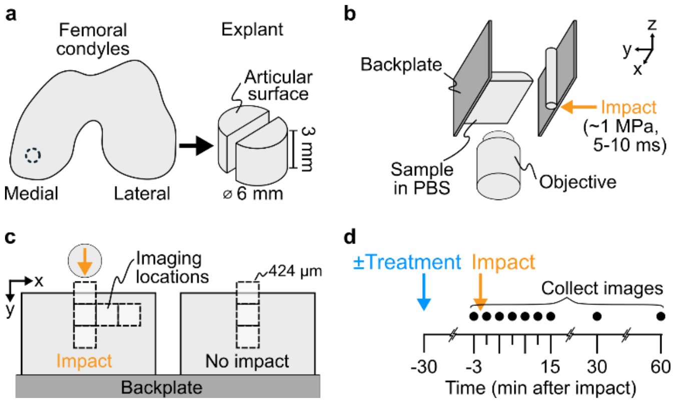

Figure 3.1. Experimental methods. (a) Cylindrical explants were dissected from medial condyles of bovine stifles and bisected to created paired samples. (b) Samples were stained with a 3-color assay for mitochondrial polarity and mounted to the stable backplate of a custom impactor. This test frame was subsequently mounted on a confocal microscope. (c) Paired hemi-cylindrical samples were mounted side-by-side on the backplate such that the two were in the same fluid bath but only one was impacted, while the second served as a non-impacted control. Samples were imaged at various locations relative to the impact (8 square fields of view; 5 on the impacted sample, 3 on the non-impacted sample). (d) Samples were imaged at all locations longitudinally, including before and up to 60 minutes after impact. For treated samples, SS-31 peptide treatment was added to the PBS bath surrounding both hemi-cylinders 30 minutes before the first image.

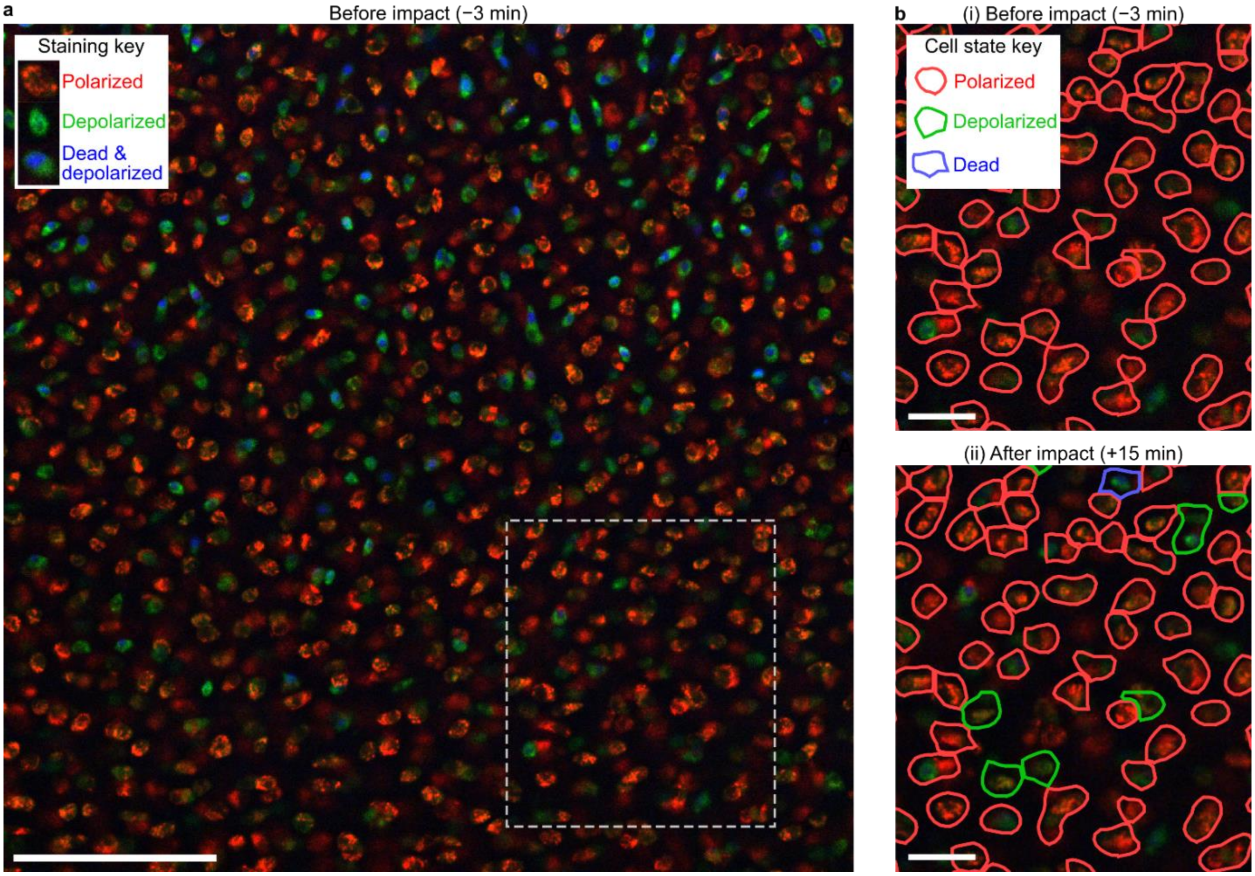

Figure 3.2. Image segmentation and cell classification. (a) An image taken at the first time point, immediately before impact, shows characteristic staining pattern. In this mitochondrial assay, red staining highlights polarized mitochondria, green staining highlights all mitochondria regardless of polarity, and blue staining highlights dead cell nuclei. Dashed rectangle indicates region highlighted in (b). Scale bar indicates 100 µm. (b) Images were subsequently analyzed to segment and classify cells as indicated by colored outlines. Cell state, as determined by the color distribution in each cell, is indicated by the color of the segmentation outline. (i) Only cells that had polarized mitochondria (red outlines) before impact were tracked longitudinally. (ii) Observing the same location at 15 minutes after impact, some cells changed from polarized to depolarized (green outline) or dead (blue outline). Scale bar indicates 25 µm.

Figure 3.3. Mechanical impact induces rapid mitochondrial depolarization and gradual cell death that are both significantly reduced by SS-31 treatment. (a) Without treatment (black lines), the average fraction of cells with depolarized mitochondria increased dramatically in the first 15 minutes after impact and was higher in impacted samples as compared to non-impacted controls ($p<1.3\times10^{-41}$). With treatment (blue lines), impacted samples showed dramatically less depolarization ($p<1.1\times10^{-3}$), especially in the first 15 minutes, while non-impacted controls were unaffected by treatment ($p>0.01$). (b) Fractional cell death in impacted samples was smaller and increased gradually over time but was still significantly reduced by SS-31 treatment ($p<4.5\times10^{-3}$, 9-30 min after impact). Points show the mean across samples (i.e. animals) and error bars indicate standard error of the mean. Untreated and treated results reflect the responses of samples from 5 and 4 animals, respectively. Statistical comparisons were evaluated using mixed effects models (Table 3.1, Table 3.2).

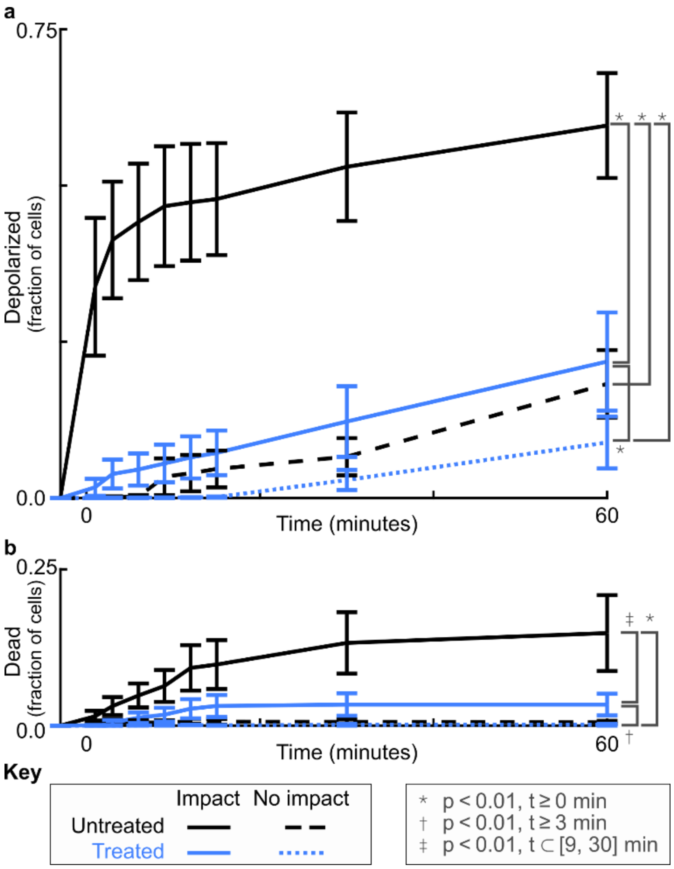

a
0.75
0.0
Depolarized
(fraction of cells)
0
60
Time (minutes)
*
*
*
*
b
0.25
0.0
Dead
(fraction of cells)
0
60
Time (minutes)
‡
*
†
Key
Impact
No impact
Untreated
Treated
* p < 0.01, t ≥ 0 min
† p < 0.01, t ≥ 3 min
‡ p < 0.01, t ⊂ [9, 30] min

3.3.2 Strain-dependence of peracute mitochondrial dysfunction

To establish the role of mitochondria in mediating mechnotransduction during injury, we correlated mitochondrial dysfunction with the mechanics of impact. In a separate set of samples, hemi-cylinders were marked with fluorescent microspheres and imaged during rapid impact injury using a fast-camera (7.1, Vision Research, Wayne, N)[104]. Fast-camera movies were analyzed using digital image correlation[105] and averaged to compute the local strain tensor field experienced during injury at maximum indentation. In order to relate cell state data with strain data, cells tracked via confocal microscopy were binned in 2D, using the same spatial grid as the strain analysis. For each spatial bin this produced both an average strain tensor and the average fraction of cells in each state. Using a mixed-effects model, we evaluated these correlations over varying impact and treatment conditions.

We found that spatial patterns of and correlations between mitochondrial function and impact strain support our two hypotheses: mitochondrial depolarization after impact is mechanically-mediated and SS-31 treatment prevented this mechanically-dependent dysfunction. At 15 minutes after impact, the average fractional mitochondrial depolarization in untreated samples was highest near the impact location and decreased further away (Figure 3.4a). In contrast, samples treated with SS-31 peptide showed much less mitochondrial depolarization with no obvious spatial pattern (Figure 3.4b). The local average strain tensor field, as characterized by the Lagrange strain norm at peak indentation, was also highest near the impact and decreased further away (Figure 3.4b). Correlating mitochondrial dysfunction with the impact strain shows that, without treatment, mitochondrial depolarization 15 minutes after impact was highly correlated with the Lagrange strain norm during impact (Figure 3.4c(i), black points; Pearson correlation coefficient R=0.68; mixed-model slope m=2.4; $p=6.0\times10^{-300}$ against the null-hypothesis of zero strain dependence). In contrast, SS-31 peptide treatment not only reduced the level of mitochondrial depolarization, but also reduced the correlation between strain and depolarization, confirming that SS-31 targets the mechanically-dependent mitochondrial dysfunction (Figure 3.4c(i), blue points; R=0.07; m=0.070; p=0.23 against the null hypothesis of zero strain dependence; $p=7.5\times10^{-131}$ against the null hypothesis of the same strain dependence regardless of treatment). All non-impacted samples experienced zero impact strain, by definition, and showed negligible mitochondrial depolarization with no obvious spatial pattern, as expected (Figure 3.4a,b,c(ii)). The full strain fields and time-dependent correlations are detailed in Figure 3.6 and Figure 3.7. The statistical model used to evaluate relationships is detailed in Table 3.3. Collectively, these results demonstrate that mitochondria function is strongly dependent on tissue strain and support the hypothesis that mitochondria mediate chondrocytes' response to injury. Because mitochondrial function depends on its inner membrane structure, these results suggest that impact may induce structural changes in mitochondria, as well.

Figure 3.4. Treatment with SS-31 eliminates strain-dependent mitochondrial depolarization. (a) (i) Without treatment, the local fraction of cells with depolarized mitochondria is high near the impact location and decreases farther away, while non-impacted samples show nearly zero depolarization. (ii) In contrast, samples treated with SS-31 show minimal depolarization after impact, while depolarization in non-impacted samples remains nearly zero. Scale bar indicates 250 µm. (b) At peak displacement during impact, Lagrange strain norm is highest near the impact and decreases further away, while no-impact samples have zero strain, by definition. Scale bar indicates 250 µm. (c) (i) In impacted but untreated samples, depolarization is correlated with the local strain ($p=8\times10^{-308}$), but after SS-31 treatment this correlation is eliminated ($p>0.01$). Each point corresponds to one spatial bin. Lines indicate the best fit and m values indicate the associated strain norm coefficients (i.e. slope). Note: * indicates significantly reduced strain correlation after treatment ($p=2\times10^{-103}$). (ii) A Tukey box plot shows the distribution of fractional depolarization in non-impact samples (zero strain), which remains low for both treatment groups. All plots show depolarization at 15 minutes after impact and Lagrange strain at peak displacement during impact. Untreated and treated results reflect the response of paired samples from 5 and 4 animals, respectively. Statistical comparisons were evaluated using a mixed effects model (Table 3.3).

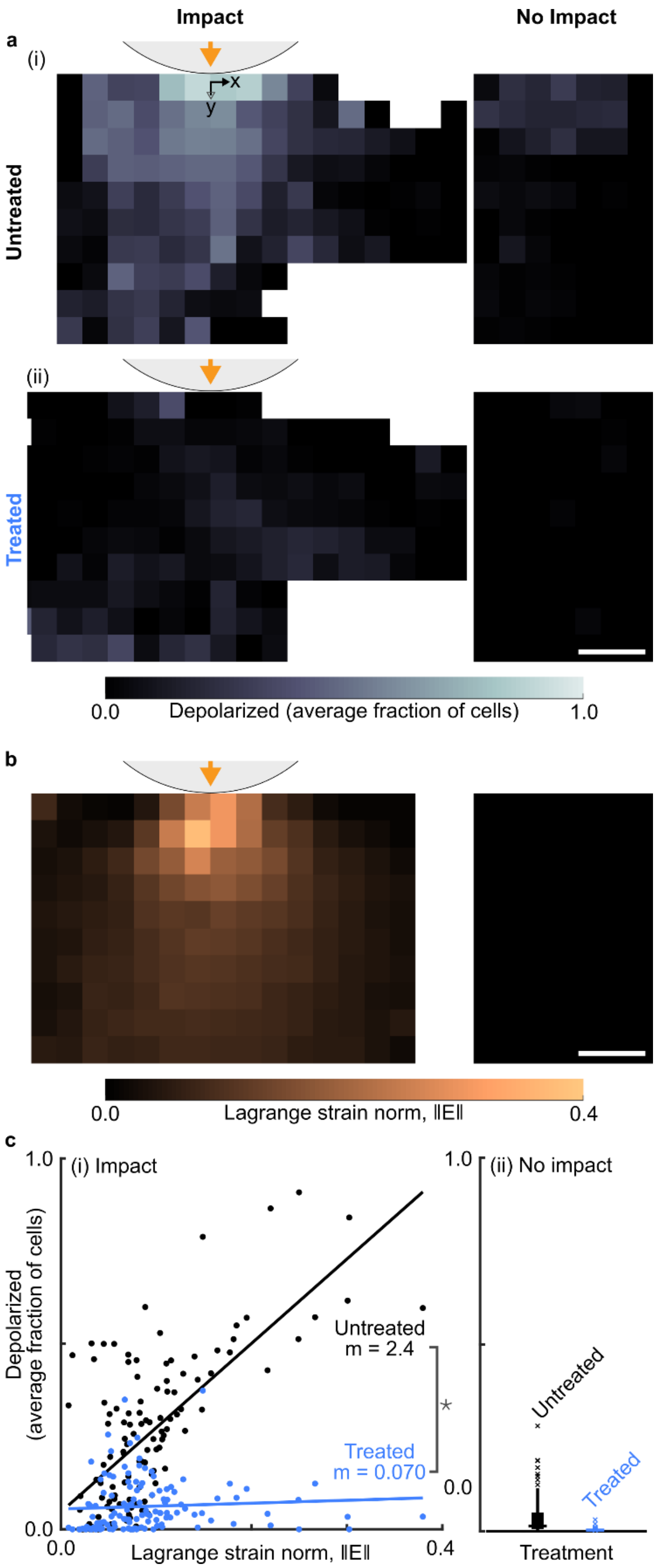
Impact
No Impact
a
(i)
x
y
Untreated
(ii)
Treated
0.0
Depolarized (average fraction of cells)
1.0
b
0.0
Lagrange strain norm, ‖E‖
0.4
c
1.0
(i) Impact
Depolarized (average fraction of cells)
Untreated
m = 2.4
*
Treated
m = 0.070
0.0
0.0
Lagrange strain norm, ‖E‖
0.4
1.0
(ii) No impact
Untreated
Treated
0.0
Treatment

3.3.3 Structural changes in mitochondria after impact

We used transmission electron microscopy (TEM) to investigate the mitochondrial structure and morphology. Separate samples were impacted as described above but without fluorescent staining. As before, a subset of samples were treated with 1 µM SS-31 before impact. Samples were fixed 30 minutes after impact, sections were harvested from the tissue immediately below the impact location, and TEM images were collected at 120 kV.

Chondrocytes in no-impact samples displayed normal, elongated mitochondrial morphology with distinct cristae structure in the inner mitochondrial membrane (Figure 3.5a). After impact, however, chondrocytes were consistently abnormal, with swollen mitochondria and little to no apparent cristae structure (Figure 3.5b). In contrast, samples that were treated with SS-31 peptide maintained normal mitochondrial morphology and retained cristae structure after impact (Figure 3.5c).

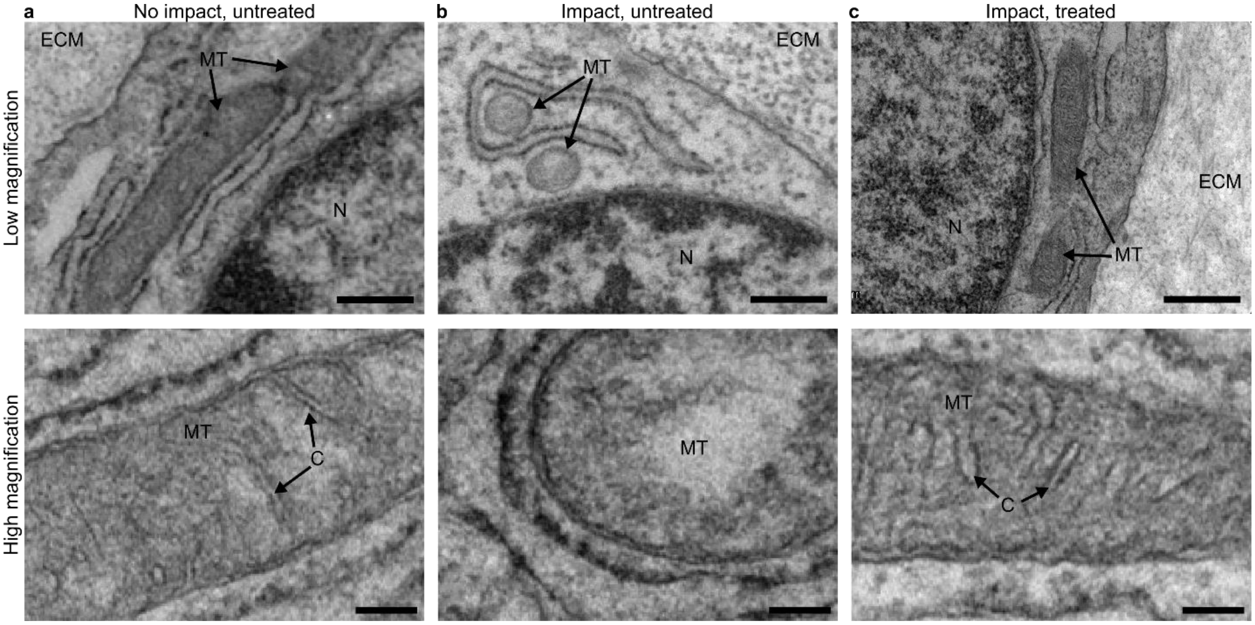

Figure 3.5. Electron microscopy reveals that SS-31 treatment preserves cristae structure in mitochondria. (a) Chondrocytes in an untreated, non-impact sample display normal, elongated mitochondrial morphology (top) and well-defined cristae structure (bottom). (b) After impact, untreated mitochondria appear ovate, swollen and lack cristae structure. (c) In contrast, samples treated with SS-31 have normal mitochondrial morphology with preserved cristae structure after impact. For imaging, samples were fixed 30 minutes after impact and images were collected in locations directly under the impact, corresponding to the imaging locations outlined in Figure 3.1c. Text and arrow labels on each image indicate extracellular matrix (“ECM”), mitochondria (“MT”), nucleus (“N”), and cristae (“C”). In low magnification images (top row) scale bar indicates 500 nm. In high magnification images (bottom row) scale bar indicates 100 nm.

3.4 Discussion

Recent evidence suggests that mitochondria are important to cartilage's response to injury and may be a promising therapeutic target. However, important knowledge gaps remain, especially regarding the role of mitochondria in mediating cartilage's response to mechanical injury, the time-frame over which their response develops, and if there are structural and functional changes in mitochondria that present druggable targets for cartilage injury. To investigate the role of mitochondria in cartilage's response to injury, we tracked individual chondrocyte behavior with longitudinal fluorescence assays and utilized TEM imaging of mitochondrial structure, revealing the peracute development of cellular dysfunction after impact.

Our results showed that mitochondria depolarize within 15 minutes after impact and this depolarization was highly correlated with the strain experienced during injury, implicating mitochondria as important mediators of cartilage's injury response. This depolarization response is much faster than previously-observed effects, including the initial wave of necrotic cell death that develops within a few hours after injury[40,74,81,84], indicating that mitochondrial dysfunction is one of the first consequences of cartilage injury. Furthermore, the high correlation between strain norm and mitochondrial depolarization indicates that much of the observed cellular dysfunction can be directly attributed to the local strain experienced during injury. This correlation parallels the mechanical-dependence of the non-specific (likely necrotic) cell death observed previously[40,84], implying that mitochondrial dysfunction may also mediate the known wave of peracute chondrocyte death after injury. Notably, while a large fraction of cells exhibited mitochondrial dysfunction, a smaller fraction exhibited cell death, indicating that not all peracute mitochondrial dysfunction evolves immediately into cell death. Not only is this observation in agreement with previous studies[91], but it reflects the complex peracute-to-acute evolution of chondrocyte injury responses[89]. Note that there was a non-zero amount of cellular dysfunction observed in control samples (Figure 3.8), which likely results from the imperfect environmental conditions during imaging, including laser exposure and the PBS bath at room-temperature and atmospheric oxygen. Nonetheless, the level of dysfunction in control samples evolved slowly and was small compared to that induced by impact. Importantly, electron microscopy of chondrocyte mitochondria from impacted samples revealed structural changes in mitochondria after injury, inducing globular morphology and loss of cristae structure, both of which are hallmarks of mitochondrial dysfunction[97]. These changes also match those observed previously, including mitochondrial fusion and fission in response to stress, as well as fragmentation from tubular to globular shape within ten minutes after chemically-induced depolarization[106,107]. Moreover, it is known that mitochondrial cristae dynamically modulate the kinetics of energy production in cells and that loss of cristae impairs cellular metabolism, further suggesting that cristae structure may be a promising therapeutic target, in general[108]. As such, our observed changes in mitochondria structure can explain the loss of mitochondrial polarity that was directly observed in this study via confocal fluorescence imaging. Moreover, it is known that mitochondria are mechanically connected to the intra- and extracellular networks such that cell strain leads to mitochondrial strain[93]. Collectively, these results support a peracute mechanism by which impact strain leads to mitochondrial membrane damage and depolarization as well as other downstream effects, including cell death.

To show that protecting mitochondrial structure is a potential therapeutic target for preventing this strain-induced dysfunction, we tested the effect of a promising new peptide, SS-31. Our results showed that SS-31 treatment before impact dramatically reduced mitochondrial depolarization. Notably, treatment targeted the mechanically-dependent depolarization, as evidenced by the loss of correlation with strain after treatment. Mitochondrial protection was confirmed by electron microscopy, which further showed that SS-31 treatment before impact preserved mitochondria tubular morphology and cristae structure after impact. Because mitochondrial structure and function are linked[108], this preservation of mitochondrial morphology may explain the corresponding retention of polarity observed via fluorescence. Moreover, these results show that, in chondrocytes, SS-31 acts to preserve mitochondrial structure. While a recent study showed that SS-31 treatment can reduce impact-induced chondrocyte apoptosis in the acute time frame after cartilage injury (i.e. days)[89], this study further shows that pretreatment with peptide can also dramatically reduce the peracute (i.e. minutes to hours) cellular dysfunction and death. The previously-observed acute mitoprotection by SS-31 likely involves protection against oxidative damage via absorption of reactive oxygen species[98,109,110], but these mechanisms of action take hours to develop and so the peracute protection observed in this study further suggests another, more immediately beneficial mechanism of mitoprotection which remains unknown.

Although the complete mechanisms of mechanotransduction and mitoprotection in cartilage remain an active area of research, SS-peptides are a particularly promising therapeutic. SS-peptides have shown promise for treating other mechanically-induced mitochondrial-based diseases, including glaucoma and ischemia reperfusion injury, and have proven safety and efficacy in clinical trials[100,111]. Moreover, SS-31's mechanism of protecting mitochondrial structure and morphology is farther upstream, as compared to apoptotic responses that are likely mediated through the mitochondria[89,91,108]. Additionally, though this study only tested pretreatment, SS-31 can also reduce chondrocyte death and cartilage matrix degeneration when treating up to 6 hours after injury in an *ex vivo* system[89]. This *ex vivo* study also showed that SS-31 can diffuse through the dense cartilage matrix[89]. Overall, SS-31 is protective of mitochondrial structure and function and a promising potential treatment for injury-induced cartilage dysfunction that warrants further study *in vivo*.

A further methodological implication of this study is to demonstrate the utility of image tracking, segmentation, and classification techniques for advancing scientific knowledge with microscopy-based assays. Here, these automated techniques enabled us to track thousands of individual cells over space and time, facilitating both better statistics (i.e. more cells) and quantifiable correlations, especially in concert with local mechanical measurements. However, the methodological implications are much farther reaching. Fluorescence microscopy assays are commonly employed to observe cells *in vitro* and *in situ*, both within and beyond the field of orthopedic mechanobiology. Indeed, similar techniques are broadly applicable for any study that uses microscopy and fluorescence to assay cellular function. By developing the techniques in this study, we hope to champion the broad utility of computer vision and machine learning across orthopedic mechanobiology and beyond.

Overall, by combining advanced techniques to understand local mechanics and cellular dysfunction, this study revealed the importance of mitochondria in cartilage's response to traumatic injury. Our results show that mitochondria are central to chondrocyte's response to trauma and that their structural degradation presents a promising therapeutic target. Indeed, the rapidity of the responses observed here and the fact that mitochondria are mechanically connected to their environment suggests that mitochondria could act as mechanotransducers during cartilage injury, independent of other, more classically studied pathways. Importantly, this study also shows that SS-31 acts to protect mitochondrial structure and function in cartilage. Collectively, this study of rapid impact mechanics and peracute mitochondrial dysfunction in cartilage is an important step toward understanding the pathogenesis of post-traumatic osteoarthritis and targeting mitochondria for treatment.

3.5 Methods

3.5.1 Sample preparation

Cylindrical explants, 6 mm diameter and 3 mm deep were dissected sterilely from the apex of the medial femoral condyle of neonatal bovines (1 explant per animal, N=9 animals; Figure 3.1a). Cylinders were cultured for approximately 8 hours in media (culture conditions: 37°C, 21% O_2, 5% CO_2; media formulation: phenol free DMEM containing 1% FBS, HEPES 0.025 ml/ml, penicillin 100 U/mL, streptomycin 100 U/mL and 2.5 mM glucose). Explants were then bisected and maintained at room-temperature PBS for the remainder of experimentation.

3.5.2 Fluorescence assay of cellular function

To observe mitochondrial function and cell death, paired hemi-cylinders were stained with a 3-color fluorescence assay: (1) 30 minute incubation in 10 nM tetramethylrhodamine, methyl ester (TMRM), which concentrates in mitochondria based on the proton gradient across their inner membrane, thus reflecting mitochondrial polarity (i.e. potential); (2) 50 minute incubation in 200 nM MitoTracker Green, which localizes to all mitochondria regardless of polarity; (3) 30 minute incubation in 100 nM Sytox Blue, a cell-impermeant nucleic acid stain which therefore stains dead cell nuclei (all stains: ThermoFisher Scientific, Waltham, MA). After staining, paired hemi-cylinders were mounted side-by-side to the impactor and suspended in a bath of PBS throughout the remainder of the experiment. This bath included 100 nM Sytox Blue, in order to ensure that cells dying during the course of the experiment would take-up stain from the bath. For treated samples, 1 μM SS-31 peptide (provided by H. Szeto) was added to the bath and samples sat unperturbed in the bath for 30 minutes before proceeding with the experiment.

3.5.3 Impact device

In order to induce injury, samples were impacted using a custom impact device that utilizes a spring-loaded piston to deliver an energy-controlled impact[84,104]. Paired hemi-cylindrical samples were mounted side-by-side to the stable backplate of the impactor, as described previously[84], such that one hemi-cylinder was centered in the path of the impact while the second served as a no-impact control (Figure 3.1c). Samples were impacted with an 8 mm diameter stainless-steel rod, inducing a range of strains in a relatively small field of view. Based on previous characterization, this impact induced a peak stress of ~1 MPa and lasted about 5-10 ms. This loading rate and the magnitude of tissue-level strains were comparable to those that may be experienced *in vivo* during injurious, super-physiologic loading[28]. Note that, although the impact geometry does not mimic physiologic loading, it can impose a wide variety of strains at super-physiologic loading rates in a relatively small field of view, thus enabling correlations between impact strain and cellular function. Physiologic loading would induce a different distribution of strains in the tissue, but the response of cells to the microscale strain in their surroundings would not be expected to change. Also note that both hemi-cylinders shared the same fluid bath throughout experimentation. As such, this setup did not prohibit potential signaling between the two samples before or after impact[112].

3.5.4 Confocal imaging of cellular function

To image the fluorescence assay longitudinally, the impact device was mounted on an inverted, point-scanning confocal microscope with a 20× objective (LSM 880, Zeiss, Oberkochen, Germany). In this setup, the confocal views the depth-profile of the two hemi-cylinders, as depicted in Figure 3.1b,c, with a square field of view, 424 µm (1024 pixels) on a side. Images were collected at 8 difference locations (5 adjacent views on the impacted hemi-cylinder, and 3 on the no-impact hemi-cylinder, as depicted in Figure 3.1c). Images at each location were also collected longitudinally over time, 3 minutes before impact, and 0, 3, 6, 9, 12, 15, 30, and 60 minutes after impact (0 was immediately after impact, ~30 seconds), as outlined in Figure 3.1d. Images were collected with three color channels corresponding to the three-stain fluoresce assay: TMRM (polarized mitochondria) was excited at 561 nm, detected at 563 nm to 735 nm, and stored in the red channel; MitoTracker Green (all mitochondria) was excited at 488, detected at 499 nm to 553 nm, and stored in the green channel; Sytox Blue (dead cells) was excited at 405 nm, detected at 414 nm to 479 nm, and stored in the blue channel. A characteristic image from one location is shown in Figure 3.2a.

3.5.5 Image analysis of cellular function

Confocal images at all locations and time points were analyzed to extract individual-cell behavior over time. This analysis included three steps: registration, segmentation, and classification, all of which were performed using MATLAB (The MathWords, Waltham, MA). Density estimates were then used to compute local variations in the fraction of cells in each state.

Registration. Confocal images at each imaging location were registered over time to correct for drift in the microscope stage. Intensity-based registration was performed between adjacent time points, allowing for rigid-body translation only. All images were then transformed back to the first time point's frame of reference and regions in the newly-transformed space that no longer had complete time information were discarded (i.e. regions of the sample that move out of the field of view).

Segmentation. Images at the first time point were segmented to locate individual cells. Segmentation was performed using a previously-described algorithm based on the watershed transform[113], using parameters that were chosen to match the manually-counted cell density in a test image: equalization clip limit: 0.01; background size: 23 px; median size: 7 px; Gaussian radius: 9 px; minimum area: 300 px^2; maximum area: 5000 px^2; minimum signal: 0.1, i.e. 10% of full range. The resulting segmentation defines regions (i.e. cells) at the first time point. These same regions were also valid at all subsequent time points, since images had been transformed back to the first time point and chondrocytes are not mobile in their native tissue environment.

Classification. Each identified cell was analyzed at each time point to classify it into one of three possible states: alive with polarized (i.e. functional) mitochondria, alive with depolarized mitochondria, and dead. For classification, scalar features were calculated for each cell at each time point and these features were then thresholded. Given the distribution of pixel intensities inside each cell region at a given time point, the following features were calculated: the 96th percentile of blue pixel values ($B_t^{(96)}$), the 88th percentile of red pixel values ($R_t^{(88)}$), and the relative change in the 90th percentile of the red pixel values ($\bar{R}_t^{(90)} = \left(R_t^{(90)} - R_0^{(90)}\right)/R_0^{(90)}$), where $A_j^{(i)}$ is the ith percentile of pixel values in channel A at time j. The corresponding thresholds were $T_1 = 63$, $T_2 = 27$, and $T_3 = -0.4$ (i.e. 40% loss), respectively, where pixel values were 8-bit (i.e. ranging from 0 to 255). At the first time point, cells with $B_0^{(96)} \leq T_1$ and $R_0^{(88)} > T_2$ (i.e. without Sytox Blue staining and with strong TMRM staining) were marked as alive with polarized mitochondria. All cells not meeting this criteria at the first time point (i.e. cells that were dead or depolarized at the start of the experiment) were marked as invalid and not analyzed further. Within the cells that were alive and polarized at the start of the experiment, those with $B_t^{(96)} > T_1$ were marked as dead. Within the remaining cells that were alive and polarized at the start of the experiment and also not dead at time *t*, those with $\bar{R}_t^{(90)} < T_3$ (i.e. those that had lost more than 40% of their original TMRM signal) were marked as alive with depolarized mitochondria. These features, the percentile levels, and their thresholds were all chosen to optimize the classification accuracy, as calculated from the confusion matrix produced by applying the classification to a subset of 546 cells that had been manually classified. Notably, the relative change in red signal (i.e. TMRM signal) over time was a better classification metric for loss of mitochondrial polarity than measures of the absolute intensity. This is intuitive, since even normal chondrocytes may have varying number of mitochondria with varying levels of polarity. As such, the relative loss of TMRM signal would be a better indicator of within-cell mitochondrial changes than the absolute intensity at a given time point. This observation reinforces the importance of following individual cells over time, rather than measuring population-averaged metrics at each time point.

Density estimates. The fraction of cells in each state was computed on a 100 µm spatial grid relative to the impact location. For each sample, Gaussian kernel density estimates were computed at each grid point, to determine the local number of cells in each state (polarized, depolarized, dead), as well as the total number of cells. Fractional state occupancy was computed by dividing by the total cell density, and areas that had less than 30 cells/mm^2 total were discarded, in order to ensure adequate counting statistics. To compute average temporal trends, as shown in Figure 3.3, cell state data was averaged using cells within 212 µm of the impact laterally and 1000 µm deep

3.5.6 Validation of experimental setup and cellular function assay

In order to test the baseline level of cellular dysfunction arising due to systematic and environmental conditions, a no-impact control experiment was performed. For this variant, one pair of hemi-cylindrical samples was prepared, imaged, and analyzed as described above, except neither sample was impacted (from N=1 additional animal). In this situation, results showed negligible cell death and minimal depolarization (Figure 3.8, blue lines). This confirms that the experimental conditions induce minimal cellular dysfunction and thus the main results of this study are not masked by environmentally-induced changes.

In order to validate the three-stain assay used to assess cellular function, two comparison experiments were performed. For each of these comparisons, a pair of hemi-cylinders was prepared as described above, except neither sample was impacted (from N=2 additional animals). For each comparison, images were collected at 0, 30, and 60 minutes and analyzed as described above. In the first comparison, 4 µM FCCP (carbonyl cyanide *p*-trifluoromethoxyphenylhydrazone; Sigma Aldrich, St. Louis, MO) was added to the impactor's fluid bath immediately after the first imaging time point. FCCP is an ionophore that causes mitochondrial depolarization by dissipating the proton gradient (transporting protons) across the inner mitochondrial membrane. For the second comparison, 2 μM oligomycin (Sigma Aldrich) was added to the impactor's fluid bath immediately after the first imaging time point. Oligomycin causes hyperpolarization of the inner mitochondrial membrane by blocking the proton channel subunit of ATP synthase. As expected, after adding FCCP to the bath, nearly all of the cells were classified as alive with depolarized mitochondria (Figure 3.8, orange lines). After adding oligomycin to the bath, nearly all cells remained classified as alive and polarized (Figure 3.8, yellow lines), following the same trend observed in the no-impact control. In both cases, there was negligible cell death throughout the experiment, as expected. These two comparisons confirm that the staining assay and analysis procedure used in this study can appropriately capture changes in mitochondrial polarity over time.

3.5.7 Electron microscopy of mitochondrial structure

To assess mitochondrial morphology and structure, two hemi-cylinder pairs were prepared and impacted as described above, but without fluorescent staining. One pair was treated with SS-31 as described above, while the other was not. For each pair, samples were incubated at room temperature for 30 minutes after impact, then and fixed for transmission electron microscopy (TEM) imaging, as follows: First, samples were transferred to a petri dish on ice containing 2% Gluteraldehyde in 0.05M cacodylate buffer and fixed for 2 hours. Second, samples were then rinsed in cacodylate buffer and placed in 1% Osmium Tetraoxide for one hour on ice. Third, samples were rinsed and dehydrated in graded (increasing) concentrations of Ethanol (25%, 50%, 70%, 95%, 100%), stained in 2% Uranyl Acetate in ethanol for 2 days, then placed in anhydrous acetone prior to stepwise embedding in 25%, 50%, 75% then 100% epoxy (EMbed 812, Electron

Microscopy Sciences, Hatfield, PA). Finally, samples were sectioned and imaged on an FEI Tecnai 12 BioTwin Transmission Electron Microscope (ThermoFisher Scientific, Waltham, MA) at 120kV, and 4008×2672 digital images were captured using a Gatan Orius® 1000 dual-scan CCD camera (Roper Technologies, Sarasota, FL), using Digital Micrograph (Gatan, Inc., Pleasanton, CA) software.

3.5.8 Fast camera elastography

Fast-camera elastography was used to track local strains in articular cartilage during rapid impact injury. For strain analysis, three hemi-cylindrical samples were obtained as described above, but were tested within 5 hours of dissection and not cultured overnight or treated with SS-31. Samples were not stained with the three-stain cellular function assay, but were instead coated with fluorescent microspheres, as described previously[104]. Samples were mounted to the impactor in a PBS bath, as described above, and the sample was imaged using a 10× objective and a high-speed camera (v7.1, Vision Research, Wayne, NJ) with illumination from a mercury arc lamp (HBO 100, Carl Zeiss Inc., Germany), thus enabling epi-fluorescence microscopy at 4,000 frames per second. In order to calculate local strain tensors in the sample at peak indentation, each of the three resulting fast-camera videos was analyzed using Ncorr, a 2D digital-image correlation tracking software (subset radius: 35 px; subset spacing: 5 px; strain radius: 5 points)[105]. For each independent strain tensor component, strain fields from all samples were shifted to place the point of impact at the origin, and Barnes smoothing interpolation was implemented to compute the average strain field on the same 100 μm spatial grid (relative to the impact location) that had been used to compute cell state density estimates[114].

3.5.9 Statistical analysis

Mixed-effects linear models were used to evaluate spatially-binned cell-state data and investigate significant trends across time, impact condition, impact strain, and treatment condition. The effects of time, impact condition, and treatment condition were evaluated as categorical variables, while strain was a continuous variable. The models also included a random effect for source animal and significance was set at $p<0.01$. For each model, the response variable was transformed to ensure normal residuals. When fitting, each model was reduced and residuals were checked for normality and homogeneity. After fitting, various statistical comparisons were evaluated using F-tests of the associated model contrasts with a Satterthwaite approximation for the degrees of freedom. Because impact state and strain are not independent (no-impact samples have zero strain, by definition), three models were fit to evaluate three slightly different objectives while maintaining linear independence of the effect variables. Similarly, since all observed cells were functional before impact, by definition, models were only fit to data after impact, namely time points 0 min through 60 min, inclusive (-3 min excluded). First, to evaluate temporal trends shown in Figure 3.3, two linear models were fit, including all variables except strain. One model was fit using the fraction of dysfunctional cells as the response variable while the second model used the fraction of dead cells as the response. Next, to investigate the relationship between strain and fractional depolarization, as shown in Figure 3.4, a linear mixed-effects model was fit to the fractional depolarization from impacted samples only, including strain norm during impact but not impact state.

3.6 Acknowledgements

L.R.B. was supported by the National Institutes of Health under award number 1F31-AR069977. M.L.D. was supported by Weill Cornell Medical College Clinical and Translational Science Center Award Seed Grant 5UL1 TR000457-09, NIH Mentored Clinical Scientist Development Award 1K08AR068470, NIH Comparative Medicine Training Grant T32RR007059 and the Harry M. Zweig Fund for Equine Research. The authors would also like thank Lynn Johnson at the Cornell Statistical Consulting Unit and Hazel Szeto for useful discussions.

3.7 Supplementary information

3.7.1 Lagrange strain field during impact

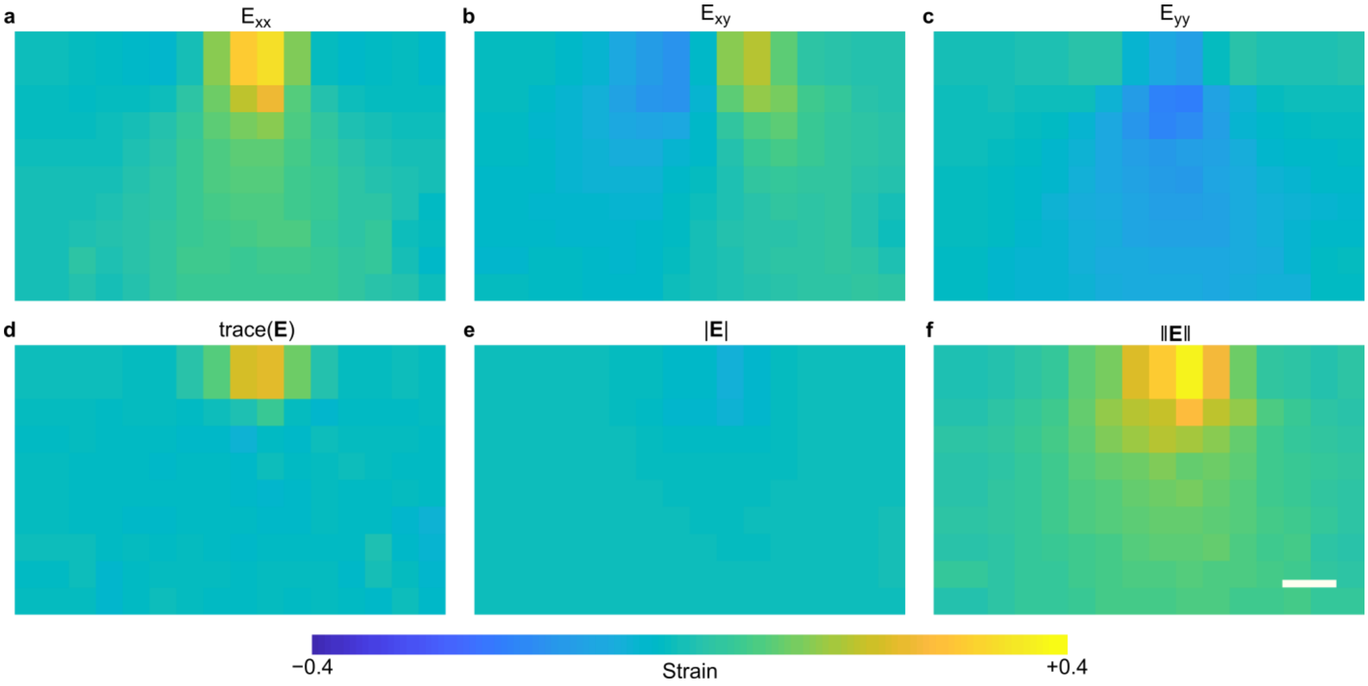

Figure 3.6. Average components and scalar measures of the Lagrange strain during impact. Strain fields are shown for the various strain measures tested, including: (a) Exx, the axial strain in the lateral direction, (b) Exy, the shear strain, (c) Eyy, the axial strain in the depth direction (parallel to the impact), (d) the trace of the strain tensor (first invariant), (e) the determinant of the strain tensor (second invariant), and (f) the spectral norm of the strain tensor. These strain measures were derived from the average 2D Lagrange strain tensor in each spatial bin at peak indentation during impact. Scale bar indicates 200 µm.

3.7.2 *Correlations between cellular dysfunction and strain over time*

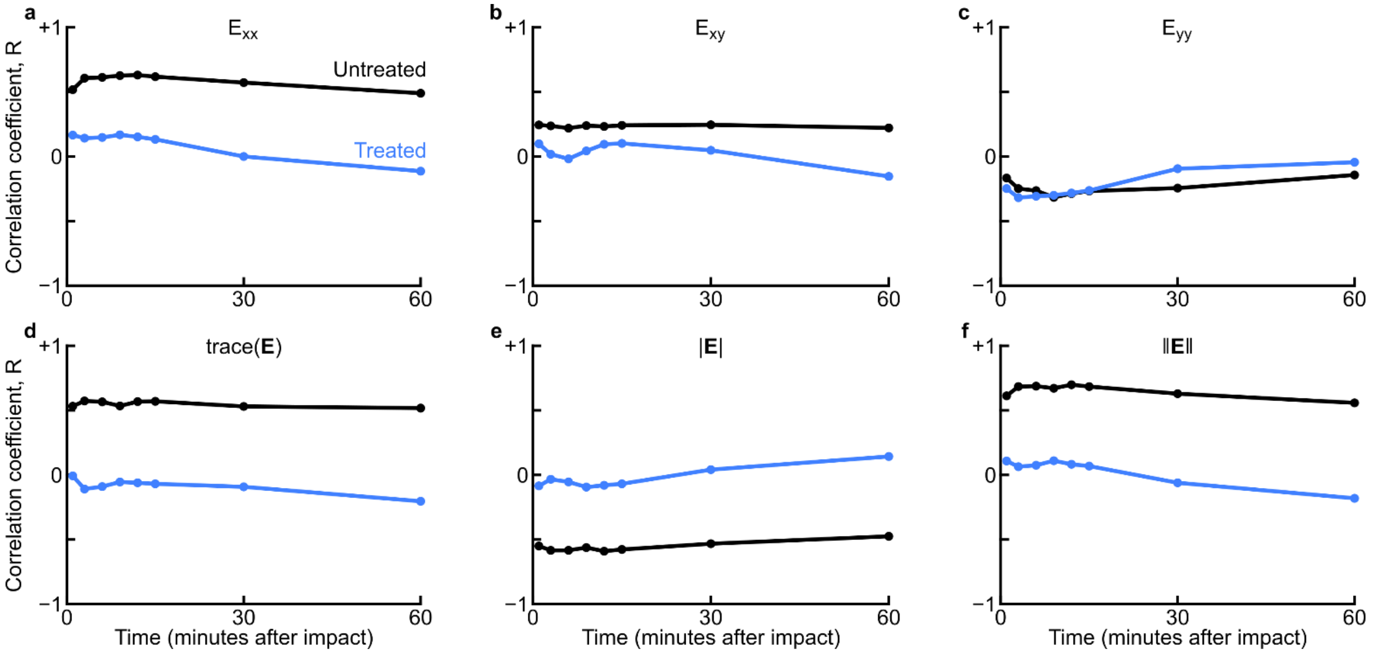

Figure 3.7. Correlations between fractional depolarization and strain are weaker after treatment but are consistent over time. Each plot shows the correlation coefficient between the average fraction of depolarized cells in each spatial bin over time and a corresponding strain measure, including: (a) Exx, the axial strain in the lateral direction, (b) Exy, the shear strain, (c) Eyy, the axial strain in the depth direction (parallel to the impact), (d) the trace of the strain tensor (first invariant), (e) the determinant of the strain tensor (second invariant), and (f) the spectral norm of the strain tensor. These strains were calculated from the average 2D Lagrange strain tensor in each spatial bin at peak indentation during impact and were correlated with the average fraction of depolarized cells in that same spatial bin. In general, the correlation is consistent over time and treatment reduces the correlation (R closer to zero). Additionally, the correlation is strongest for the strain norm, representing the overall magnitude of strain.

3.7.3 *Validation of experimental method and mitochondrial polarity assay*

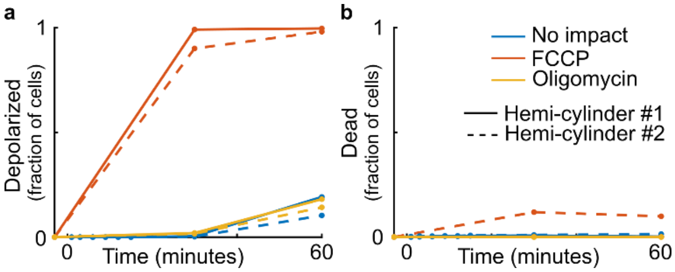

Figure 3.8. Validation of experimental method and mitochondrial polarity assay. (a) Repeating the experimental method with no treatment and no impact on either hemi-cylinder showed low, but non-zero mitochondrial dysfunction over time, reflecting systematic effects inherent to the method. The mitochondrial polarity imaging assay was validated by repeating the experiment (no impact and no treatment) with the addition of either FCCP or oligomycin at time zero. (a) As expected, nearly all observed chondrocytes showed depolarization when exposed to FCCP, while chondrocytes exposed to oligomycin retained full mitochondria polarity, paralleling the results in for the no-impact group. (b) In all cases, there was negligible cell death, as expected.

3.7.4 *Statistical models*

Various linear mixed-effects models were fit to the data to test for significant trends and difference between testing conditions. In all cases, models were fit and reduced in MATLAB using `fitlme` and further statistical contrasts and associated p-values were computed using the method `coefTest`. All models included a random effect of source animal on the intercept. Residuals were checked for normality and homogeneity and response variables were transformed to ensure normal residuals. Sample treatment condition and impact condition were encoded as binary variables.

Time was also treated as a categorical variable, including time points #2-9, corresponding to 0 through 60 minutes after impact. The time point collected before impact was excluded because all tracked cells were alive and functional at that time, by definition. The details of each model are specified below.

3.7.4.1 Mixed-effects model of mitochondrial dysfunction over time, impact, and treatment

A mixed-effects linear model was fit to test for significant differences in fractional mitochondrial dysfunction over time, impact condition, and treatment condition, as shown in Figure 3.3a. This mixed-effects model is detailed in Table 3.1 and was fit by the equation:

$$(fraction\ depolarized)^{\frac{1}{5}} = 1 + treated \times impacted + treated \times time + impacted \times time + treated \times impacted \times time + (1|animal)$$

Coefficient name	Coefficient estimate	Standard Error	t Statistic	DOF	p Value	95% CI Lower	95% CI Upper
(Intercept)	0.022	0.051	0.4	4632	6.7E-01	-0.078	0.122
'treated'	-0.061	0.077	-0.8	4632	4.2E-01	-0.212	0.089
'impacted'	0.635	0.023	27.9	4632	4.9E-158	0.591	0.680
'time_3'	0.016	0.021	0.8	4632	4.5E-01	-0.026	0.058
'time_4'	0.023	0.021	1.1	4632	2.8E-01	-0.019	0.065
'time_5'	0.103	0.021	4.8	4632	1.5E-06	0.061	0.144
'time_6'	0.129	0.021	6.1	4632	1.5E-09	0.087	0.171
'time_7'	0.141	0.021	6.6	4632	3.5E-11	0.100	0.183
'time_8'	0.226	0.021	10.6	4632	5.8E-26	0.184	0.267
'time_9'	0.500	0.021	23.5	4632	1.3E-115	0.459	0.542
'treated:impacted'	-0.457	0.034	-13.5	4632	1.1E-40	-0.524	-0.391
'treated:time_3'	-0.016	0.033	-0.5	4632	6.2E-01	-0.080	0.048
'treated:time_4'	-0.023	0.033	-0.7	4632	4.8E-01	-0.087	0.041
'treated:time_5'	-0.103	0.033	-3.2	4632	1.6E-03	-0.166	-0.039
'treated:time_6'	-0.129	0.033	-4.0	4632	7.6E-05	-0.193	-0.065
'treated:time_7'	-0.097	0.033	-3.0	4632	2.8E-03	-0.161	-0.034
'treated:time_8'	0.031	0.033	1.0	4632	3.4E-01	-0.033	0.095
'treated:time_9'	-0.022	0.033	-0.7	4632	4.9E-01	-0.086	0.042
'impacted:time_3'	0.046	0.032	1.4	4632	1.5E-01	-0.017	0.109
'impacted:time_4'	0.055	0.032	1.7	4632	8.9E-02	-0.008	0.118
'impacted:time_5'	0.010	0.032	0.3	4632	7.6E-01	-0.053	0.073
'impacted:time_6'	-0.025	0.032	-0.8	4632	4.3E-01	-0.088	0.038
'impacted:time_7'	-0.034	0.032	-1.1	4632	2.9E-01	-0.098	0.029
'impacted:time_8'	-0.089	0.032	-2.8	4632	5.6E-03	-0.152	-0.026
'impacted:time_9'	-0.324	0.032	-10.1	4632	1.5E-23	-0.387	-0.261
'treated:impacted:time_3'	0.089	0.048	1.9	4632	6.4E-02	-0.005	0.183
'treated:impacted:time_4'	0.110	0.048	2.3	4632	2.1E-02	0.017	0.204
'treated:impacted:time_5'	0.172	0.048	3.6	4632	3.2E-04	0.078	0.266
'treated:impacted:time_6'	0.217	0.048	4.5	4632	5.8E-06	0.123	0.311
'treated:impacted:time_7'	0.199	0.048	4.2	4632	3.2E-05	0.105	0.293
'treated:impacted:time_8'	0.150	0.048	3.1	4632	1.7E-03	0.056	0.244
'treated:impacted:time_9'	0.288	0.048	6.0	4632	1.9E-09	0.194	0.382

Table 3.1. Mixed-effects model of the fractional depolarization over time, impact condition, and treatment condition. Each row corresponds to one coefficient in the full model. This model was fit to the data shown in Figure 3.3a and used compute associated statistical comparisons.

3.7.4.2 Mixed-effects model of cell death over time, impact, and treatment

A mixed-effects linear model was fit to test for significant differences in fractional cell death over time, impact condition, and treatment condition, as shown in Figure 3.3b. This mixed-effects model is detailed in Table 3.2 and was fit by the equation:

$$\begin{aligned}(fraction\ dead)^{\frac{1}{10}} \\ = 1 + treated \times impacted + treated \times time\ + impacted \times time \\ + (1|animal)\end{aligned}$$

Coefficient name	Coefficient estimate	Standard Error	t Statistic	DOF	p Value	95% CI Lower	95% CI Upper
(Intercept)	0.079	0.048	1.7	4639	9.9E-02	-0.015	0.173
'treated'	-0.098	0.071	-1.4	4639	1.7E-01	-0.238	0.041
'impacted'	0.095	0.020	4.9	4639	1.2E-06	0.057	0.133
'time_3'	-0.008	0.021	-0.4	4639	7.1E-01	-0.049	0.033
'time_4'	0.001	0.021	0.0	4639	9.7E-01	-0.040	0.042
'time_5'	0.059	0.021	2.8	4639	5.1E-03	0.018	0.100
'time_6'	0.067	0.021	3.2	4639	1.4E-03	0.026	0.108
'time_7'	0.067	0.021	3.2	4639	1.5E-03	0.026	0.108
'time_8'	0.078	0.021	3.7	4639	1.9E-04	0.037	0.119
'time_9'	0.067	0.021	3.2	4639	1.5E-03	0.026	0.108
'treated:impacted'	-0.082	0.013	-6.1	4639	1.4E-09	-0.108	-0.055
'treated:time_3'	0.023	0.026	0.9	4639	3.9E-01	-0.029	0.074
'treated:time_4'	-0.001	0.026	0.0	4639	9.8E-01	-0.052	0.051
'treated:time_5'	-0.057	0.026	-2.2	4639	2.9E-02	-0.109	-0.006
'treated:time_6'	-0.070	0.026	-2.7	4639	7.9E-03	-0.121	-0.018
'treated:time_7'	-0.065	0.026	-2.5	4639	1.3E-02	-0.117	-0.014
'treated:time_8'	-0.023	0.026	-0.9	4639	3.9E-01	-0.074	0.029
'treated:time_9'	0.005	0.026	0.2	4639	8.5E-01	-0.047	0.056
'impacted:time_3'	0.121	0.026	4.6	4639	4.4E-06	0.069	0.172
'impacted:time_4'	0.225	0.026	8.6	4639	1.2E-17	0.174	0.277
'impacted:time_5'	0.238	0.026	9.1	4639	1.5E-19	0.187	0.290
'impacted:time_6'	0.288	0.026	11.0	4639	1.0E-27	0.237	0.339
'impacted:time_7'	0.295	0.026	11.2	4639	6.6E-29	0.243	0.346
'impacted:time_8'	0.325	0.026	12.4	4639	1.0E-34	0.274	0.376
'impacted:time_9'	0.334	0.026	12.7	4639	1.6E-36	0.283	0.385

Table 3.2. Mixed-effects model of the fractional cell death over time, impact condition, and treatment condition. Each row corresponds to one coefficient in the full model. This model was fit to the data shown in Figure 3.3b and used compute associated statistical comparisons.

3.7.4.3 Mixed-effects model of mitochondrial dysfunction over time, impact strain norm, and treatment

A mixed-effects linear model was fit to test for significant differences in fractional mitochondrial dysfunction over time, impact strain norm, and treatment condition, as shown in Figure 3.4. This model was fit using data from impacted samples only, because no-impact samples have zero strain, by definition, and thus the two variables are not independent. This mixed-effects model is detailed in Table 3.3 and was fit by the equation:

$$(fraction\ depolarized)^{\frac{1}{2}} = 1 + time + treated \times strain + (1|animal)$$

Coefficient name	**Coefficient estimate**	**Standard Error**	**t Statistic**	**DOF**	**p Value**	**95% CI Lower**	**95% CI Upper**
(Intercept)	0.036	0.048	0.7	5709	4.6E-01	-0.059	0.130
'treated'	-0.002	0.071	0.0	5709	9.8E-01	-0.142	0.138
'strain'	2.440	0.061	39.9	5709	8.0E-308	2.321	2.560
'time_3'	0.056	0.012	4.8	5709	1.3E-06	0.033	0.078
'time_4'	0.071	0.012	6.1	5709	9.1E-10	0.048	0.093
'time_5'	0.094	0.012	8.1	5709	4.5E-16	0.071	0.116
'time_6'	0.100	0.012	8.7	5709	5.1E-18	0.077	0.123
'time_7'	0.113	0.012	9.8	5709	1.9E-22	0.090	0.135
'time_8'	0.195	0.012	17.0	5709	5.4E-63	0.173	0.218
'time_9'	0.316	0.012	27.5	5709	6.3E-156	0.294	0.339
'treated:strain’	-2.371	0.090	-26.2	5709	2.8E-143	-2.548	-2.194

Table 3.3. Mixed-effects model of the fractional mitochondrial dysfunction over time, impact strain norm, and treatment condition. Each row corresponds to one coefficient in the full model. This model was fit to the data shown in Figure 3.4 and used compute associated statistical comparisons.

CHAPTER 4. LOCAL AND GLOBAL MEASUREMENTS SHOW THAT DAMAGE INITIATION IN ARTICULAR CARTILAGE IS INHIBITED BY THE SURFACE LAYER AND HAS SIGNIFICANT RATE DEPENDENCE

Bartell, L. R., Xu, M. C., Bonassar, L. J., Cohen, I. *Journal of Biomechanics* **72,** 63-70 (2018).

4.1 Abstract

Cracks in articular cartilage are a common sign of joint damage, but failure properties of cartilage are poorly understood, especially for damage initiation. Cartilage failure may be further complicated by rate-dependent and depth-dependent properties, including the compliant surface layer. Existing blunt impact methods do not resolve local cartilage inhomogeneities and traditional fracture mechanics tests induce crack blunting and may violate underlying assumptions of linear elasticity. To address this knowledge gap, we developed and applied a method to indent cartilage explants with a sharp blade and initiate damage across a range of loading rates (strain rates 0.5%/s to 500%/s), while recording local sample deformation and strain energy fields using confocal elastography. To investigate the importance of cartilage's compliant surface, we repeated the experiment for samples with the surface removed. Bulk data suggest a critical force at which the tissue cuts, but local strains reveals that the deformation the sample can sustain before reaching this force is significantly higher in the surface layer. Bulk and local results also showed significant rate dependence, such that samples were easier to cut at faster speeds. This result highlights the importance of rate for understanding cracks in cartilage and parallels recent studies of rate-dependent failure in hydrogels. Notably, local sample deformation fields were well fit by classical Hookean elasticity. Overall, this study illustrates how local and global measurements surrounding

the initiation of damage in articular cartilage can be combined to reveal the importance of cartilage's zonal structure in protecting against failure across physiologically relevant loading rates.

4.2 Introduction

Cracks in articular cartilage are a common sign of joint damage. In clinical settings, fissures are often observed during arthroscopic inspection of an injured joint[115,116]. Such injuries predispose patients to chronic joint damage and disease, including osteoarthritis[3]. In orthopedics, clinicians and researchers acknowledge the importance of cracks by including them in various arthroscopy and histopathology grading schemes[117,118]. Basic science and engineering studies have also associated cartilage cracks with increased cell death and matrix degradation[2,119], suggesting they can disrupt the homeostasis that is essential for joint health. As such, cracks in cartilage have the potential to be an important early marker of cartilage damage and disease. However, beyond these basic observations, cartilage cracks are poorly understood and many questions must be answered before cracks can guide clinical decision-making.

One complication for studying cracks in cartilage is that cartilage is highly anisotropic and heterogeneous, with mechanical properties and composition that vary with depth. The superficial 100-300 µm of tissue, known as the surface layer, has lower compressive and shear moduli than the bulk[49,102], which may be explained by variations in composition[37]. Additionally, the collagen alignment varies with depth, where fibers near the surface are predominantly parallel to that surface with an additional in-plane alignment known as the split-line pattern[22–24]. Recent results have further demonstrated that the surface layer may serve a mechanically protective role[26,84].

Beyond variations in composition and alignment, cartilage has a complex rate-dependence from both viscoelastic and poroelastic effects[120]. All of these factors may influence cartilage fracture and failure but are difficult to disentangle without studying cartilage at spatial resolutions of around ten microns.

Experimentally, cartilage cracks are generally studied in two contexts: blunt overload or traditional fracture mechanics geometries, such as the notch test. In overload experiments, such as a drop-tower test, a blunt object rapidly and forcefully impacts cartilage[6,40,40,42,43,104]. When this loading is faster than the poroelastic time scale, fluid is trapped and pressurizes, thus stressing the surrounding solid matrix, which ultimately ruptures[121]. This loading is analogous to physiologic injuries, but the geometry of the sample and loading both influence fluid pressurization and so the material properties are difficult to disentangle. Moreover, the exact location of crack initiation is unknown prior to loading, making it experimentally difficult to study local material behavior. In contrast, traditional fracture mechanics experiments apply standardized sample and loading geometries to articular cartilage that are designed to concentrate stress at a particular point, leading to material failure[122–125]. By linking a specific geometry to linear elasticity, such data can be used to calculate material properties, such as toughness, which describes the ability to absorb energy without cracking. In soft tissues, however, finite strains may violate the assumptions of linear elasticity and it is unclear to what degree this affects the understanding of cartilage failure. Studies applying the well-known notch test to cartilage show the tissue failing by crack-blunting and plastic yielding rather than traditional brittle crack propagation, indicating that tissue microstructure inhibits the stress concentration necessary to propagate brittle-like cracks[126,127]. Additionally, such methods study steady-state crack growth, rather than damage initiation, though the latter may be equally important physiologically. Thus, neither blunt overload nor traditional fracture tests are adequate to fully understand cracks in articular cartilage, especially damage initiation.

To address this knowledge gap, this study aimed to develop an indentation-based method to study damage initiation in articular cartilage. By indenting samples with a sharp blade, we created a crack at a known location, in a well-defined geometry, and with more stress-concentration than notch tests [128]. Moreover, because the crack location was known, we could utilize recently developed confocal elastography techniques to study both global and local material behavior and investigate the importance of material inhomogeneity and finite strains when interpreting damage initiation in cartilage. We further investigated how rate modulates the observed damage initiation by indenting over a wide range of loading rates. Combined, this method simultaneously observed the local, global and time-dependent processes that are potentially important to understanding damage initiation in articular cartilage.

4.3 Methods

4.3.1 Sample preparation

Chondral explants were harvested from condyles of 13 neonatal calves (sex unknown; Gold Medal Packing, Oriskany, NY) (Figure 4.1A). Explants were immersed in PBS and stored at 4°C for up to 48 h. For testing, explants were trimmed to 3 mm deep and bisected perpendicular or parallel to the known split-line direction[129], creating 125 hemi-cylindrical samples. In some samples, a sledge microtome was used to remove 500 μm from the articular surface, creating a surface-removed group. Information about each sample was recorded, including source animal, condyle (medial or lateral), orientation (parallel or perpendicular to split-line), time between dissection and testing, and surface condition (intact or removed).

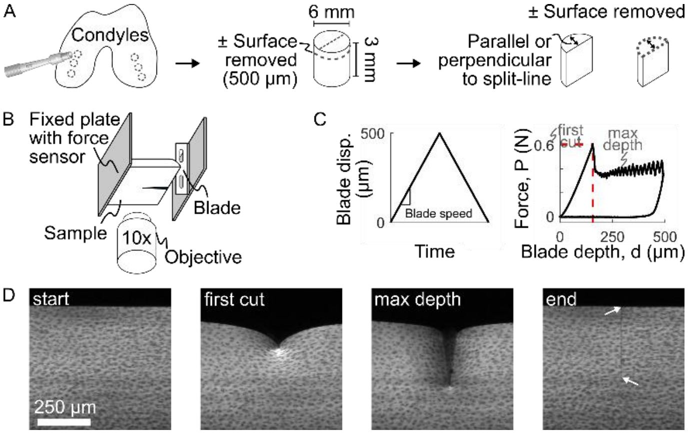

Figure 4.1. Outline of experimental methods. (A) Cylindrical plugs were harvested from medial and lateral condyles, trimmed to 3 mm deep, with the surface either intact or removed, and then bisected to create hemi-cylindrical samples. (B) Samples were mounted to the fixed plate of the test frame, with the cartilage surface facing the blade. The test frame was mounted on a confocal microscope to image local sample deformation. (C) The blade was driven into the sample at a fixed speed to a maximum displacement of 500 μm while the bulk force response was recorded at the fixed plate using a force sensor. A characteristic force-depth curve is shown with the point of first-cut marked by the dashed red lines. (D) Example confocal images taken throughout the experiment. At the end, after the blade has retracted, arrows mark the extent of the remaining crack. Note there is no residual deformation, indicating elastic deformation, other than the newly-created crack surface.

4.3.2 Indentation device

To test cartilage failure properties, a razor blade (#27-251, Razor Blade Company, Van Nuys, CA; ~150 nm tip diameter, §4.7.1) was mounted to the piezoelectric-driven plate of a Tissue Deformation Imaging Stage (TDIS; Harrick Scientific, Ithaca, NY) and used to indent cartilage, thus creating cracks in a known location (Figure 4.1B,C). Samples were glued to the fixed plate of the TDIS, as described previously[49]. During indentation, force was measured using a 2 kg (19.6 N) load cell (S300, Strain Measurement Devices, Wallingford, CT) and blade displacement was recorded from the piezoelectric monitor. The blade was driven to 500 µm displacement and retracted at fixed speeds of 2.5 to 1000 µm/s. Each sample was immersed in PBS throughout testing and indented only once with a fresh blade.

The TDIS was mounted onto an inverted confocal microscope (LSM 5 LIVE, Carl Zeiss Inc., Oberkochen, Germany), to observe local sample deformation. For imaging contrast, samples were stained for 50 minutes in 14 µM 5-DTAF[49]. Videos of deformation during indentation were recorded at 15 to 60 frames per second, depending on blade speed, with a 512 pixel (666 µm) field of view (Figure 4.1D).

4.3.3 Data analysis

For each experiment, force (F) verses blade depth (d) plots were characterized. Force was smoothed using a moving-average filter with a window size of 1 µm blade displacement (scaled in time based on the blade speed). The blade depth was calculated as the blade displacement minus the slight displacement of back plate resulting from the strain-based load cell. The critical force,

F_C, and depth, d_C, at first-cut were extracted, and the data were integrated up to this critical point to extract strain energy, W_C. For these three responses (critical force, depth, and energy), mixed-effects linear regression models were implemented to test which parameters significantly affected each response (§4.7.2).

Confocal videos were processed to extract local deformation and energy fields. Videos were analyzed from zero blade depth to just beyond the point of first cut using Ncorr (2D image correlation; widow size 19.7 µm, grid spacing 3.9 µm, smoothing radius 27.5 um)[105]. Images were generally well tracked, except the area closest to the blade tip. When the first cut in the bulk response did not agree with that observed in the confocal video, likely due to misalignment, samples were excluded from local deformation analysis.

Deformation fields were used to compute local strain energy density. Strain energy was calculated by assuming a 2D neo-Hookean constitutive model with depth-dependent Lamé parameters taken from the literature[102,129]. Local deformations were compared to the 2D functional form predicted by contact mechanics. According to Johnson[128], line loading of a Hookean elastic half-space yields the radial displacement field:

$$u_r(r,\theta) = -\frac{(1-\upsilon^2)}{\pi E} 2P \cos\theta \ln\frac{r}{r_0} - \frac{(1-2\upsilon)(1+\upsilon)}{\pi E} P\theta \sin\theta \tag{4.1}$$

where μ_r is the radial displacement, r is the radial distance from the applied load, θ is the circumferential direction ($\theta = 0$ parallel to the applied load), ν and E are the Poisson's ratio and Young's modulus, P is the applied force per length, and r_0 is a scaling constant. Thus, 2D displacement data for each sample were fit to:

$$u_r(r,\theta) = \cos\theta\,(-\beta_1 \ln r + \beta_2) - \beta_3\theta \sin\theta \tag{4.2}$$

with $\beta_1 = \frac{(1-\upsilon^2)}{\pi E}2P$, $\beta_2 = \beta_1 \ln r_0 + \alpha$, and $\beta_3 = \frac{(1-2\upsilon)(1+\upsilon)}{\pi E}P$,

using a nonlinear least-squares approach with fitting coefficients β_i. Note that β_2 incorporates both the scaling term r_0 and any overall sample displacement resulting back plate displacement, α.

4.4 Results

Bulk indentation force-depth data showed similar behavior across all samples, including a smooth rise up to the point of first cut, followed by a dramatic drop and then a sawtooth-like pattern as the blade continued to cut (Figure 4.2A). The critical force, depth, and energy at first-cut were extracted and fit to linear mixed-effects models (Figure 4.2B-D). All three outcomes depended significantly on indentation rate ($p = 2.6\times10^{-5}$, 5.5×10^{-21}, and 6.1×10^{-16} for critical force, depth, and energy, respectively). Moreover, the critical depth and energy were significantly lower for surface-removed samples ($p = 1.2\times10^{-29}$ and 1.7×10^{-4}, respectively). Notably, no other terms were significant in the models.

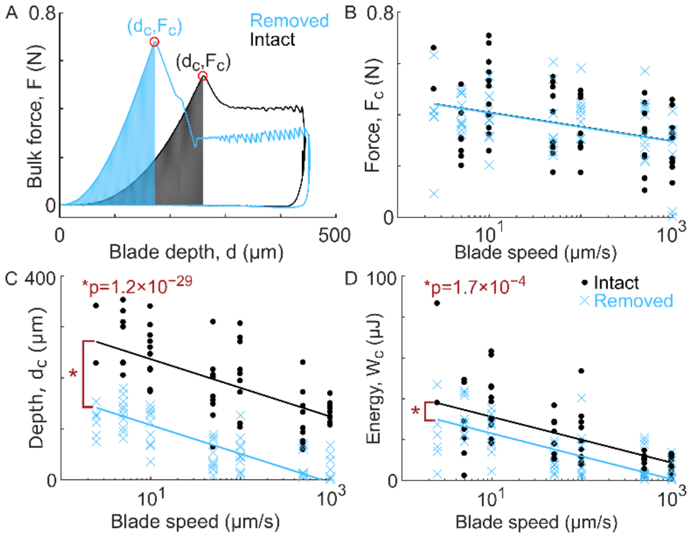

Figure 4.2. (A) Characteristic force vs. blade depth curves for one surface-intact and one surface-removed sample. Both samples were taken from the 10 μm/s blade speed group. For all samples, the force and depth at first cut (d_C and F_C, respectively) were extracted and the integration of force verses depth up to that point, a measure of strain energy (W_C), was computed. (B-D) The force, depth, and energy at first cut for all experiments (circles or crosses), shown with the corresponding reduced linear model fits (solid lines), for surface-intact (black) and surface-removed (blue) samples. For all three measures, the response was significantly dependent on blade speed (p-values: 2.6×10^{-5}, 5.5×10^{-21}, and 6.1×10^{-16}, respectively). Additionally, surface-removed samples had a lower critical cut depth and energy, as compared to surface-intact (p-values: 1.2×10^{-29} and 1.7×10^{-4}, respectively). See §4.7.2 for full statistical models.

Normalizing each bulk force curve by the critical force and depth collapsed the data to reveal overall trends that varied with loading rate (Figure 4.3A). At slower blade speeds, surface-intact and -removed samples showed similar trends, including a slight “J”-shaped response. At higher blade speeds, the surface-removed samples showed a dramatic change in concavity, with a steep initial rise in the force response. For each blade speed, the difference between surface-intact and -removed trends was characterized by the root-mean-square (RMS) deviation between each pair of normalized force-depth curves (Figure 4.3B). This RMS deviation confirmed that intact and removed samples became increasingly distinct at faster indentation.

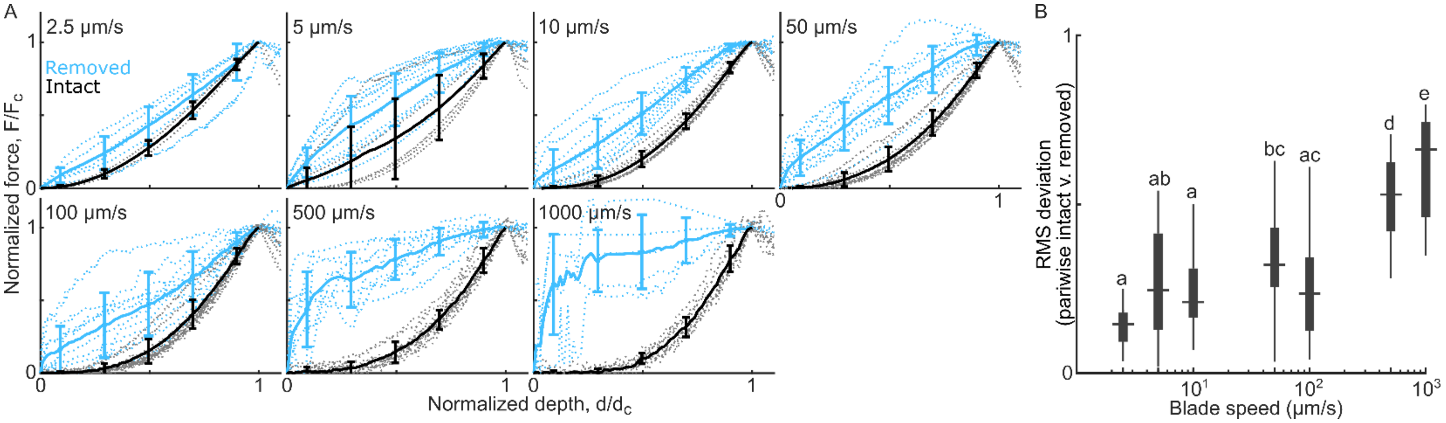

Figure 4.3. (A) Force verses blade depth curves, up to the point of first-cut, normalized by the cut force and cut depth, and grouped by blade speed. Individual samples are shown in dotted lines and group averages +/- standard deviation are shown in solid lines. Surface-intact samples (gray curves) show characteristic “J”-shaped response. In the 2.5 µm/s group, surface-removed samples follow a similar trend. However, at higher speeds the surface-intact and -removed groups become increasingly distinct and, instead of a toe-region, surface-removed samples show a sharp initial rise. (B) A Tukey box plot of the RMS deviation between each pair of normalized force curves, as a function of blade speed. Groups that share a letter are not significantly different, confirming that the intact and removed samples become increasingly distinct (higher deviation) at faster speeds.

In addition to the bulk response, confocal videos were analyzed to extract local deformation fields and calculate strain energy density. Samples showed high strain and strain energy near the tip, though the shape and magnitude varied between groups. Figure 4.4 compares characteristic samples from the surface-intact and -removed groups at similar bulk force and again at similar blade depths. At first-cut, the strain was higher in magnitude and spread over a larger region of the surface-intact sample. The strain energy density fields looked more similar between the groups. Comparing the samples at matched-depth instead, the surface intact sample still showed more lateral spread of strain across the compliant articular surface (arrows), while the strain energy density field was much lower in magnitude.

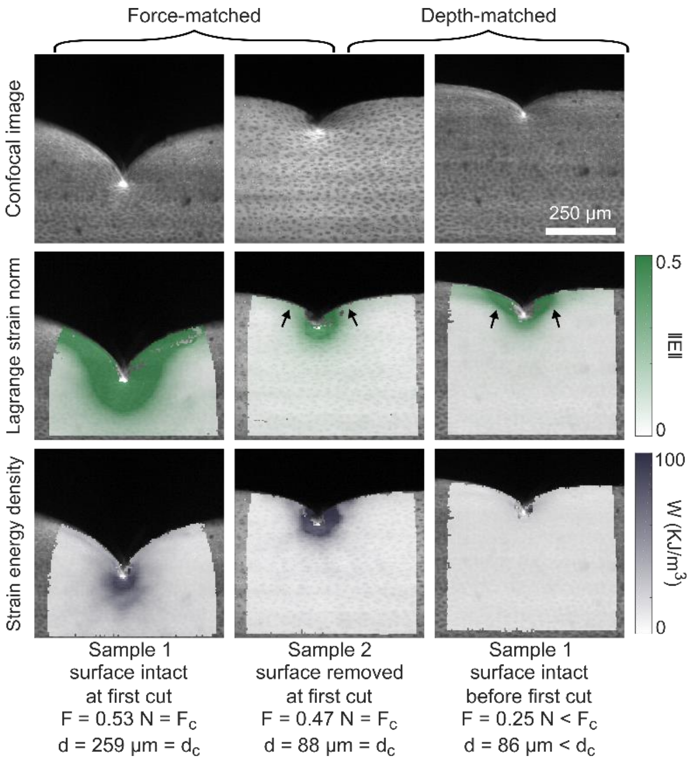

Figure 4.4. Local deformation analysis for strain and strain energy density. Columns 1-2 compare one surface-removed and one surface-intact sample at first cut, i.e. with similar bulk force. Alternatively, columns 2-3 compare the same two samples, but at similar blade depths (i.e. prior to the first cut for the surface-intact sample). Row 1 shows the raw confocal images, row 2 shows the resulting Lagarange strain norm, and row 3 shows the corresponding strain energy density. Note that both strain and strain energy are in deformed coordinates. In the force-controlled comparison, strain fields are distinct between surface-intact and -removed, but the strain energy fields are more similar. The opposite is true (similar strain but distinct strain energy) for the depth-controlled comparison. Arrows highlight differences in how the strain field spreads across the surface layer.

To characterize overall trends, strain energy density fields were grouped by surface condition and indentation rate and averaged (Figure 4.5A). The 2.5 and 1000 μm/s groups only had one sample each and thus were excluded. Two trends were apparent from these plots. First, the magnitude of the strain energy decreased with increasing blade speed, in agreement with the bulk results (Figure 4.2D). Second, strain energy fields in surface-intact samples were more oblong, extending farther both along the surface and deeper into the tissue, while surface-removed fields were more radially symmetric (§4.7.3). Figure 4.5B shows the average change in strain energy density before and after first cut, when the blade had moved 20 µm further. These ΔW fields highlight where strain energy was lost to create the resulting initial cut ($\Delta W<0$), and where additional strain energy was gained as the blade advanced ($\Delta W>0$). These ΔW fields decreased in spatial extent with increasing rate.

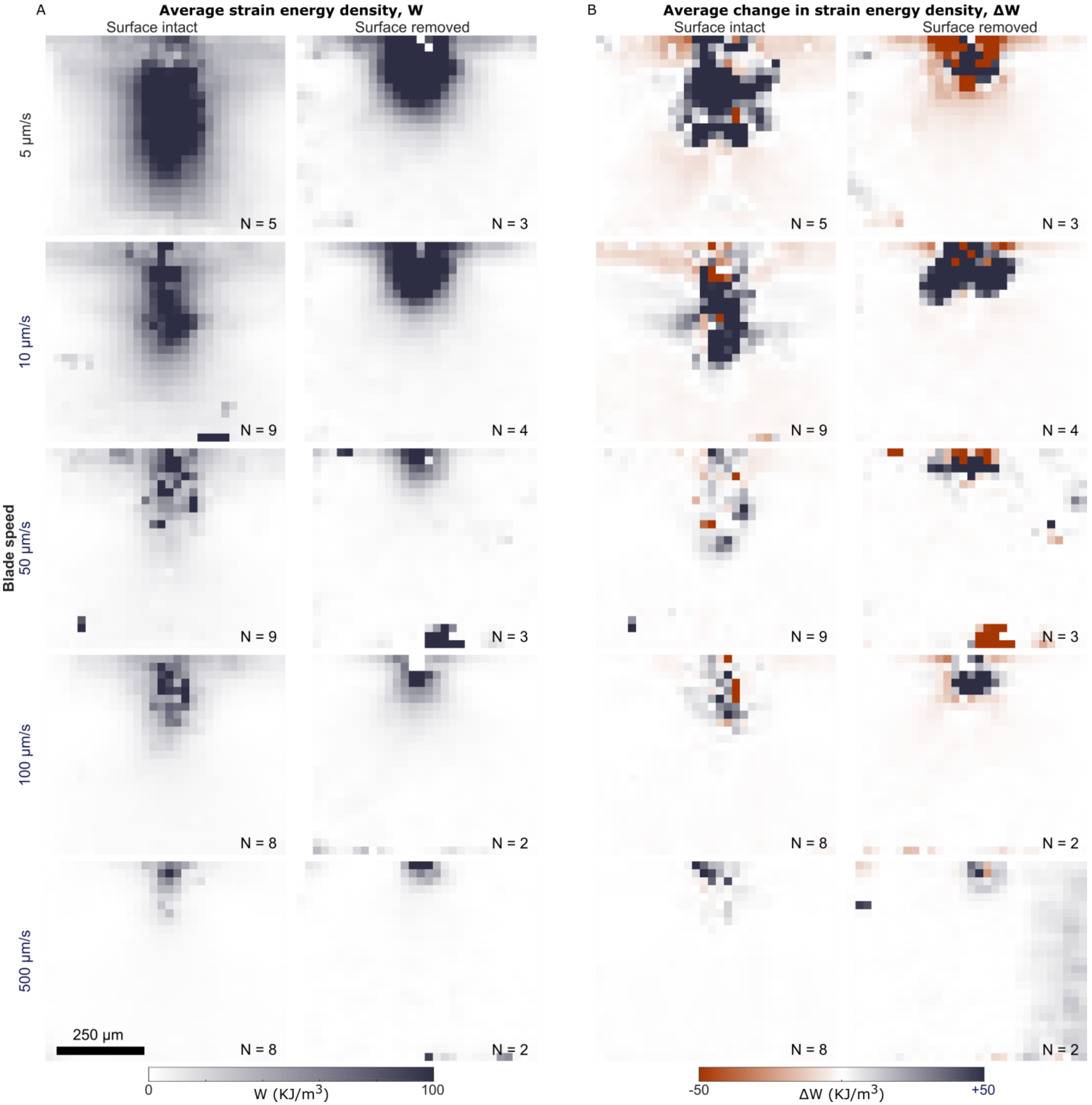
A
Average strain energy density, W
Surface intact
Surface removed
B
Average change in strain energy density, ΔW
Surface intact
Surface removed
Blade speed
5 µm/s
10 µm/s
50 µm/s
100 µm/s
500 µm/s
N = 5
N = 3
N = 9
N = 4
N = 9
N = 3
N = 8
N = 2
N = 8
N = 2
250 µm
0
W (KJ/m^3)
100
-50
ΔW (KJ/m^3)
+50

Figure 4.5. (A) Average strain energy density fields at first cut, grouped by surface condition (columns) and blade speed (rows), in undeformed coordinates, where the top-center of each frame corresponds to the point of blade indentation. In general, the surface-intact strain energy field is more oblong, extending deeper into the sample and laterally along the surface, while the surface-intact strain energy field is more radially symmetric about the point of indentation. In both surface-intact and surface-removed groups, the strain energy density decreases as blade speed increases, in agreement with the bulk results. (B) Similar plots of the average change in strain energy density from just before the point of first cut to a few frames after, when the blade has moved 20 μm further. Note that some areas of the field have decreased strain energy (i.e. negative ΔW) while others have increased (i.e. positive ΔW). As in the strain energy fields shown in (A), the overall extent of ΔW fields also decreases with increased blade speed. Numbers (N) at the bottom of each frame indicate the number of samples averaged to produce the given field. The scale bar applies to all frames.

Displacement fields were fit to the form predicted by contact mechanics. Figure 4.6 shows cuts of the raw data and associated 2D fits to Equation 4.2 for constant θ and varying r (A,D) and for constant r and varying θ (B,E). For all samples, β_i coefficients fell in the in the expected range, given values of ν and E taken from the literature and F_C taken from this study (§4.7.4). Despite assumptions of small-strain Hookean elasticity and infinite boundaries, these fits recapitulated the overall trends with coefficients of determination greater than 0.9 in all cases (R^2, Figure 4.6C,F). In fact, the surface-intact samples tended to have lower R^2, since the data deviated more from the fit at smaller values of r and was more sharply peaked in θ. This observation is not surprising, considering that the model assumes homogeneous material properties and the surface-intact samples have a mechanically-distinct surface layer.

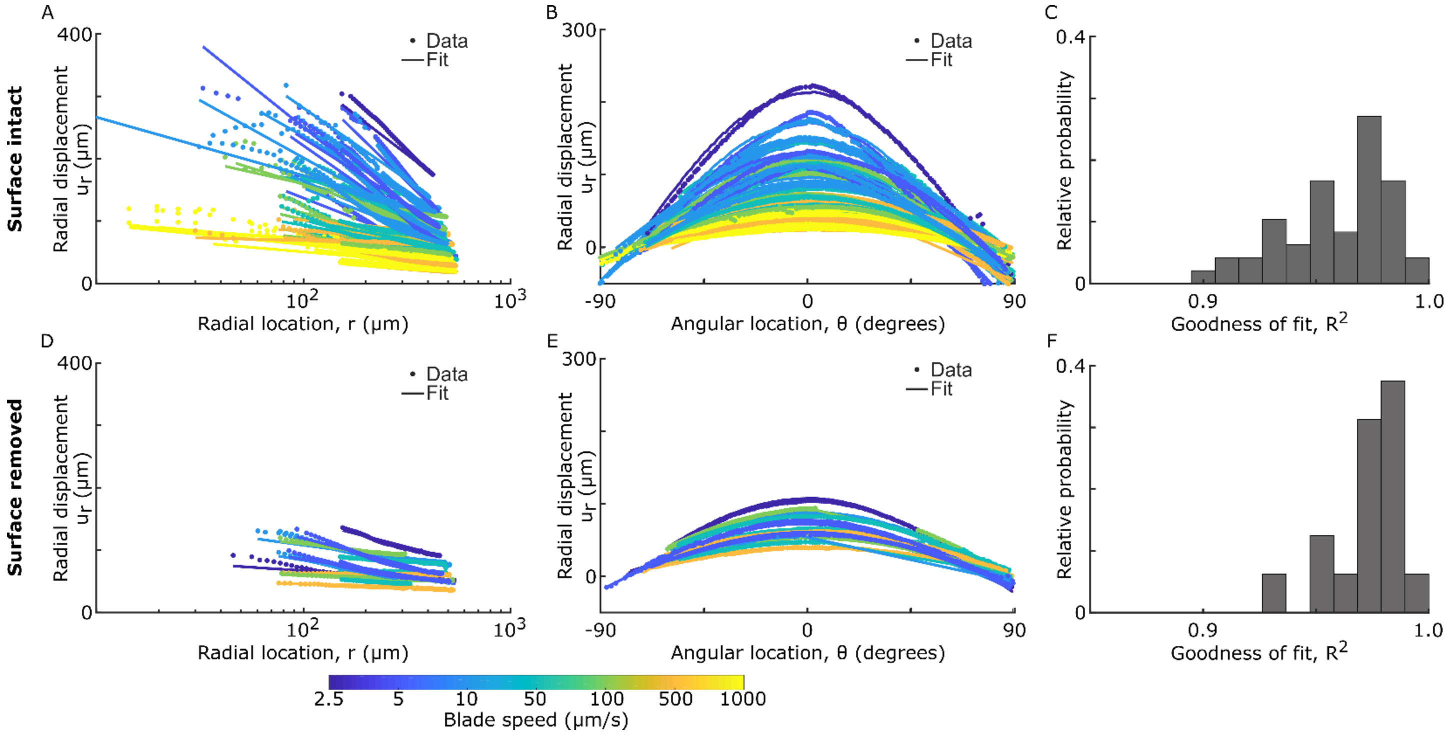

Figure 4.6. Cuts of the 2D displacement data and associated 2D fits to the functional form predicted by contact mechanics (Equation 4.2). Data and fits are shown for (A-C) surface-intact samples and (D-F) surface-removed samples, with cuts taken (A,D) at θ = 0° and (B,E) at r = 300 μm. Color reflects blade speed. (C,F) Associated histograms of the goodness of fit (coefficient of determination) for each fit. In general, this equation fits the data well (R^2>0.9), though there are larger deviations at small values of r and, for surface-intact samples, the data's trend with θ is more sharply peaked. See §4.7.4 for data and fits normalized by the fitting parameters.

4.5 Discussion

Our blade indentation experiments with confocal elastography revealed strong rate dependence in both bulk and local results, such that samples were easier to cut at faster speeds. As rate increased, the first-cut occurred at lower force, lower blade depth, lower energy, more localized strain field, and smaller radial displacement (Figure 4.2, Figure 4.5, Figure 4.6). Moreover, in surface-removed samples, normalized bulk force trends with depth switched from a strain-stiffening to a strain-weakening behavior with increasing indentation speed (Figure 4.3). This rate dependence may be explained by the depth-varying poroelastic and viscoelastic time scales inherent to articular cartilage. Here, the relevant characteristic length scale determining the rate of fluid flow in the tissue may vary from the radius of the blade tip (≈150 nm) to the decay length of the strain field (≈500 µm). These length scales result in characteristic poroelastic time scales of 0.1 ms to 40 s, spanning the range from faster to slower than the indentation rate. Thus, at slower rates, fluid pressurization and flow are unlikely to be a dominant factor but may come into play at faster rates. The viscoelasticity of cartilage may introduce another time scale. Using data from Hayes and Bodine[19], the viscosity of the solid matrix at 20 Hz is about 23 kPa·s, which, dividing by the storage modulus, gives a time scale of about 15 ms. Thus, viscoelastic dissipation in the solid matrix is less likely to influence the results here, except at the faster indentation rates. Overall, the rate dependence studied here is physiologically relevant, ranging from nearly static (≈0.5%/s) to injurious (≈500%/s) rates[121,130]

In addition to this rate-dependence, both bulk and local responses varied between surface-intact and surface-removed sample groups. While the groups had similar critical bulk force, surface-removed samples had significantly lower critical depth and energy (Figure 4.2). Locally, the strain and strain energy fields spread across the compliant surface layer, but strain was more localized near the tip in surface-removed samples (Figure 4.4, Figure 4.5). Combined, these results suggest a critical force at which the tissue cuts, but the deformation the sample can sustain before reaching this force is significantly higher for the surface layer. In vivo, this behavior would allow the surface to better conform to local defects in the loading geometry before cracking. Combined with the fact that the surface is more dissipative than the bulk, these results reinforce the idea that the surface tissue may serve a mechanically protective role in the joint[26,84].

Separately, it is interesting to note that, other than indentation rate and surface condition, no variables significantly affected any of the responses measured in this study. The fact that neither orientation, nor its interaction with surface condition was significant implies that, while the compliant surface is mechanically important, the orientation of the thin zone of highly aligned fibers at the articular surface did not have a large effect on any of the responses studied here. While these results are surprising, they may change with tissue maturity as the collagen alignment develops further[131].

The primary focus of this study was connecting the local and global trends up to and at first-cut, i.e. for damage initiation. In the literature, the propagation of existing cracks is also an important topic that, like damage initiation, is understudied in the context of articular cartilage. The existing studies often computed toughness during crack propagation as characterized by the strain energy release rate (energy released per crack area), yielding values ranging from 140 J/m^2 to over 1000 J/m^2 [123,125,127,132]. To compare our results to these studies, we extracted a similar estimate of toughness from the bulk force-displacement data which averaged to 32.3 J/m^2 for surface-intact samples and 68.0 J/m^2 for surface-removed samples (§4.7.5). While this measure excludes the superficial-most tissue (≈50 μm) and is lower than the other literature values, it suggests that toughness increases with depth into the tissue. It is especially interesting to note that our measure of toughness is closest to that measured by Chin-Purcell and Lewis for their cartilage samples that displayed the most brittle-like response[123], similar to the cracking observed in the present study. This comparison highlights that, although the loading geometry used here does not mimic that experienced physiologically, it carries some advantages of traditional fracture mechanics approaches, including localized stress concentration in a standardized geometry that encourages brittle-like fracture modes over a wide-range of physiologically relevant loading rates.

In the broader field of material damage and failure, the effects of both inhomogeneous material properties and time-dependent processes are active areas of research, especially for soft materials, such as hydrogels. In layered systems, cracks have been observed to propagate toward and then along interfaces[133,134], which is not unlike the crack deflection often observed in articular cartilage[40,135,136], and may be related to the difference between surface-intact and -removed groups observed here. In hydrogels, both viscoelasticity and poroelasticity are known to modify the material failure and damage in complex ways[137,138]. Indentation and compression based experiments, similar to the method used here, have recently shown promise for studying this time-dependent behavior in hydrogels[138]. Another interesting parallel is with recently-developed double-network hydrogels which, with a combination of elastic and ductile (i.e. dissipative) networks, can have extremely high toughness[139,140]. Cartilage, one of the toughest, soft bio-materials, may also be considered a double-network (elastic collagen, dissipative proteoglycan networks) and so this interpretation may be relevant for cartilage failure. Beyond hydrogels, a similar “stick-slip” sawtooth region was observed when performing displacement-controlled blade indentation on rubbers[141]. This comparison suggests that, after first cut, friction may also play a role in our study. In the future, it would be interesting to explore the above parallels in more detail, since each has important implications for both the likelihood of native cartilage failing during normal or super-physiological use, as well as designing engineered tissues that can withstand the complex, dynamic loading environment in a joint.

Though useful for resolving the importance of rate and local material behavior in initiating cartilage damage, this study is not without limitations. In particular, neonatal bovine articular cartilage explants were used. Neonatal tissue is known to have an under-developed collagen alignment[22], and so the response of mature tissue may be further modulated by its stronger collagen alignment[131]. The tissue toughness may also increase as collagen density and cross-linking increase with maturity[142]. Nonetheless, the shear properties of immature and mature tissues are similar[49] and immature tissue provides a framework for studying injury[66,67]. Another limitation is the use of a neo-Hookean constitutive model to calculate strain energy fields. This model does not perfectly capture cartilage’s response[143], and parameters were taken from the literature instead of sample-specific measurements. Nonetheless, the neo-Hookean model performs adequately when compared to others[143], and is designed for situations with large deformations, such as those observed in this study[144].

The combination of bulk and local measurements surrounding cartilage damage and cracking demonstrated in this study provides a fruitful ground for bridging the gap between traditional fracture mechanics, local damage theories, and clinically-relevant articular cartilage failure. In future work, it would be interesting to develop this method further, building theoretical underpinnings to extracting relevant material damage and failure properties as a function of location in the tissue. Also, as confirmed in this study, loading rate is central to understanding articular cartilage both *ex vivo* and *in vivo*, including its failure. To that end, future work with this method can address this rate dependence in more detail, including its link to cutting-edge research regarding the effects of poroelasticity, viscoelasticity, and secondary-networks on the strength and failure of hydrogel-like materials. Overall, this study illustrates how combining local and global measurements surrounding the initiation of damage in articular cartilage can be used to reveal the importance of cartilage's known layered structure in protecting against failure across physiologically relevant loading rates.

4.6 Acknowledgements

This study was supported by the National Science Foundation (NSF) under award number CMMI 1536463. L.R.B. was supported by the National Institutes of Health, under award number 1F31-AR069977. This work made use of the Cornell Center for Materials Research Shared Facilities, which are supported through the NSF MRSEC program (DMR-1719875). The authors would also like thank Lynn Johnson at the Cornell Statistical Consulting unit, Prof. C. Y. Hui, and members of the Cohen and Bonassar lab for useful discussions.

4.7 Supplemental information

4.7.1 Blade geometry

The sharpness of razor blades used in this study (#27-251, Razor Blade Company, Van Nuys, CA) was characterized by imaging the tip of a fresh, untouched blade using a SEM (Zeiss LEO 1550 FESEM, Oberkochen, Germany). As shown in Figure 4.7, the radius at the tip of these uncoated blades is approximately 75 nm and the apex angle at the tip is 29° ± 1°, as measured using ImageJ.

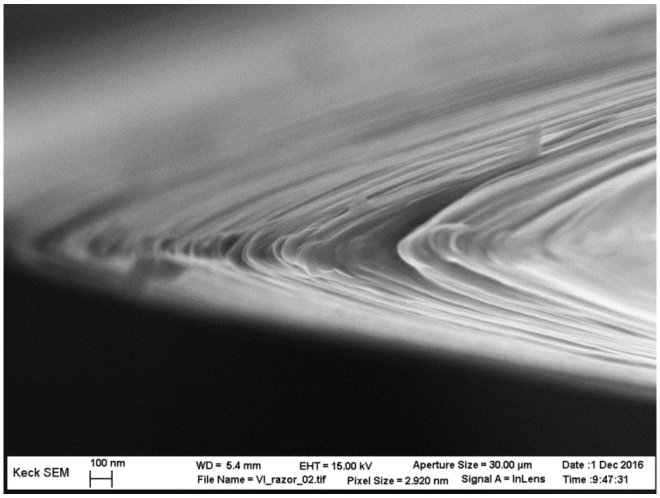

Figure 4.7. A SEM image showing the tip of a fresh razor blade. The radius of the tip is approximately 75 nm.

4.7.2 Mixed-effect linear models of bulk responses

Critical bulk force, blade depth and integrated energy at the point of first fracture were fit to mixed-effects linear regression models in order to test for significant effects. Each of these three responses was fit to a linear model which included all individual and interaction terms for the available variables: sample orientation (parallel or perpendicular to the split-line), surface condition (intact or removed), storage time between dissection and testing, source condyle (medial or lateral), and the natural log of the blade speed. A random effect was added to account for samples that originated from different animals. These models were implemented in MATLAB (The MathWorks Inc, Natick, MA) using the `fitlme` function. Each full model was reduced by iteratively removing insignificant highest-order terms ($p > 0.01$) and fitting again, using the Satterthwaite approximation for computing degrees of freedom. The residuals of each model were also checked for normality and homogeneity.

Response = A + B × ln(blade speed)	**Parameter A**			**Parameter B**		**Goodness of fit**
	Parameter value		p-value	Parameter value	p-value	Adjusted R^2
	Intact	Removed	Intact vs. Removed	Intact or Removed	Value vs. zero	
Cut force (N)	0.484	0.462	0.96	−0.0242	2.6×10^{-5}	0.12
Cut depth (μm)	293	162	1.2×10^{-29}	−24.5	5.5×10^{-21}	0.72
Cut energy (μJ)	42.3	34.2	1.7×10^{-4}	−4.87	6.1×10^{-16}	0.42

Table 4.1. Coefficients, significance values, and goodness of fit values for the reduced mixed-effects linear models of critical bulk force, depth, and energy at first cut, and the toughness (throughout cutting) as shown in Figure 4.2B-D. In all cases, the full model was reduced by removing insignificant higher-order fixed effects ($p > 0.01$), resulting in the final two-parameter model shown here.

4.7.3 Strain energy density spatial extent

The spatial extent of individual strain energy fields in undeformed coordinates was characterized by taking the lateral- and depth-variance of data points above a strain-energy threshold of 20 KJ/m^3. Each variance was then fit to a reduced, fixed-effects linear model to test for significant effects. Each linear model included all individual and interaction terms for the available variables: sample orientation (parallel or perpendicular to the split-line), surface condition (intact or removed), storage time between dissection and testing, source condyle (medial or lateral), and the natural log of the blade speed. These models were implemented in MATLAB using the `fitlm` function. Each full model was reduced by iteratively removing insignificant highest-order terms ($p > 0.01$) and fitting again, using the Satterthwaite approximation for computing degrees of freedom. The residuals of each model were also checked for normality and homogeneity.

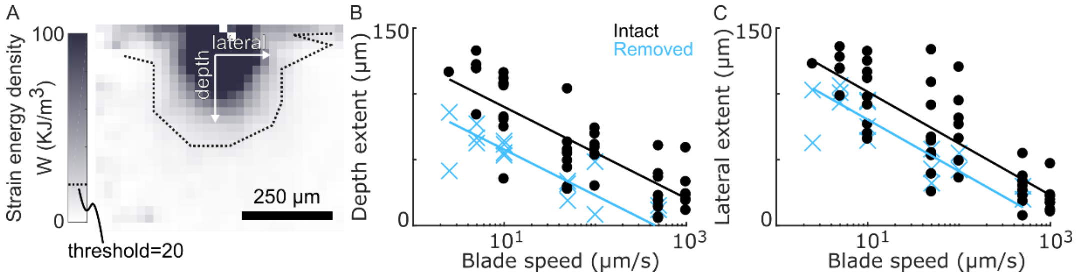

Figure 4.8. Analysis of the spatial extent of the strain energy density field in the lateral and depth dimensions. (A) Example strain energy density field showing the points above the threshold value of 20 KJ/m^3. Points above this threshold were analyzed to calculate the variance in the (B) depth and (C) lateral directions for surface-intact samples (black circles) and surface-removed samples (blue circles). This data was fit to a fixed-effects model based on the log of the blade speed and the surface condition and these fits are shown as solid lines. The fits are further detailed in Table 4.2.

Response = A + B × ln(blade speed)	**Parameter A**			**Parameter B**		**Goodness of fit**
	Parameter value		p-value	Parameter value	p-value	Adjusted R^2
	Intact	Removed	Intact vs. Removed	Intact or Removed	Value vs. zero	
Depth extent (μm)	125	92.4	3.3 E -7	-15.1	3.0 E -17	0.69
Lateral extent (μm)	141	120	1.4 E -3	-17.0	1.7 E -17	0.68

Table 4.2. Coefficients, significance values, and goodness of fit values for the linear fixed-effects models of the lateral and depth extent of the strain energy fields, as shown in Figure 4.8B-C.

4.7.4 Radial displacement fields fits

In order to compare observed sample deformation with that predicted by contact mechanics, local 2D displacement data was fit to the 2D functional form predicted by contact mechanics[128]. Although this theory assumes infinitely-sharp indentation of a Hookean elastic half space under small strain conditions, Equation 4.2 fit the data reasonably well, as shown in Figure 4.6. To highlight the logarithmic scaling, data and fits were scaled by the fitting parameters, β_i, and these 1D cuts of the normalized 2D data and fits are shown on a linear-log plot in Figure 4.9.

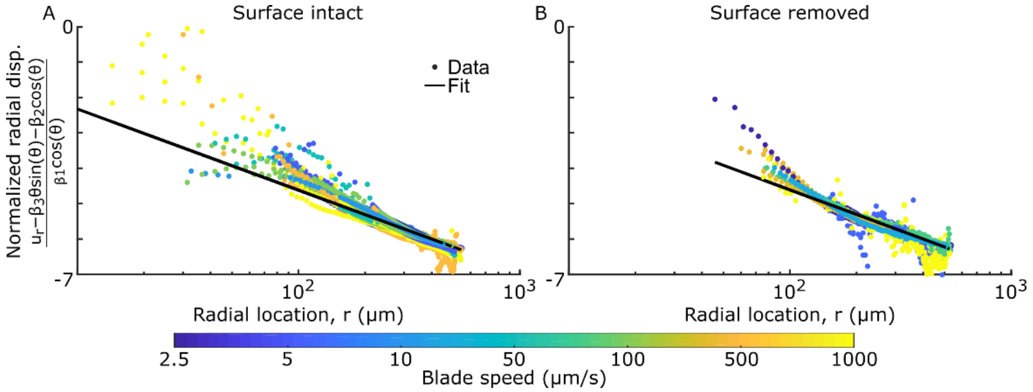

Figure 4.9. Cuts of the 2D displacement data and associated 2D fits to the functional form predicted by contact mechanics. Data and fits are shown for (A) surface-intact and (B) surface-removed samples, with cuts take at $\theta = 0°$. The data and fits were scaled based on the fitting parameters and are shown on a linear-log plot to emphasize the collapse and logarithmic scaling of the data. Note, this is the same data as shown in Figure 4.6, but scaled.

It is also interesting to inspect the values of the fitting coefficients obtained from these fits (β_i in Equation 4.2). Although β_2 is difficult to interpret due to the unknown influence of the scaling constant (*R*), fitted values for β_1 and β_3 can be directly calculated by assuming reasonable values of the Poisson's radio, ν, and Young's modulus, *E*, taken from the literature, and values of P = F_C/(3 mm) from this study. Assuming ν ≈ 0.0 to 0.5, E ≈ 1 to 50 MPa, and F_C ≈ 0.5 to 0.9 N, we expect β_1 ≈ 1 to 200 μm and β_3 ≈ 0 to 100 μm. The actual coefficients for β_1 and β_3 did agree with the expected values. The coefficient values are summarized in Table 4.3 and Figure 4.10. Note that, on average, values for β_1 and β_3 were higher for surface-intact samples, which is expected since the modulus of the surface layer is smaller and β_1 and β_3 are both inversely proportional to *E*.

	Surface intact			**Surface removed**		
	β_1	**β_2**	**β_3**	**β_1**	**β_2**	**β_3**
Mean (μm)	42.3	330	20.0	16.7	164	5.27
Standard error (μm)	4.9	33	1.8	2.9	19	1.1

Table 4.3. Fit coefficients for surface-intact and surface-removed samples obtained by fitting local displacement data to Equation 4.2 in a 2D, least-squares sense. For each coefficient, the average value and the standard error of the mean are shown.

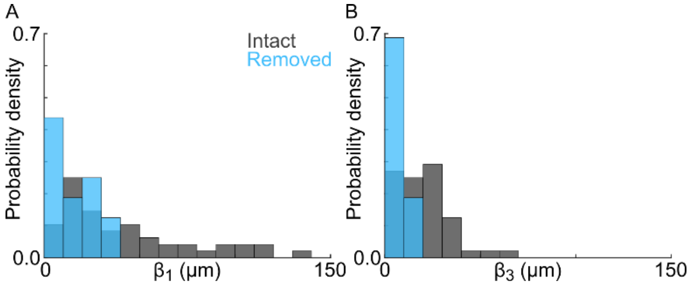

Figure 4.10. Histograms of the fit coefficients (A) β_1 and (B) β_3 obtained by fitting local displacement data to Equation 4.2. Note that, the values lie in the expected range of values and values for surface-intact samples are generally higher than surface-removed.

4.7.5 Toughness calculation

In the current study, the primary focus was on damage initiation in articular cartilage. However, the propagation of existing cracks is also an important and understudied issue relevant to articular cartilage. A handful of studies have applied traditional and more novel fracture tests to characterize the toughness of articular cartilage and other soft biomaterials[123,125,127,132]. When characterizing this crack propagation, many studies extract a measure of the toughness material property, or the ability of the material to resist cracking, based on the strain energy release rate (i.e. energy released per crack area). These existing studies observed toughness values from 140 J/m^2 to over 1000 J/m^2 for articular cartilage. Although not the main focus of the present study, the bulk data after the first-cut provides a window to explore crack propagation in our system.

To estimate a measure of toughness from the present study, we analyzed the bulk force-displacement data after the first-cut, i.e. during the sawtooth-region. In particular, we anticipate that a taller and wider sawtooth implies a tougher material, since the energy build-up and loss during this time should reflect the strain energy released to create the new crack surface. To isolate these regions of strain build-up, the derivative of the force was thresholded to determine points during energy build-up (i.e. with positive slope) and only these areas were integrated, as depicted in Figure 4.11A. This energy was then divided by the final crack area, as determined by confocal images taken after each experiment (depth- and surface-profiles). This toughness measure was fit to a reduced mixed-effects linear model to determine significant effects with a random effect for animal, following the same procedure for linear models of the cut force, depth, and energy (as described in §4.3.3 and shown in Figure 4.2B-D). Note that this measure of toughness effectively excludes the first-cut. Based on the confocal videos, we estimate this first cut to be about 10 –

50 µm deep in undeformed coordinates. Instead, this measure of toughness applies to the tissue depth from after this first cut through the final cut depth, which is usually many-hundred microns. As such, the toughness comparison measure does not apply to the most superficial ~50 µm and is also likely a slight underestimation of the full value.

The results of this toughness measure are shown in Figure 4.11B as a function of surface condition and blade speed. As with the other bulk results (Figure 4.2B-D, Table 4.1), these were the only two significant factors in the linear model (Table 4.4). Averaged across blade speed, the toughness was 32.3 J/m^2 for surface-intact samples and 68.0 J/m^2 for surface-removed samples.

These results suggest that (after the first 20-50 µm) toughness increases with depth into the tissue. As mentioned previously in §4.5, it is especially interesting to note that our measure of toughness is closest to that measured by Chin-Purcell and Lewis[123]. This study measured a toughness of 140 J/m^2 for their most brittle-like samples and this brittle-like fracture is most comparable to the experimental system used in this study. However, in both surface-intact and surface-removed samples, our measure of toughness is lower than those reported elsewhere in the literature, which may reflect limitations of the current calculation. This measure of toughness also has a slight dependence on blade speed. Since toughness is a material property, this rate dependence is non-ideal and may reflect time-dependent strain relaxation and energy dissipation in the tissue that is not appropriately incorporated into the current calculation.

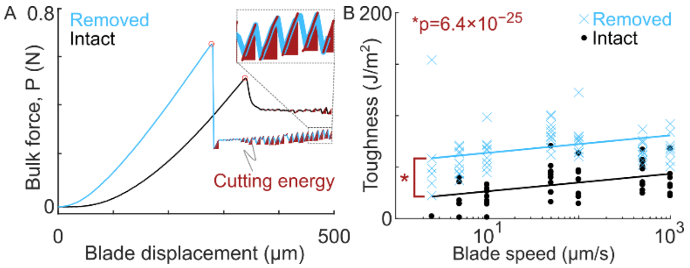

Figure 4.11. (A) Characteristic force vs. blade displacement curves for one surface-intact and one surface-removed sample, up to the blade turn-around point. Both samples were taken from the 10 μm/s blade speed group and are the same samples shown in Figure 4.2A. For all samples, the energy expended during the full cutting time was integrated, as depicted by red areas. This energy was divided by the final cut area as a measure of toughness. (B) The toughness for all experiments (circles or crosses), shown with the corresponding reduced linear model fits (solid lines), for surface-intact (black) and surface-removed (blue) samples. This measure of toughness was significantly dependent on blade speed (p-value: 3.1×10^{-5}) and surface condition, with surface-removed having a higher toughness (p-value: 6.4×10^{-25}).

	Parameter A			**Parameter B**		**Goodness of fit**
Response = A + B × ln(blade speed)	Parameter value		p-value	Parameter value	p-value	Adjusted R^2
	Intact	Removed	Intact vs. Removed	Intact or Removed	Value vs. zero	
Toughness (J/m^2)	54.9	17.6	6.4×10^{-25}	3.71	3.1×10^{-5}	0.64

Table 4.4. Coefficients, significance values, and goodness of fit values for the linear mixed-effects models of toughness as shown in Figure 4.11. In all cases, the full model originally included random effects for source animal and fixed effects for log of the blade speed, surface condition, storage time before testing, orientation in the joint, and condyle, with all interaction terms. The model was then reduced by removing insignificant higher-order fixed effects ($p > 0.01$), resulting in the final two-parameter model shown here.

CHAPTER 5. 3D MICROSCALE FLOW OF POLYMER COATINGS ON GLASS DURING INDENTATION

Bartell, L. R., Lin, N. Y. C., Lyon, J. L., Sorensen, M. L., Clark, D. A., Lockhart, M. J., Matthews, J. R., Glaesemann, G. S., DeRosa, M. E., Cohen, I. *MRS Communications* **7,** 896–903 (2017).

5.1 Abstract

We present an indentation-scope that interfaces with confocal microscopy, enabling direct observation of the 3D microstructural response of coatings on substrates. Using this method, we compared microns-thick polymer coatings on glass with and without silica nanoparticle filler. Bulk force data confirmed the >30% modulus difference, while microstructural data further revealed slip at the glass-coating interface. Filled coatings slipped more and about two times faster, as reflected in 3D displacement and von Mises strain fields. Overall, these data indicate silica-doping of coatings can dramatically alter adhesion. Moreover, this method compliments existing theoretical and modeling approaches for studying indentation in layered systems.

5.2 Introduction

Protective coatings are widely used and studied across science, technology, and engineering. For example, coatings enhance the chemical stability of organic materials and semiconducting photoelectrodes[7,8], protect metals from corrosion[9], and inhibit mechanical damage in glasses[10]. Organic polymeric coatings are commonly employed due to their high processability and photo-curability. For many years, these polymeric materials have been further enhanced by the addition of a second material phase. In particular, many recent studies focus on small, rigid inorganic additives, such as glass or ceramic nanoparticles. Such nanoparticle additives are useful because they increase the coating toughness without substantially decreasing the modulus, increasing the viscosity, or changing the glass transition temperature[145–148].

Indentation testing is a common and versatile technique for understanding material behavior, including in coated systems. For example, indentation tests are used to measure coating hardness[149], coating-substrate adhesion[150], fracture properties of the coating and substrate[10,151], and coating and substrate moduli[152–154]. Such data are also utilized to compare various models of the substrate and coating material behavior[11–15]. Traditional methods include extracting bulk force-displacement data during indentation with Vickers or ball-type tips[154], with the possible addition of a video recording during indentation[150,155] and surface analysis after tip retraction[152]. Instrumented nanoindentation, with the possible addition of concurrent 2D microscopy, is used to study thin-film coatings[11,156,157]. On a larger length scale, one study has used 3D confocal microscopy to extract the displacement of a ball indenting hydrogel, thus measuring the bulk hydrogel modulus[153].

Despite the real-world utility of coatings and the large variety of research on the indentation behavior of coated systems, few techniques enable researchers to directly observe the microscale material behavior under indentation, especially in a fully 3D context. This structural information is of great interest to a variety of fields and, if available, would enable researchers to address a diverse array of questions about the microscale response of polymeric coatings, the effect of nanoparticle fillers, and how such coating-substrate systems ultimately fail.

To address this knowledge-gap and better understand coating-substrate systems, we developed an indentation-scope that interfaces with fast confocal microscopy to directly measure both bulk and 3D microscale responses of a coated glass system during the entire indentation process. In particular, we applied this technique to study the behavior of a microns-thick UV curable epoxy-based coating on glass and compared plain coatings (unfilled) to those with silica nanoparticle filler. We observed coating pile-up around the tip in all samples and our results confirm a slightly higher force response in filled coatings, reflecting their ~50% larger modulus. We also observed slip at the coating-glass interface in all samples. Interestingly, the area of slip was not only larger in filled coatings, but developed at a faster rate with indenter displacement, potentially implying a different mechanism of slip growth.

5.3 Methods

5.3.1 Instrument

To observe the structural response of coatings during indentation, we designed a custom indentation-scope that interfaces with a confocal microscope. The schematic of our setup geometry is shown in Figure 5.1a. The sample (coating on glass coverslip) was clamped between two annular sample holders and attached to a three-axis piezoelectric motor with a travel range of 300 µm and accuracy of ± 2 nm in the *z* direction (not depicted; P-563.3CD, Physik Instrumente, Karlsruhe, Germany). The diamond tip (4-sided pyramid indenter, 120° between faces; Gilmore Diamond, Attleboro, MA) was fixed to a load cell, which was mounted on the indentation apparatus. The load cell had a force measurement range of 44.5 N (10 lb) and was connected to a strain gauge amplifier (LSB200 and CSG110, Futek, Irvine, CA), digitized at 100 points per second using a

USB DAQ (12 bits analog input resolution; USB-6000, National Instruments, Austin, TX). With 2 mV/V gain and 10 V excitation, this setup can resolve forces to ± 2 mN. During indentation tests, the load cell and diamond tip remained stationary while the piezo motor moved the sample upward toward the tip. Because the load cell was stationary, the force measurement was not subject to inertial effects. The sample was moved toward the tip at 0.15 μm/s, producing quasi-static measurements. Force output is shown in Figure 5.1b. This indentation apparatus was based on a previously-developed multiaxial confocal-rheoscope[158].

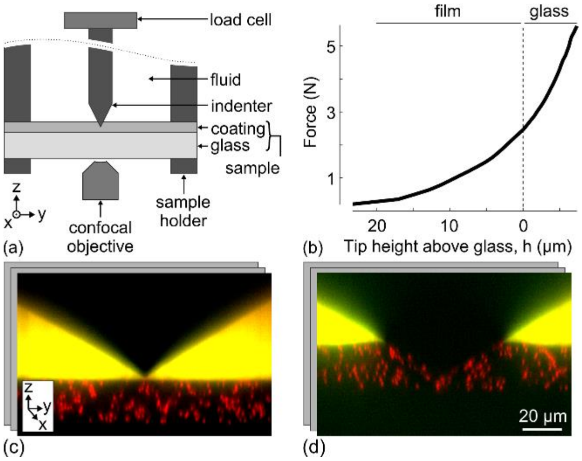

Figure 5.1. Schematic of experimental setup and results. (a) Diagram of confocal indentation-scope where the sample holder is connected to a piezoelectric motor (not shown) and drives the coated glass sample up into the diamond indenter. During the experiment bulk force data was collected from the load cell and local sample deformation is observed from below using an inverted confocal microscope. (b) Force plotted against tip height (tip-to-glass distance, h) for each experiment (dashed lines) and the group average (solid lines) for plain and filled coatings. The tip hits the glass-coating interface at height h = 0 μm. Above 20 μm, the tip is above the coating and below 0 μm the tip is in the glass. Brackets above the plot area indicate the three stages of indentation used for comparing the coatings' flows. (c) Representative *yz* projection of the 3D confocal data showing the system (c) before and (d) during indentation.

To image the 3D microstructure of the coating, the indentation apparatus interfaced with a high-speed, line-scanning confocal microscope (LSM 5 Live, Carl Zeiss Microscopy LLC, Jena, Germany), with a 100× objective (Zeiss Plan-aprochromat 100× 1.4 NA oil DIC objective, 340 μm total working distance) that was mounted on a high-speed piezo focusing motor for rapid *z*-actuation (P-725.2CD PIFOC, Physik Instrumente, Karlsruhe, Germany). The entire field of view

(128 μm × 128 μm × 90 μm; 512 pixels × 512 pixels × 400 pixels) was collected in ≈ 6.7 s. Full, 3D image stacks were collected throughout the experimental time at a rate of 1 stack per 11.84 s, for a total experimental time of about 950 s. Example *xz* confocal slices are shown in Figure 5.1c. The microscope imaged through the glass substrate to capture the coating and diamond tip above it. Thus, a thin, coverslip-thickness glass was used as the substrate (200 μm-thick Corning® Willow® glass, Corning Incorporated, Corning, NY). We used finite element analysis to estimate the deformation of the glass substrate during indentation and found the maximum strain to be ≈ 1%, significantly less than the strain within the coating.

5.3.2 Materials

In this experiment, we tested two different coating formulations obtained from Corning Incorporated: plain UV-curable epoxy coating, and a UV-curable epoxy coating with ≈20 nm diameter silica particles uniformly dispersed at ≈30% volume fraction and bonded to the epoxy coating. The plain (unfilled) coating was comprised of 48 wt% of 3,4 epoxycyclohexylmethyl -3,4 epoxy-cyclohexane carboxylate (Syna Epoxy 06, Synasia Inc., Metuchen, NJ), 48 wt% 3-Ethyl-3-oxetanemethanol (S-101, Synasia Inc., Metuchen, NJ) as a crosslinker. The filled coating was comprised of 48 wt% cycloaliphatic epoxy resin (Nanopox C620 Evonik Industries, Essen, Germany, which contains 40 wt% epoxy functionalized nanosilica,) and 48 wt% oxetane crosslinker (Nanopox C680 Evonik Industries, Essen, Germany, which contains 50 wt% epoxy-functionalized nanosilica,). Both formulations contained 1 wt% cationic photoinitiator (UVI-6976, Dow Chemical Co., Midland, MI) and 3 wt% adhesion promoter (A-186, Momentive Performance Materials Inc., Waterford NY). These two epoxy bases have different tradenames but are equivalent other than the addition of nanosilica filler. The plain and filled coatings had a storage modulus of 2464 MPa and 4222 MPa, respectively, as measured using dynamic mechanical analysis at 25°C (DMA Q800, TA Instruments, New Castle, DE).

To track the deformation field of the epoxy coating, Poly(methyl methacrylate) (PMMA) particles of diameter 1.8 μm and volume fraction ≈ 8% were included in both coating formulations. These tracer particles were fluorescently labeled with DiIC18 (1,1'-Dioctadecyl-3,3,3',3'-tetramethylindotricarbocyanine iodide; excitation wavelength 565 nm) and thus visible on the fluorescence confocal microscope. All three materials (epoxy, nanosilica particles, and tracer particles) have refractive indices close to that of the coverslip substrate (i.e. 1.51). Therefore, the final coating composite had high optical transparency and minimal aberrations. After adding tracer particles, the coating moduli for plain and filled coatings at 25°C were 2470 MPa and 3682 MPa, respectively.

To prepare plain and filled epoxy samples for imaging, PMMA tracer-particles were added. The PMMA particles were initially dispersed in decahydronaphthalene. The tracer-particle suspension was added into the epoxy after any nanosilica filling, and the mixture was vortexed thoroughly and left under vacuum until the decahydronaphthalene evaporated entirely. Unlike the silica nanoparticles, tracer particles were not functionalized and therefore not covalently bound to the epoxy matrix. We found that the small amount of added tracer-particles did not significantly alter the epoxy viscosity. Importantly, since the tracer particles were mixed with epoxy prior to sample curing, they are firmly entrapped in the coating matrix and flow with the coating during indentation.

The epoxy formulations were then coated onto glass substrates, creating a total of 8 samples (4 of each coating). To prepare the substrate for coating, the glass was first sonicated in a liquid detergent bath (7× cleaning solution, MP Biomedicals, Santa Ana, CA) at 3% concentration for five minutes, and then rinsed with deionized water. After this cleaning process, the epoxy was spin-coated on the glass at 1000 rpm and 1500 rpm for plain and filled epoxies, respectively, in order to achieve a final coating thickness of ≈ 20 µm. After the coating procedure, the samples were immediately cured using a table-top UV oven (2000 Flood, Dymax, Torrington, CT) for three minutes, corresponding to ≈ 10 J/cm^2. We then used the confocal microscope to inspect the cured coating and only kept samples with a uniform coating thickness of 20 µm ± 2 µm. The selected samples were then protected from light and stored at room-temperature for at least one week to finish curing. Fully-cured samples were clamped in the annular sample holder and mounted to the indentation apparatus on the confocal microscope. To visualize the position of the diamond tip and the coating's upper surface during the experiment, we placed a fluorescent fluid (fluorescein-water solution, excitation wavelength 494 nm) on the coating after mounting.

5.3.3 Data analysis

5.3.3.1 Force response

Raw force data from the load cell were first smoothed using a moving-average filter, with a window size of 99 points (0.99 s $\ll$ 11.84 s image time $\ll$ 950 s full experiment time), to reduce noise. Smoothed curves were then re-sampled using nearest-neighbor interpolation to extract the force during each imaging time-point.

5.3.3.2 Coating-glass interface location

Imaging data sets were first analyzed to extract the *z* position of the glass-coating interface over time. At each time point, each slice of the *z* stack was summed in the *xy* plane to obtain an overall intensity, I, versus *z* position. This intensity was low in the glass because the glass is not fluorescent, and high in the coating, due to the fluorescent tracer particles. Images also showed gradual intensity decay with *z* due to slight refractive index mismatches. This overall intensity dependence was fit with a sigmoid plus a linear term,

$$I(z) = \beta_0 + \beta_1\left(1 + e^{(\beta_2 - z)/\beta_3}\right)^{-1} + \beta_4(z - \beta_2),$$

where z is the height of the slice above the bottom of the stack and β_i are fittings constants. Using this model, we extracted β_2 as the interface position.

5.3.3.3 Tip location

After finding the interface, images were analyzed to extract the *z* position of the diamond tip over time. In the first time point, the tip's *z* position was determined manually using the central *xz* projection. This projection was also used to measure the coating thickness. The tip was mounted to the stationary force sensor and thus moves proportional to any applied force. This dependence was calibrated and exploited to determine the relative *z* displacement of the tip from the relative change in force. This method was particularly useful when the tip was in the sample and no longer clearly visible. However, in the first 5-10 time points (tip height $h > 17$ µm), the diamond tip slipped vertically slightly due to slack in the system, violating this linearity. During these time points, the tip height was instead determined by tracking the vertical displacement of the tip itself in the confocal images. This second method was validated by confirming linearity with the force when the tip was not slipping and by manual comparison to the imaging data. Finally, the coating's initial thickness, glass-coating interface *z* position over time, and tip *z* position over time were combined to determine the tip height (tip-to-glass distance, *h*) as a function of time for each experiment. Results are plotted with respect to tip height.

5.3.3.4 Tracer particle paths

At each imaging time-point, the 3D image data was analyzed to locate tracer particles embedded in the coating. Images were analyzed using the 3D, IDL-implementation of the Crocker-Grier particle-finding algorithm to locate the *(x(t), y(t), z(t))* positions of the tracer particles[159]. Particle positions were linked over time using `trackpy`, the python implementation of the related Crocker-Grier particle-tracking algorithm (search range: 1.0 µm, memory: 0 time points, minimum duration 90% of full experiment time).

For each experiment, the coating's flow was divided into three stages of indentation and then analyzed. The three stages of indentation were chosen based on the tip's height above the glass, where stages 1 through 3 include imaging time-points when the tip is 20 µm to 10 µm, 10 µm to 0 µm, and 0 µm to -4 µm from the glass, respectively. Here, negative tip height indicates the tip penetrating into the glass. To understand the coating's flow within each stage, we characterized each particle's trajectory by calculating the total path length,

$$L = \sum [\, (\delta \mathrm{x})^2 + (\delta \mathrm{y})^2 + (\delta \mathrm{z})^2]^{1/2},$$

where $\delta \mathrm{x} = \mathrm{x(t)} - \mathrm{x(t-1)}$*;* the end-to-end displacements in the three Cartesian coordinates,

$$\Delta \mathrm{x} = x(t_{end}) - x(t_{start}),$$

where t_{start} and t_{end} are the first and last time points in the stage (similarly for y and z); and the radial end-to-end displacement,

$$\Delta \mathrm{R} = [\Delta \mathrm{x}^2 + \Delta \mathrm{y}^2]^{1/2}.$$

Initial data indicated slip at the coating-glass interface. To characterize any slip, particles within 3 µm of the coating-glass interface were isolated and those with a radial displacement over a threshold of 0.05 µm/time-step were plotted. The area of slip was characterized by manually fitting an ellipse around these tracks. Due to the intrinsic spacing of tracer particles dispersed in the coating, this method was able to resolve slip areas larger than roughly 1500 µm^2.

Tracer particle paths were also used to compute 3D strain fields. These scattered displacement tracks were interpolated and smoothed on a 5 µm grid using a 3D variation of Barnes interpolation[160]. Lagrange strain fields were calculated from numeric spatial gradients of the displacement fields, via the central difference method. This analysis returned a full 3D strain tensor at each point on the 3D grid, valid for both small and large strains[161].

5.4 Results

5.4.1 Force

Smoothed force data for each experiment are plotted with respect to tip height above glass in Figure 5.1b, along with the averages for each sample group. On average, the force-response in the coating was about 30% stronger in the samples with filled epoxy, reflecting the 50% higher modulus of the coating. However, once the tip penetrated the glass (i.e. $h < 0$ µm), the plain and filled force responses were more similar, as expected, because the glass begins to dominate the response.

5.4.2 Particle paths

The flow of the coating was reflected in the paths of the tracer particles, as shown in Figure 5.2 for the entire indentation experiment and the three individual stages of one experiment. See Supplementary Material for movies of tracer particle paths for every experiment (Movies S1). These traces, especially during the first stage, illustrate how the coating flows to produce a pile-up around the tip. In general, particles closer to the tip moved down and out, perpendicular to the tip's face, while the hard-boundary at the bottom of the coating redirected the force such that particles farther away from the tip move up and out. Separately, tracer particles near the tip-coating-fluid interface immediately moved up and out, parallel to the tip face, creating a small, localized pile-up that was later pushed out laterally. In the later stages of indentation, the tip and glass formed a wedge-like boundary that constrained the coating flow near the tip such that it was dominated by the lateral components.

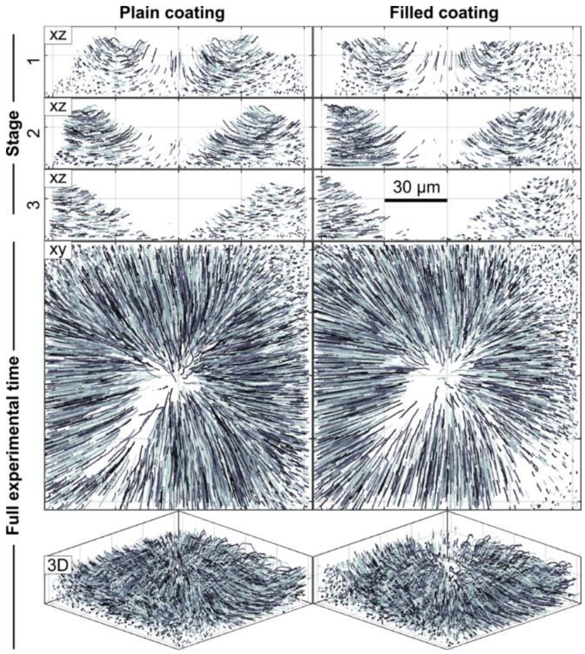

Figure 5.2. Paths of tracer particles in one experiment. For stages 1 through 3, *xz* views of the paths within the range $y = 0$ µm ± 10 µm are shown. Additionally, the paths throughout the entire experiment are shown in *xy* and 3D projections. Each line indicates the path of a different tracer particle. In all plots, paths are shown relative to the glass-coating interface, which is at the $z = 0$ µm plane.

To quantify the coating's flow, we calculated various characteristics of the tracer-particle paths during the three stages of indentation. In particular, Figure 5.3 shows the histograms for total path length, z displacement, and radial end-to-end displacement. Each plot shows the normalized probability density of a particular path characteristic for each individual experiment, and all experiments combined, for plain and filled coatings. As the tip approached and penetrated the glass (stages 2-3), the histograms for the two sample types became increasingly distinct. This was true for all path characteristics except the z displacement, where the two coating formulations both showed relatively small displacements at all stages of indentation.

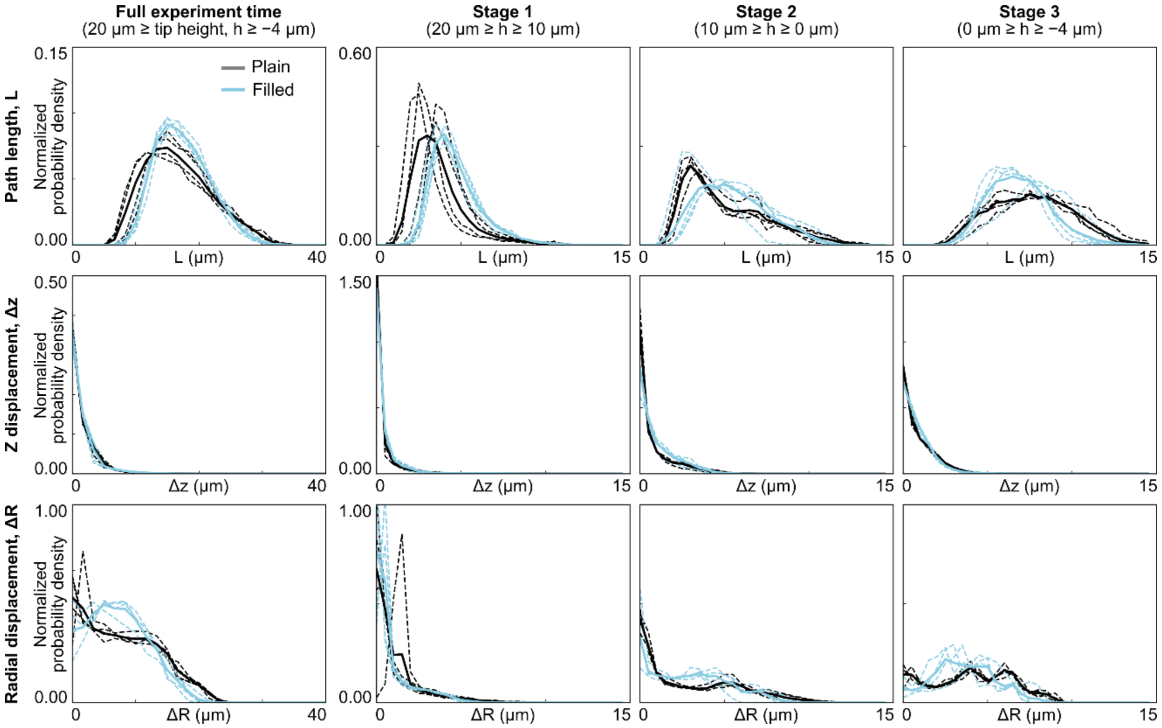

Figure 5.3. Histograms of path characteristics for tracer particles during each stage of indentation. Histograms are shown for each experiment individually (dashed lines), as well as for the population average (thick lines) for plain and filled coatings. In general, the plain and filled coatings become increasingly distinct during the later stages.

As exhibited in Figure 5.3, plain and filled coatings had distinctly different behaviors when comparing their radial flow component. This flow behavior also varied across the coating's depth (i.e. along *z*). Therefore, we further quantified the depth-dependence of the coatings' radial flow. Figure 5.4 shows the normalized probability density of the radial displacement (averaged over all samples of each sample type) plotted as a function of the tracer particles' *z*-position at the start of each stage. Consistent with Figure 5.3, these plots again show that, as indentation progressed, the plain and filled coatings became increasingly distinct. Particles higher above the glass ($z \gtrsim 10$ µm) had similar radial displacements, regardless of filling. However, in the third stage of indentation when the tip approached and penetrated the glass, the tracer particles closest to the glass interface ($z \lesssim 5$ µm) moved farther radially in the filled coatings as compared to the plain coatings. For filled samples, as z approaches the glass interface ($z \rightarrow 0$ in Figure 5.4), the radial displacement approached a finite value (approx. 2 µm), suggesting slip between the filled coating and the glass substrate. Thus, data in this lowest z bin was extracted and analyzed further to characterize interfacial slip.

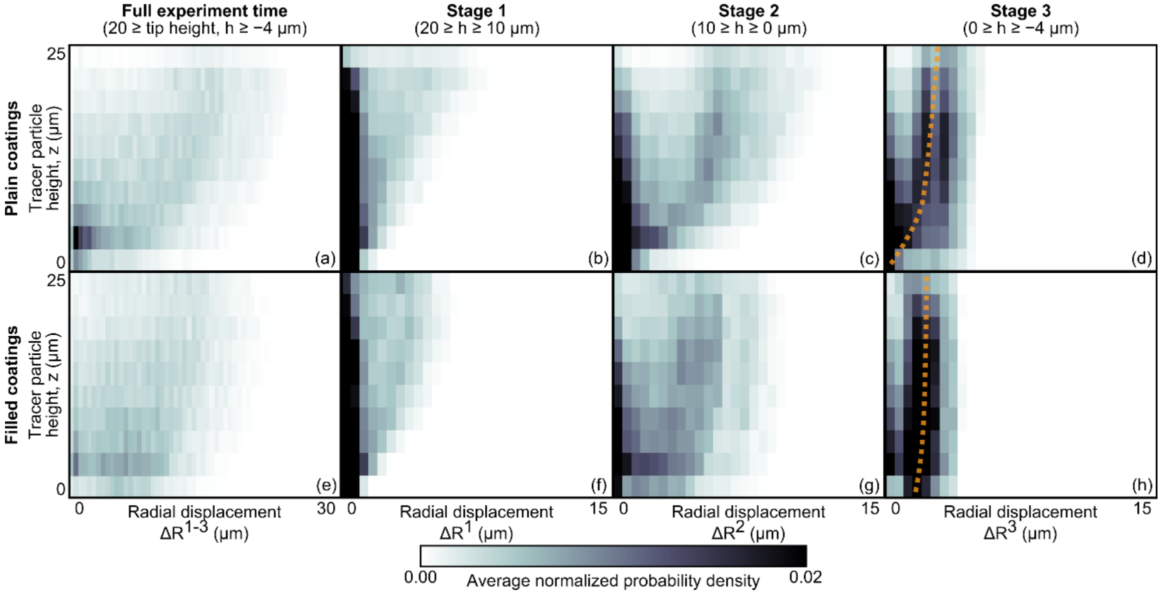

Figure 5.4. Normalized probability density of tracer-particles' radial displacement as a function of height above the glass interface. Results are shown averaged over all experiments for (a-d) plain and (e-h) filled coatings during the entire experiment and the three stages of indentation. The plain and filled coatings have similar behavior in the early stages. However, in stage 3, the trends are distinct for particles near the glass interface. In particular, particles in the filled coatings have a non-zero radial displacement, even at $z = 0$ µm. This trend is illustrated by the dashed lines, which are shown as visual guides.

Slip at the coating-glass interface was investigated further by observing large-displacement paths near the coating-glass interface (Figure 5.5a) and calculating the area of slip (if any) at each time point. Using this method, all samples showed some amount of slip during indentation. As the tip neared the glass (*h* = 0), however, filled coatings generally had a larger slip area (Figure 5.5b). Moreover, the slip area grew at a faster rate in filled samples, as compared to plain coatings.

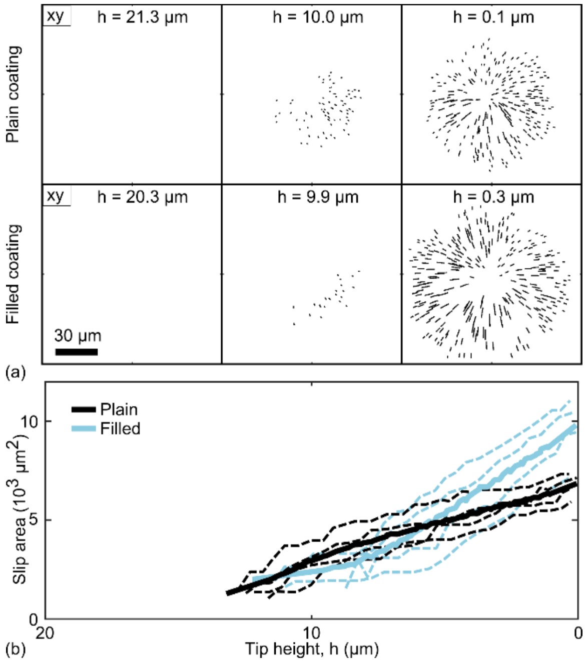

Figure 5.5. (a) XY-views of tracer-particles paths within 3 µm of the coating-glass interface (i.e. 0 µm ≤ z ≤ 3 µm) that displaced radially above a minimum threshold and thus were indicative of interfacial slip. These paths are shown for characteristic samples with plain (first row) and filled (second row) coatings. (b) The slip area calculated from the paths shown in (a), shown as a function of tip height above the glass interface, h. Slip areas are shown for plain and filled coatings, including individual experiments (dashed lines) and group averages (solid lines).

5.4.3 3D strain fields

Tracer particles' paths were analyzed to calculate the local 3D displacement and strain fields in the samples during indentation. To highlight the distribution and magnitude of the strain field and to provide insight regarding nonlinear behavior in the coating, Figure 5.6 shows characteristic surfaces of constant von Mises strain from 5% to 20% for plain and filled samples. These plots show the strain field during indentation when the tip height is zero, i.e. when the diamond tip contacts the coating-glass interface but can be similarly calculated throughout the indentation process. See Supplementary Material for movies of von Mises strain surfaces for all experiments (Movies S2). The threshold yield strain of the plain and filled coatings is unknown and the two may be different. Nonetheless, these constant-strain surfaces highlight the shape and magnitude of the deformation field during indentation, including lobes that correspond to the sharp edges of the pyramid-shaped diamond tip. Interestingly, we observed that the strain in the filled coatings had a similar shape as the strain field in plain coatings, but with a slightly lower volume enclosed within a given contour level. There may also be slight differences in the shape between plain and filled coatings. In particular, we noted that samples with filled coatings tended to have more defined lobes than plain coatings.

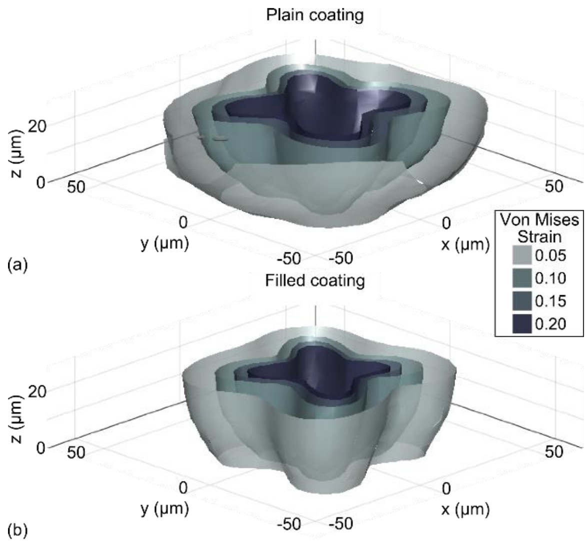

Figure 5.6. Characteristic surfaces of constant von Mises strain highlighted at various levels from 5% to 20%, shown for (a) plain and (b) filled coatings. Both plots show the strain field in undeformed coordinates at the point when the tip is closest to the coating-glass interface (i.e. $h \cong 0$ μm). The four lobes correspond to the four sharp edges of the pyramid-shaped diamond indenter.

5.5 Discussion

This experiment used a custom confocal method to visualize the 3D behavior of thin epoxy coatings on glass substrates during indentation with a pyramid-shaped diamond tip (Figure 5.1). In addition to recording the bulk force and tip-displacement response, tracer particles embedded in the coatings were tracked in 3D during indentation in order to measure the microscale flow behavior within the coating, including displacement and strain fields. Coatings with and without nanosilica bead filler were compared to elucidate the effects of nanosilica doping.

In bulk measurements (Figure 5.1b), filled coatings exhibited ≈ 30% higher force than plain coatings. This is consistent with, though slightly lower than the ≈ 50% modulus enhancement due to filling, as measured by traditional mechanical testing of the bulk material. On the microscale, the flow fields of plain and filled coatings became increasingly distinct in stages 2 and 3, as the tip approached and penetrated the glass. In particular, in the filled samples, tracer particles flowed farther laterally (Figure 5.2 and Figure 5.3). In filled coatings, the radial displacement as a function of particle height approached a non-zero value as height tended toward zero (Figure 5.4). These differences implied slip at the coating-glass interface, which was more pronounced in filled coatings. Thus, slip was characterized by observing the tracer particle paths near the interface with large radial displacements (Figure 5.5a). Using this method, slip at the interface was observed in all samples. However, as the tip neared the glass interface, filled samples showed a larger slip area which developed at a faster rate with respect to tip height, *h* (Figure 5.5b). This higher magnitude and rate of slip could be explained by the presence of the nanosilica beads. For example, consider the mechanisms illustrated in Figure 5.7. Initially, the nanosilica beads, if present, would be chemically bonded to the glass substrate[146,162]. Because of this structure, as the coating deforms laterally, the polymer connection between the bead and glass would be increasingly tensed to the point of rupture (Figure 5.7a). However, without beads, this strain could dissipate throughout a larger network structure, thus avoiding rupture. Similarly, the nanosilica beads are very stiff relative to the surrounding polymer network. Thus, once slip has started, it could proceed more rapidly in filled coatings because the beads would absorb comparatively little deformation, and instead transfer forces further laterally, enhancing slip growth (Figure 5.7b).

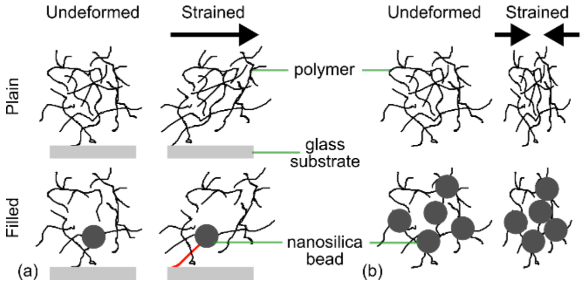

Figure 5.7. Illustration of the proposed mechanisms of slip in plain and filled coatings. (a) In plain coatings, the entire polymer network can absorb shear strain. In filled coatings, however, the silica nanoparticles bond directly to the glass interface, leading to strain concentration and failure of this bond. (b) Because nanosilica particles are very stiff compared to the surrounding polymer network, compressive strain may cause relatively more densification in the filled coating and this may subsequently explain the different rates of slip observed in plain verses filled coatings.

Tracer particle tracks were also used to compute local 3D strain fields throughout the indentation process. In particular, the local von Mises strain had a consistent shape across all experiments, including four lobes of high strain around the corners of the pyramid indenter (Figure 5.6). While the shape was similar, the overall volume contained in a given strain contour was consistently lower in the filled coatings as compared to plain, despite at equal tip height (*h* = 0; i.e. equal strain boundary conditions). Also, the filled-coating samples retained more distinct lobes. This observation may again be explained by the differences in interfacial slip between the two samples. Importantly, the strain measured here represents strain in the coating material only (i.e. material strain) and does not incorporate any effective strain from relative coating-glass displacement. As a result, slip would serve to reduce the strain measured in the coating. Similarly, increased slip would reduce any effective “pinning” of the strain field at the glass interface, thus freeing the strain field to retain the lobe shape resulting from the diamond-tip’s geometry.

Slip is common in these coated-glass systems and previous studies have used indentation testing and the onset of slip to study adhesion and failure. For example, Ritter et. al. developed microindentation to measure adhesive shear strength of polymer coatings on glass, using both a ball and Vickers-type indenters[150,155]. Slip may also be important for load transfer between coating and substrate and thus have important implications for the ability of such coatings to protect underlying glass. In future work, it would be interesting to examine the relationship between nanoparticle filler concentration, coating-glass adhesion, and coating properties after plastic deformation. Recent literature has lauded the benefits of nanosilica beads in polymer coatings for increasing toughness without compromising other mechanical benefits[145–148]. The results of this study reveal that nanosilica filled coatings may be more susceptible to interfacial slip at a glass surface than plain coatings. This effectively reduces the material strain in filled coatings and likely alters the stress field in the underlying glass while increasing the energy absorbed at the interface.

Understanding local coating behavior is essential for studying coated glass systems as a whole. Ritter et. al. also observed pile-up around the indenter in polymer coated glass systems and applied a load-sharing model to understand the bulk force response[10,149]. Others have similarly developed theoretical models and used simulation and finite element modeling to understand the local distribution of stresses in coated or layered systems[11,15,156]. In contrast, the method developed here enables direct experimental visualization of the local coating deformation, complementing existing theoretical and modeling approaches. The method used in this study could also be repeated with the addition of stress-sensitive dyes to enable direct, 3D visualization of the stress field[163,164].

This method provided detailed information about indentation but was not without limitations. In particular, confocal imaging requirements limit sample geometry and introduce trade-offs between resolution and field-of-view. In order to achieve high spatial resolution, a high magnification objective with a correspondingly low working distance of about 100 µm was used. Similarly, high magnification corresponds to small field-of-view and important sample behaviors may occur on larger lateral length scales, outside the imaging field. Also, despite high-speed imaging, it takes multiple seconds to image the entire field-of-view, thus limiting the temporal resolution. Despite these limitations, the imaging parameters may be adjusted to capture the physical time and length scales of interest. This technique is also limited by the tracer particles. Not only must they be incorporated, but the imaging resolution must be appropriate to track these tracer particles, though their size is somewhat adjustable. The amount and distribution of tracer particles similarly sets the spatial resolution of resulting 3D displacement and strain fields. Nonetheless, the tracer particles enable the local 3D microscale deformation and strain to be tracked *in situ*.

Overall, the method presented here provides unprecedented access to information about microscale processes in 3D throughout indentation. In particular, we directly observed and quantitatively characterized indentation flow *in situ* on the micrometer scale in order to better understand glass-coating interactions, adhesive failure, and the role of silica nanoparticle fillers. This experimental method directly complements existing theoretical and modeling approaches to understanding these phenomena and is applicable to a wide array of mechanical phenomena.

5.6 Acknowledgments

L.B. and I.C. were supported by an award from Corning Incorporated to Cornell University. N.L. and I.C. were supported by NSF DMF-CMP award no. 1507607. J.L., M.S., D.C., M.L., J.M., G.G., and M.D. are full time employees of Corning Incorporated.

CHAPTER 6. CONCLUSIONS

6.1 Conclusions

Reflecting on the work presented here, we see that imaging in concert with spatiotemporal analysis is an exciting and useful avenue for relating the complex mechanical behavior of a system, such as articular cartilage, to its function and dysfunction.

In articular cartilage, we discovered that traumatic impact induces rapid, strain-dependent mitochondrial dysfunction and cell death in chondrocytes (Chapter 2-Chapter 3). Understanding this relationship between injury mechanics and cellular dysfunction, as well as its rapid temporal evolution, is central to elucidating the mechanotransduction pathways that lead from injury to disease. Furthermore, understanding this evolution enabled us to test promising mitoprotective drugs that directly target mitochondria structure and may arrest the downward spiral into joint dysfunction (Chapter 3). More broadly, these studies demonstrate the utility of combining imaging data and analysis from disparate sources (e.g. fast camera elastography plus microscopy assay segmentation and classification) to investigate the detailed biomechanics and mechanobiology relationships that regulate tissue function.

In addition to understanding the acute pathogenesis of joint disease, we also discovered that the heterogeneous, layered properties of articular cartilage may serve to protect the tissue, both biologically and mechanically (Chapter 2, Chapter 4). From the cellular perspective, we found that, because cell death after impact is correlated with impact strain, the compliant surface layer of cartilage can absorb load and thus may protect the underlying cells during injury (Chapter 2).

Similarly, from the perspective of mechanical integrity, we found that the presence of the surface layer delays the onset of matrix cracks in articular cartilage (Chapter 4). These discoveries have important clinical implications, particularly because cracks in cartilage are commonly observed after traumatic injury and because joint disease involves the mechanical degradation of the tissue, especially from the articular surface. Taken together, these studies highlight the importance of preserving cartilage's layered structure for maintaining the mechanical and biological homeostasis necessary for cartilage function in the joint. Paradoxically, however, these results also suggest a 'sacrificial' surface layer, wherein the superficial cells experience more extreme loading and are thus more likely to die, which in term compromises the mechanical integrity of that important surface layer. While this paradox could be true, it more likely points to a complicated relationship between biomechanics and mechanobiology of articular cartilage. Perhaps chondrocytes in the superficial layer are more likely to recover or regenerate after injury, or perhaps their response to loading is different than chondrocytes in the bulk of the tissue. These are new and important questions that we hope will be resolved by future studies.

6.2 Future directions

The natural end of any research project is not simply the end, but an open door to other fascinating ideas that continue to move the field forward. After conducting these studies on cartilage biomechanics and mechanobiology, many promising future directions await our study, including those detailed below.

6.2.1 Mechanobiology and the peracute-to-acute evolution of chondrocyte dysfunction after articular cartilage injury

As shown in this thesis, cellular dysfunction in articular cartilage begins within minutes of injurious loading, with important implications for targeted treatment of cartilage degradation. However, the full temporal evolution of chondrocyte response to injury is not yet well-understood. In a recent paper, Anderson et. al. outlined the conceptual framework of the various known waves of cellular response to injury, including early necrosis and inflammation, as well as the catabolic-to-anabolic transition that occurs many days later[2]. Though useful, an important knowledge gap remains: How do individual cells navigate through these various "states" over time? Moreover, how do the mechanics of injurious loading and any therapeutic treatments influence this temporal evolution? Indeed, we now wonder: If peracute chondrocyte dysfunction is strongly regulated by mechanotransduction via mitochondria, is this also true of the later, acute dysfunction? Given the methods developed in this thesis, we are now well-equipped to answer these questions. By upgrading the custom impactor developed in Chapter 2 to facilitate long-term sterile culture[i], cartilage explants could be injured and then cultured over longer times, enabling periodic checks via fluorescence microscopy assays and media analyses. A corresponding statistical analysis of individual cell state (e.g. via survival analysis) could then determine how factors such as treatment and injury mechanics influence cells' injury response. Moreover, analogous to the study by Garrido et. al., culturing unimpacted control samples either in the same or a separate bath as their impacted counterpart would further elucidate which of these chondrocyte responses are signaled via mechanical stimulation verses chemical communication[165]. Answering these questions would complement our understanding of the peracute (minutes-to-hours) response, would reveal to what degree injury mechanotransduction influences the acute (hours-to-weeks) dysfunction, and would enable researchers to optimize drug treatments and therapies accordingly.

6.2.2 Double-network hydrogels and crack propagation in articular cartilage

Despite the progress presented in this thesis, the development of cracks in articular cartilage remains an understudied yet important problem. In particular, there is no accepted unifying model governing cracks in cartilage and, as such, individual studies characterizing cracks are of limited utility. Establishing such a model would be of broad interest and provide utility for understanding why cracks develop, predicting when and where cracks will happen (e.g. via patient specific modeling), and preventing cracks clinically. Interestingly, one observation from Chapter 4 is the parallel between toughness in articular cartilage and that in double-network hydrogels. For example, during blade indentation, cartilage deformation appears similar to that of double-network hydrogels[139,166]. Also, initial studies of a double-network, rigidity-percolation model of articular cartilage show promising parallels between crack propagation in the model and that observed in notch-tests of cartilage[37,167,168]. In double-network hydrogels, the first network is a rigid skeleton which may be analogous to the collagen network in cartilage, while the second, energy-dissipating network may be analogous to the charged proteoglycan network in cartilage. Thus, one future direction of this work would be to explore these parallels between double-network models and cartilage material failure in more detail. In particular, to validate the predictive power of a double-network model for understanding cartilage failure, it would be interesting to conduct a two-part study. First, to demonstrate the applicability of such a model, one study could test a double-network, rigidity-percolation model in a traditional notch-test geometry and compare this model's predicted local deformation and critical-load at crack propagation to that observed in real cartilage samples via confocal elastography during an analogous notch-test. Second, in order to validate the model, it would be especially interesting to enzymatically degrade cartilage's proteoglycan network, model a similar loss of the secondary network in the double-network model, and again compare the results regarding deformation and failure in a notch-test[169,170]. If a double-network model can recapitulate the failure response of both normal and degraded cartilage, this result would show that the model can be tuned to predict cartilage material property changes. This observation would further solidify the importance of cartilage's double-network structure in governing its mechanical function and failure. This interpretation of cartilage as a double-network material would be especially interesting because, in cartilage, degradation of the proteoglycan network is a hallmark of joint damage and disease. Understanding the interplay between cartilage matrix constituents, cartilage's network structure, and subsequent material failure would provide broad insight regarding cartilage homeostasis and dysfunction, both as an engineering material and as a critical tissue for health joint function.

BIBLIOGRAPHY

1. Mow, V. C., Ratcliffe, A. & Robin Poole, A. Cartilage and diarthrodial joints as paradigms for hierarchical materials and structures. *Biomaterials* **13,** 67–97 (1992).

2. Anderson, D. D. *et al*. Post-traumatic osteoarthritis: Improved understanding and opportunities for early intervention. *J. Orthop. Res.* **29,** 802–809 (2011).

3. Brown, T. D., Johnston, R. C., Saltzman, C. L., Marsh, J. L. & Buckwalter, J. A. Posttraumatic Osteoarthritis: A First Estimate of Incidence, Prevalence, and Burden of Disease: *J. Orthop. Trauma* **20,** 739–744 (2006).

4. Krasnokutsky, S., Attur, M., Palmer, G., Samuels, J. & Abramson, S. B. Current concepts in the pathogenesis of osteoarthritis. *Osteoarthritis Cartilage* **16,** S1–S3 (2008).

5. Goldring, M. B. & Goldring, S. R. Articular cartilage and subchondral bone in the pathogenesis of osteoarthritis. *Ann. N. Y. Acad. Sci.* **1192,** 230–237 (2010).

6. Scott, C. C. & Athanasiou, K. A. Mechanical Impact and Articular Cartilage. *Crit. Rev. Biomed. Eng.* **34,** 347–378 (2006).

7. Garcia Parejo, P., Zayat, M. & Levy, D. Highly efficient UV-absorbing thin-film coatings for protection of organic materials against photodegradation. *J. Mater. Chem.* **16,** 2165–2169 (2006).

8. Hu, S. *et al.* Thin-Film Materials for the Protection of Semiconducting Photoelectrodes in Solar-Fuel Generators. *J. Phys. Chem. C* **119,** 24201–24228 (2015).

9. Wang, D. & Bierwagen, G. P. Sol–gel coatings on metals for corrosion protection. *Prog. Org. Coat.* **64,** 327–338 (2009).

10. Ritter, J. E., Gu, W. & Lardner, T. J. Effectiveness of polymer coatings on reducing indention damage in glass. *Polym. Eng. Sci.* **32,** 1372–1378 (1992).

11. Hakiri, N., Matsuda, A. & Sakai, M. Instrumented indentation microscope applied to the elastoplastic indentation contact mechanics of coating/substrate composites. *J. Mater. Res.* **24,** 1950–1959 (2009).

12. Silbernagl, D. & Cappella, B. Mechanical properties of thin polymer films on stiff substrates. *Scanning* **32,** 282–293 (2010).

13. Bhattacharya, A. K. & Nix, W. D. Analysis of elastic and plastic deformation associated with indentation testing of thin films on substrates. *Int. J. Solids Struct.* **24,** 1287–1298 (1988).

14. Hirst, W. & Howse, M. G. J. W. The Indentation of Materials by Wedges. *Proc. R. Soc. Lond. Math. Phys. Eng. Sci.* **311,** 429–444 (1969).

15. Gao, X.-L., Jing, X. N. & Subhash, G. Two new expanding cavity models for indentation deformations of elastic strain-hardening materials. *Int. J. Solids Struct.* **43,** 2193–2208 (2006).

16. Data and Statistics | Arthritis | CDC. (2017). Available at: https://www.cdc.gov/arthritis/data_statistics/index.htm. (Accessed: 23rd April 2018)

17. Zhang, Y. & Jordan, J. M. Epidemiology of Osteoarthritis. *Clin. Geriatr. Med.* **26,** 355–369 (2010).

18. Mow, V. C., Ateshian, G. A. & Spilker, R. L. Biomechanics of Diarthrodial Joints: A Review of Twenty Years of Progress. *J. Biomech. Eng.* **115,** 460–467 (1993).

19. Hayes, W. C. & Bodine, A. J. Flow-independent viscoelastic properties of articular cartilage matrix. *J. Biomech.* **11,** 407–419 (1978).

20. Mow, V. C. & Mansour, J. M. The nonlinear interaction between cartilage deformation and interstitial fluid flow. *J. Biomech.* **10,** 31–39 (1977).

21. Mow, V. C., Holmes, M. H. & Michael Lai, W. Fluid transport and mechanical properties of articular cartilage: A review. *J. Biomech.* **17,** 377–394 (1984).

22. Roth, V. & Mow, V. C. The intrinsic tensile behavior of the matrix of bovine articular cartilage and its variation with age. *J. Bone Jt. Surg.* **62,** 1102–1117 (1980).

23. Below, S., Arnoczky, S. P., Dodds, J., Kooima, C. & Walter, N. The split-line pattern of the distal femur: A consideration in the orientation of autologous cartilage grafts. *Arthrosc. J. Arthrosc. Relat. Surg.* **18,** 613–617 (2002).

24. Benninghoff, A. Form und Bau der Gelenkknorpel in ihren Beziehungen zur Funktion. *Z. Für Zellforsch. Mikrosk. Anat.* **2,** 783–862 (1925).

25. Schinagl, D. R. M., Ting, M. K., Price, J. H. & Sah, R. L. Video microscopy to quantitate the inhomogeneous equilibrium strain within articular cartilage during confined compression. *Ann. Biomed. Eng.* **24,** 500–512 (1996).

26. Buckley, M. R., Bonassar, L. J. & Cohen, I. Localization of Viscous Behavior and Shear Energy Dissipation in Articular Cartilage Under Dynamic Shear Loading. *J. Biomech. Eng.* **135,** 031002–031002 (2013).

27. Grodzinsky, A. J., Levenston, M. E., Jin, M. & Frank, E. H. Cartilage Tissue Remodeling in Response to Mechanical Forces. *Annu. Rev. Biomed. Eng.* **2,** 691–713 (2000).

28. Aspden, R. M., Jeffrey, J. E. & Burgin, L. V. Letter to the Editor. *Osteoarthritis Cartilage* **10,** 588–589 (2002).

29. Birchfield, P. C. Osteoarthritis overview. *Geriatr. Nur. (Lond.)* **22,** 124–131 (2001).

30. Jackson, D. W., Simon, T. M. & Aberman, H. M. Symptomatic articular cartilage degeneration: the impact in the new millennium. *Clin. Orthop.* S14-25 (2001).

31. Murphy, L. *et al.* Lifetime risk of symptomatic knee osteoarthritis. *Arthritis Care Res.* **59,** 1207–1213 (2008).

32. Felson, D. T. *et al.* Osteoarthritis: New Insights. Part 1: The Disease and Its Risk Factors. *Ann. Intern. Med.* **133,** 635–646 (2000).

33. Fischenich, K. M. *et al.* Chronic changes in the articular cartilage and meniscus following traumatic impact to the lapine knee. *J. Biomech.* **48,** 246–253 (2015).

34. Radin, E., Paul, I. & Rose, R. Role of mechanical factors in pathogenesis of primary osteoarthritis. *The Lancet* **299,** 519–522 (1972).

35. Vellet, A. D., Marks, P. H., Fowler, P. J. & Munro, T. G. Occult posttraumatic osteochondral lesions of the knee: prevalence, classification, and short-term sequelae evaluated with MR imaging. *Radiology* **178,** 271–276 (1991).

36. Wang, C. C.-B., Deng, J.-M., Ateshian, G. A. & Hung, C. T. An Automated Approach for Direct Measurement of Two-Dimensional Strain Distributions Within Articular Cartilage Under Unconfined Compression. *J. Biomech. Eng.* **124,** 557–567 (2002).

37. Silverberg, J. L. *et al.* Structure-Function Relations and Rigidity Percolation in the Shear Properties of Articular Cartilage. *Biophys. J.* **107,** 1721–1730 (2014).

38. Wong, B. L. *et al.* Biomechanics of cartilage articulation: Effects of lubrication and degeneration on shear deformation. *Arthritis Rheum.* **58,** 2065–2074 (2008).

39. Backus, J. D. *et al.* Cartilage viability and catabolism in the intact porcine knee following transarticular impact loading with and without articular fracture. *J. Orthop. Res.* **29,** 501–510 (2011).

40. Jeffrey, J. E., Gregory, D. W. & Aspden, R. M. Matrix Damage and Chondrocyte Viability Following a Single Impact Load on Articular-Cartilage. *Arch. Biochem. Biophys.* **322,** 87–96 (1995).

41. Newberry, W. N., Garcia, J. J., Mackenzie, C. D., Decamp, C. E. & Haut, R. C. Analysis of Acute Mechanical Insult in an Animal Model of Post-traumatic Osteoarthrosis. *J. Biomech. Eng.* **120,** 704–709 (1998).

42. Repo, R. U. & Finlay, J. B. Survival of articular cartilage after controlled impact. *J. Bone Jt. Surg.* **59,** 1068–1076 (1977).

43. Waters, N. P., Stoker, A. M., Carson, W. L., Pfeiffer, F. M. & Cook, J. L. Biomarkers affected by impact velocity and maximum strain of cartilage during injury. *J. Biomech.* **47,** 3185–3195 (2014).

44. Abusara, Z., Seerattan, R., Leumann, A., Thompson, R. & Herzog, W. A novel method for determining articular cartilage chondrocyte mechanics in vivo. *J. Biomech.* **44,** 930–934 (2011).

45. Guilak, F., Ratcliffe, A. & Mow, V. C. Chondrocyte deformation and local tissue strain in articular cartilage: A confocal microscopy study. *J. Orthop. Res.* **13,** 410–421 (1995).

46. Upton, M. L., Gilchrist, C. L., Guilak, F. & Setton, L. A. Transfer of Macroscale Tissue Strain to Microscale Cell Regions in the Deformed Meniscus. *Biophys. J.* **95,** 2116–2124 (2008).

47. Moo, E. K. *et al.* The Properties of Chondrocyte Membrane Reservoirs and Their Role in Impact-Induced Cell Death. *Biophys. J.* **105,** 1590–1600 (2013).

48. Alexander, P. G. *et al.* Development of a Spring-Loaded Impact Device to Deliver Injurious Mechanical Impacts to the Articular Cartilage Surface. *Cartilage* **4,** 52–62 (2013).

49. Buckley, M. R., Bergou, A. J., Fouchard, J., Bonassar, L. J. & Cohen, I. High-resolution spatial mapping of shear properties in cartilage. *J. Biomech.* **43,** 796–800 (2010).

50. Chen, C.-T. *et al.* Chondrocyte necrosis and apoptosis in impact damaged articular cartilage. *J. Orthop. Res.* **19,** 703–711 (2001).

51. Häuselmann, H. J. *et al.* The superficial layer of human articular cartilage is more susceptible to interleukin-1–induced damage than the deeper layers. *Arthritis Rheum.* **39,** 478–488 (1996).

52. Chahine, N. O., Wang, C. C.-B., Hung, C. T. & Ateshian, G. A. Anisotropic strain-dependent material properties of bovine articular cartilage in the transitional range from tension to compression. *J. Biomech.* **37,** 1251–1261 (2004).

53. Julkunen, P., Kiviranta, P., Wilson, W., Jurvelin, J. S. & Korhonen, R. K. Characterization of articular cartilage by combining microscopic analysis with a fibril-reinforced finite-element model. *J. Biomech.* **40,** 1862–1870 (2007).

54. Chahine, N. O., Ateshian, G. A. & Hung, C. T. The effect of finite compressive strain on chondrocyte viability in statically loaded bovine articular cartilage. *Biomech. Model. Mechanobiol.* **6,** 103–111 (2007).

55. Chen, C.-T., Bhargava, M., Lin, P. M. & Torzilli, P. A. Time, stress, and location dependent chondrocyte death and collagen damage in cyclically loaded articular cartilage. *J. Orthop. Res.* **21,** 888–898 (2003).

56. Levin, A. S., Chen, C.-T. C. & Torzilli, P. A. Effect of tissue maturity on cell viability in load-injured articular cartilage explants. *Osteoarthritis Cartilage* **13,** 488–496 (2005).

57. Novakofski, K. D. *et al.* Identification of cartilage injury using quantitative multiphoton microscopy. *Osteoarthritis Cartilage* **22,** 355–362 (2014).

58. Quinn, T. M., Allen, R. G., Schalet, B. J., Perumbuli, P. & Hunziker, E. B. Matrix and cell injury due to sub-impact loading of adult bovine articular cartilage explants: effects of strain rate and peak stress. *J. Orthop. Res.* **19,** 242–249 (2001).

59. Federico, S., Grillo, A., La Rosa, G., Giaquinta, G. & Herzog, W. A transversely isotropic, transversely homogeneous microstructural-statistical model of articular cartilage. *J. Biomech.* **38,** 2008–2018 (2005).

60. Li, L., Shirazi-Adl, A. & Buschmann, M. D. Investigation of mechanical behavior of articular cartilage by fibril reinforced poroelastic models. *Biorheology* **40,** 227–233 (2003).

61. Wang, C. C.-B., Hung, C. T. & Mow, V. C. An analysis of the effects of depth-dependent aggregate modulus on articular cartilage stress-relaxation behavior in compression. *J. Biomech.* **34,** 75–84 (2001).

62. Wilson, W., van Donkelaar, C. C., van Rietbergen, R. & Huiskes, R. The role of computational models in the search for the mechanical behavior and damage mechanisms of articular cartilage. *Med. Eng. Phys.* **27,** 810–826 (2005).

63. Del Carlo, M. & Loeser, R. F. Cell death in osteoarthritis. *Curr. Rheumatol. Rep.* **10,** 37–42 (2008).

64. D’lima, D. D., Hashimoto, S., Chen, P. C., Colwell, C. W. & Lotz, M. K. Human chondrocyte apoptosis in response to mechanical injury. *Osteoarthritis Cartilage* **9,** 712–719 (2001).

65. Kurz, B. *et al.* Influence of tissue maturation and antioxidants on the apoptotic response of articular cartilage after injurious compression. *Arthritis Rheum.* **50,** 123–130 (2004).

66. Li, Y. *et al.* Moderate dynamic compression inhibits pro-catabolic response of cartilage to mechanical injury, tumor necrosis factor-α and interleukin-6, but accentuates degradation above a strain threshold. *Osteoarthritis Cartilage* **21,** 1933–1941 (2013).

67. Rolauffs, B. *et al.* Stress-vs-time signals allow the prediction of structurally catastrophic events during fracturing of immature cartilage and predetermine the biomechanical, biochemical, and structural impairment. *J. Struct. Biol.* **183,** 501–511 (2013).

68. Jeffrey, J. E. & Aspden, R. M. The Biophysical Effects of a Single Impact Load on Human and Bovine Articular Cartilage. *Proc. Inst. Mech. Eng. [H]* **220,** 677–686 (2006).

69. Heiner, A. D. *et al.* Cartilage-on-cartilage versus metal-on-cartilage impact characteristics and responses. *J. Orthop. Res.* **31,** 887–893 (2013).

70. Mow, V. C. & Guo, X. E. Mechano-electrochemical properties of articular cartilage: Their inhomogeneities and anisotropies. *Annu. Rev. Biomed. Eng.* **4,** 175–209 (2002).

71. Chen, C.-T., Burton-Wurster, N., Lust, G., Bank, R. A. & Tekoppele, J. M. Compositional and metabolic changes in damaged cartilage are peak-stress, stress-rate, and loading-duration dependent. *J. Orthop. Res.* **17,** 870–879 (1999).

72. Ewers, B. J., Dvoracek-Driksna, D., Orth, M. W. & Haut, R. C. The extent of matrix damage and chondrocyte death in mechanically traumatized articular cartilage explants depends on rate of loading. *J. Orthop. Res.* **19,** 779–784 (2001).

73. Huser, C. A. M. & Davies, M. E. Validation of an in vitro single-impact load model of the initiation of osteoarthritis-like changes in articular cartilage. *J. Orthop. Res.* **24,** 725–732 (2006).

74. Torzilli, P. A., Grigiene, R., Borrelli, J., J. & Helfet, D. L. Effect of Impact Load on Articular Cartilage: Cell Metabolism and Viability, and Matrix Water Content. *J. Biomech. Eng.* **121,** 433–441 (1999).

75. Haut, R. C., Ide, T. M. & De Camp, C. E. Mechanical Responses of the Rabbit Patello-Femoral Joint to Blunt Impact. *J. Biomech. Eng.* **117,** 402–408 (1995).

76. Natoli, R. M., Scott, C. C. & Athanasiou, K. A. Temporal Effects of Impact on Articular Cartilage Cell Death, Gene Expression, Matrix Biochemistry, and Biomechanics. *Ann. Biomed. Eng.* **36,** 780–792 (2008).

77. Morel, V. & Quinn, T. M. Cartilage injury by ramp compression near the gel diffusion rate. *J. Orthop. Res.* **22,** 145–151 (2004).

78. Stolberg-Stolberg, J. A. *et al.* Effects of cartilage impact with and without fracture on chondrocyte viability and the release of inflammatory markers. *J. Orthop. Res.* **31,** 1283–1292 (2013).

79. Poole, C. A. *et al.* Detection of Viable and Non-Viable Cells in Connective Tissue Explants Using the Fixable Fluoroprobes 5-Chloromethylfluorescein Diacetate and Ethidium Homodimer-1. *Connect. Tissue Res.* **33,** 233–241 (1996).

80. Grogan, S. P. *et al.* In vitro model for the study of necrosis and apoptosis in native cartilage. *J. Pathol.* **198,** 5–13 (2002).

81. Kühn, K., D'Lima, D. D., Hashimoto, S. & Lotz, M. Cell death in cartilage. *Osteoarthritis Cartilage* **12,** 1–16 (2004).

82. Cheng, D. S. & Visco, C. J. Pharmaceutical Therapy for Osteoarthritis. *PM&R* **4,** S82–S88 (2012).

83. Gallagher, B. *et al.* Chondroprotection and the Prevention of Osteoarthritis Progression of the Knee: A Systematic Review of Treatment Agents. *Am. J. Sports Med.* **43,** 734–744 (2015).

84. Bartell, L. R., Fortier, L. A., Bonassar, L. J. & Cohen, I. Measuring microscale strain fields in articular cartilage during rapid impact reveals thresholds for chondrocyte death and a protective role for the superficial layer. *J. Biomech.* **48,** 3440–3446 (2015).

85. Blanco, F. J., Rego, I. & Ruiz-Romero, C. The role of mitochondria in osteoarthritis. *Nat. Rev. Rheumatol.* **7,** 161–169 (2011).

86. Terkeltaub, R., Johnson, K., Murphy, A. & Ghosh, S. Invited review: the mitochondrion in osteoarthritis. *Mitochondrion* **1,** 301–319 (2002).

87. Goetz, J. E. *et al.* Time-dependent loss of mitochondrial function precedes progressive histologic cartilage degeneration in a rabbit meniscal destabilization model. *J. Orthop. Res.* n/a-n/a (2016). doi:10.1002/jor.23327

88. Koike, M. *et al.* Mechanical overloading causes mitochondrial superoxide and SOD2 imbalance in chondrocytes resulting in cartilage degeneration. *Sci. Rep.* **5,** (2015).

89. Delco Michelle L., Bonnevie Edward D., Szeto Hazel S., Bonassar Lawrence J. & Fortier Lisa A. Mitoprotective therapy preserves chondrocyte viability and prevents cartilage degeneration in an ex vivo model of posttraumatic osteoarthritis. *J. Orthop. Res.* **0,** (2018).

90. Huser, C. a. M. & Davies, M. E. Calcium signaling leads to mitochondrial depolarization in impact-induced chondrocyte death in equine articular cartilage explants. *Arthritis Rheum.* **56,** 2322–2334 (2007).

91. Delco, M. L., Bonnevie, E. D., Bonassar, L. J. & Fortier, L. A. Mitochondrial dysfunction is an acute response of articular chondrocytes to mechanical injury. *J. Orthop. Res.* (2017). doi:10.1002/jor.23651

92. Brouillette, M. J. *et al.* Strain-dependent oxidant release in articular cartilage originates from mitochondria. *Biomech. Model. Mechanobiol.* **13,** 565–572 (2014).

93. Knight, M. M. *et al.* Chondrocyte Deformation Induces Mitochondrial Distortion and Heterogeneous Intracellular Strain Fields. *Biomech. Model. Mechanobiol.* **5,** 180 (2006).

94. Szafranski, J. D. *et al.* Chondrocyte mechanotransduction: effects of compression on deformation of intracellular organelles and relevance to cellular biosynthesis. *Osteoarthritis Cartilage* **12,** 937–946 (2004).

95. Li, D., Wang, W. & Xie, G. Reactive Oxygen Species: The 2-Edged Sword of Osteoarthritis. *Am. J. Med. Sci.* **344,** 486–490 (2012).

96. Bonnevie, E. D. *et al.* Microscale Frictional Strains Determine Chondrocyte Fate in Loaded Cartilage. *J. Biomech.* (2018). doi:10.1016/j.jbiomech.2018.04.020

97. Chan, D. C. Mitochondrial Fusion and Fission in Mammals. *Annu. Rev. Cell Dev. Biol.* **22,** 79–99 (2006).

98. Szeto, H. H. First-in-class cardiolipin-protective compound as a therapeutic agent to restore mitochondrial bioenergetics. *Br. J. Pharmacol.* **171,** 2029–2050 (2014).

99. Birk, A. V. *et al.* The Mitochondrial-Targeted Compound SS-31 Re-Energizes Ischemic Mitochondria by Interacting with Cardiolipin. *J. Am. Soc. Nephrol.* **24,** 1250–1261 (2013).

100. Gibson, C. M. *et al.* EMBRACE STEMI study: a Phase 2a trial to evaluate the safety, tolerability, and efficacy of intravenous MTP-131 on reperfusion injury in patients undergoing primary percutaneous coronary intervention. *Eur. Heart J.* **37,** 1296–1303 (2016).

101. Saad, A. *et al.* Phase 2a Clinical Trial of Mitochondrial Protection (Elamipretide) During Stent Revascularization in Patients With Atherosclerotic Renal Artery Stenosis. *Circ. Cardiovasc. Interv.* **10,** (2017).

102. Schinagl, R. M., Gurskis, D., Chen, A. C. & Sah, R. L. Depth-dependent confined compression modulus of full-thickness bovine articular cartilage. *J. Orthop. Res.* **15,** 499–506 (1997).

103. Liesa, M., Palacín, M. & Zorzano, A. Mitochondrial Dynamics in Mammalian Health and Disease. *Physiol. Rev.* **89,** 799–845 (2009).

104. Henak, C. R., Bartell, L. R., Cohen, I. & Bonassar, L. J. Multi-scale strain as a predictor of impact-induced fissuring in articular cartilage. *J. Biomech. Eng.* (2016). doi:10.1115/1.4034994

105. Blaber, J., Adair, B. & Antoniou, A. Ncorr: Open-Source 2D Digital Image Correlation Matlab Software. *Exp. Mech.* **55,** 1105–1122 (2015).

106. Miyazono, Y. *et al.* Uncoupled mitochondria quickly shorten along their long axis to form indented spheroids, instead of rings, in a fission-independent manner. *Sci. Rep.* **8,** 350 (2018).

107. Ishihara, N., Jofuku, A., Eura, Y. & Mihara, K. Regulation of mitochondrial morphology by membrane potential, and DRP1-dependent division and FZO1-dependent fusion reaction in mammalian cells. *Biochem. Biophys. Res. Commun.* **301,** 891–898 (2003).

108. Cogliati, S., Enriquez, J. A. & Scorrano, L. Mitochondrial Cristae: Where Beauty Meets Functionality. *Trends Biochem. Sci.* **41,** 261–273 (2016).

109. Szeto, H. H. Mitochondria-targeted peptide antioxidants: Novel neuroprotective agents. *AAPS J.* **8,** E521–E531 (2006).

110. Zhao, K., Luo, G., Giannelli, S. & Szeto, H. H. Mitochondria-targeted peptide prevents mitochondrial depolarization and apoptosis induced by tert-butyl hydroperoxide in neuronal cell lines. *Biochem. Pharmacol.* **70,** 1796–1806 (2005).

111. PANG, Y., WANG, C. & YU, L. Mitochondria-Targeted Antioxidant SS-31 is a Potential Novel Ophthalmic Medication for Neuroprotection in Glaucoma. *Med. Hypothesis Discov. Innov. Ophthalmol.* **4,** 120–126 (2015).

112. Clements, K. M., Burton-Wurster, N. & Lust, G. The spread of cell death from impact damaged cartilage: lack of evidence for the role of nitric oxide and caspases11Source of support: NIH Grant No. R01 AR47558. *Osteoarthritis Cartilage* **12,** 577–585 (2004).

113. Bartell, L. R., Bonassar, L. J. & Cohen, I. A watershed-based algorithm to segment and classify cells in fluorescence microscopy images. *ArXiv170600815 Cs* (2017).

114. Daley, R. *Atmospheric Data Analysis*. (Cambridge University Press, 1992).

115. Bauer, M. & Jackson, R. W. Chondral lesions of the femoral condyles: A system of arthroscopic classification. *Arthrosc. J. Arthrosc. Relat. Surg.* **4,** 97–102 (1988).

116. Curl, W. W. *et al.* Cartilage injuries: A review of 31,516 knee arthroscopies. *Arthrosc. J. Arthrosc. Relat. Surg.* **13,** 456–460 (1997).

117. Outerbridge, R. E. The Etiology of Chondromalacia Patellae. *Bone Jt. J.* **43-B,** 752–757 (1961).

118. Pritzker, K. P. H. *et al.* Osteoarthritis cartilage histopathology: grading and staging. *Osteoarthritis Cartilage* **14,** 13–29 (2006).

119. Lewis, J. L. *et al.* Cell death after cartilage impact occurs around matrix cracks. *J. Orthop. Res.* **21,** 881–887 (2003).

120. Mow, V. C., Kuei, S. C., Lai, W. M. & Armstrong, C. G. Biphasic Creep and Stress Relaxation of Articular Cartilage in Compression: Theory and Experiments. *J. Biomech. Eng.* **102,** 73–84 (1980).

121. Morel, V. & Quinn, T. M. Cartilage injury by ramp compression near the gel diffusion rate. *J. Orthop. Res.* **22,** 145–151 (2004).

122. Ahsan, T. & Sah, R. L. Biomechanics of integrative cartilage repair. *Osteoarthritis Cartilage* **7,** 29–40 (1999).

123. Chin-Purcell, M. V. & Lewis, J. L. Fracture of Articular Cartilage. *J. Biomech. Eng.* **118,** 545–556 (1996).

124. Oyen-Tiesma, M. & Cook, R. F. Technique for estimating fracture resistance of cultured neocartilage. *J. Mater. Sci. Mater. Med.* **12,** 327–332 (2001).

125. Taylor, D., O'Mara, N., Ryan, E., Takaza, M. & Simms, C. The fracture toughness of soft tissues. *J. Mech. Behav. Biomed. Mater.* **6,** 139–147 (2012).

126. Hui, C.-Y., A, J., Bennison, S. J. & Londono, J. D. Crack blunting and the strength of soft elastic solids. *Proc. R. Soc. Lond. Math. Phys. Eng. Sci.* **459,** 1489–1516 (2003).

127. Stok, K. & Oloyede, A. Conceptual fracture parameters for articular cartilage. *Clin. Biomech.* **22,** 725–735 (2007).

128. Johnson, K. L. *Contact Mechanics*. (Cambridge University Press, 1987).

129. Silverberg, J. L., Dillavou, S., Bonassar, L. & Cohen, I. Anatomic variation of depth-dependent mechanical properties in neonatal bovine articular cartilage. *J. Orthop. Res.* **31,** 686–691 (2013).

130. Rolauffs, B. *et al.* Vulnerability of the superficial zone of immature articular cartilage to compressive injury. *Arthritis Rheum.* **62,** 3016–3027 (2010).

131. Lewis, J. L. & Johnson, S. L. Collagen architecture and failure processes in bovine patellar cartilage. *J. Anat.* **199,** 483–492 (2001).

132. Simha, N. K., Carlson, C. S. & Lewis, J. L. Evaluation of fracture toughness of cartilage by micropenetration. *J. Mater. Sci. Mater. Med.* **15,** 631–639 (2003).

133. Barthelat, F., Yin, Z. & Buehler, M. J. Structure and mechanics of interfaces in biological materials. *Nat. Rev. Mater.* **1,** 16007 (2016).

134. Dunlop, J. W. C., Weinkamer, R. & Fratzl, P. Artful interfaces within biological materials. *Mater. Today* **14,** 70–78 (2011).

135. Men, Y., Jiang, Y., Chen, L., Zhang, C. & Ye, J. On mechanical mechanism of damage evolution in articular cartilage. *Mater. Sci. Eng. C* **78,** 79–87 (2017).

136. Thambyah, A., Zhang, G., Kim, W. & Broom, N. D. Impact induced failure of cartilage-on-bone following creep loading: A microstructural and fracture mechanics study. *J. Mech. Behav. Biomed. Mater.* **14,** 239–247 (2012).

137. Bouklas, N., Landis, C. M. & Huang, R. Effect of Solvent Diffusion on Crack-Tip Fields and Driving Force for Fracture of Hydrogels. *J. Appl. Mech.* **82,** 081007-081007–16 (2015).

138. Fakhouri, S., B. Hutchens, S. & J. Crosby, A. Puncture mechanics of soft solids. *Soft Matter* **11,** 4723–4730 (2015).

139. Gong, J. P. Why are double network hydrogels so tough? *Soft Matter* **6,** 2583–2590 (2010).

140. Long, R. & Hui, C.-Y. Fracture toughness of hydrogels: measurement and interpretation. *Soft Matter* **12,** 8069–8086 (2016).

141. Lake, G. J. & Yeoh, O. H. Measurement of rubber cutting resistance in the absence of friction. *Int. J. Fract.* **14,** 509–526 (1978).

142. Bank, R. A., Bayliss, M. T., Lafeber, F. P. J. G., Maroudas, A. & Tekoppele, J. M. Ageing and zonal variation in post-translational modification of collagen in normal human articular cartilage: The age-related increase in non-enzymatic glycation affects biomechanical properties of cartilage. *Biochem. J.* **330,** 345–351 (1998).

143. Brown, C. P., Nguyen, T. C., Moody, H. R., Crawford, R. W. & Oloyede, A. Assessment of common hyperelastic constitutive equations for describing normal and osteoarthritic articular cartilage. *Proc. Inst. Mech. Eng. [H]* **223,** 643–652 (2009).

144. Holzapfel, G. A. Nonlinear solid mechanics: a continuum approach for engineering. (Wiley, 2000).

145. Kinloch, A. J. *et al.* The effect of silica nano particles and rubber particles on the toughness of multiphase thermosetting epoxy polymers. *J. Mater. Sci.* **40,** 5083–5086 (2005).

146. Ragosta, G., Abbate, M., Musto, P., Scarinzi, G. & Mascia, L. Epoxy-silica particulate nanocomposites: Chemical interactions, reinforcement and fracture toughness. *Polymer* **46,** 10506–10516 (2005).

147. Zhang, H., Zhang, Z., Friedrich, K. & Eger, C. Property improvements of in situ epoxy nanocomposites with reduced interparticle distance at high nanosilica content. *Acta Mater.* **54,** 1833–1842 (2006).

148. Hsieh, T. H. *et al.* The toughness of epoxy polymers and fibre composites modified with rubber microparticles and silica nanoparticles. *J. Mater. Sci.* **45,** 1193–1210 (2010).

149. Ritter, J. E., Sioui, D. R. & Lardner, T. J. Indentation behavior of polymer coatings on glass. *Polym. Eng. Sci.* **32,** 1366–1371 (1992).

150. Ritter, J. E., Lardner, T. J., Rosenfeld, L. & Lin, M. R. Measurement of adhesion of thin polymer coatings by indentation. *J. Appl. Phys.* **66,** 3626–3634 (1989).

151. Chai, H., Lawn, B. & Wuttiphan, S. Fracture modes in brittle coatings with large interlayer modulus mismatch. *J. Mater. Res.* **14,** 3805–3817 (1999).

152. Bull, S. j. A simple method for the assessment of the contact modulus for coated systems. *Philos. Mag.* **95,** 1907–1927 (2015).

153. Lee, D., Rahman, M. M., Zhou, Y. & Ryu, S. Three-Dimensional Confocal Microscopy Indentation Method for Hydrogel Elasticity Measurement. *Langmuir* **31,** 9684–9693 (2015).

154. King, R. B. Elastic analysis of some punch problems for a layered medium. *Int. J. Solids Struct.* **23,** 1657–1664 (1987).

155. Ritter, J. E. & Rosenfeld, L. G. Use of the indentation technique for studying delamination of polymeric coatings. *J. Adhes. Sci. Technol.* **4,** 551–571 (1990).

156. Bull, S. J. Nanoindentation of coatings. *J. Phys. Appl. Phys.* **38,** R393 (2005).

157. Li, M., Palacio, M. L., Barry Carter, C. & Gerberich, W. W. Indentation deformation and fracture of thin polystyrene films. *Thin Solid Films* **416,** 174–183 (2002).

158. Lin, N. Y. C. *et al.* A multi-axis confocal rheoscope for studying shear flow of structured fluids. *Rev. Sci. Instrum.* **85,** 033905 (2014).

159. Crocker, J. C. & Grier, D. G. Methods of Digital Video Microscopy for Colloidal Studies. *J. Colloid Interface Sci.* **179,** 298–310 (1996).

160. Bartell, L. Barnes interpolation. *MATLAB Central File Exchange* (2016). Available at: www.mathworks.com/matlabcentral/fileexchange/58937-barnes-interpolation--barnes-objective-analysis-. (Accessed: 20th September 2016)

161. Liu, W. & Long, R. Constructing Continuous Strain and Stress Fields From Spatially Discrete Displacement Data in Soft Materials. *J. Appl. Mech.-Trans. Asme* **83,** 011006 (2016).

162. Lee, J. & Yee, A. F. Fracture of glass bead/epoxy composites: on micro-mechanical deformations. *Polymer* **41,** 8363–8373 (2000).

163. Gossweiler, G. R. *et al.* Mechanochemical Activation of Covalent Bonds in Polymers with Full and Repeatable Macroscopic Shape Recovery. *ACS Macro Lett.* **3,** 216–219 (2014).

164. Celestine, A.-D. N. *et al.* Fracture-induced activation in mechanophore-linked, rubber toughened PMMA. *Polymer* **55,** 4164–4171 (2014).

165. Garrido, C. P. *et al.* Anti-apoptotic treatments prevent cartilage degradation after acute trauma to human ankle cartilage. *Osteoarthritis Cartilage* **17,** 1244–1251 (2009).

166. Bartell, L. R., Xu, M. C., Bonassar, L. J. & Cohen, I. Local and global measurements show that damage initiation in articular cartilage is inhibited by the surface layer and has significant rate dependence. *J. Biomech.* **0,** (2018).

167. Stok, K. & Oloyede, A. A Qualitative Analysis of Crack Propagation in Articular Cartilage at Varying Rates of Tensile Loading. *Connect. Tissue Res.* **44,** 109–120 (2003).

168. Sindermann, A., Bartell, L., Bonassar, L., Cohen, I. & Das, M. Nonlinear response and crack propagation in Articular Cartilage modeled as a biopolymer double network. in R16.014 (2017).

169. Griffin, D. J. *et al.* Effects of enzymatic treatments on the depth-dependent viscoelastic shear properties of articular cartilage. *J. Orthop. Res.* **32,** 1652–1657 (2014).

170. June, R. K. & Fyhrie, D. P. Enzymatic digestion of articular cartilage results in viscoelasticity changes that are consistent with polymer dynamics mechanisms. *Biomed. Eng. OnLine* **8,** 32 (2009).

---

[i] Initial progress on an impactor redesign has been conducted by Shannon Y. Zhou as part of her Senior Design Project for MAE 4691. This design work was conducted in collaboration with Lena R. Bartell, Itai Cohen, and Lawrence J. Bonassar during Zhou's Spring 2016 semester at Cornell University. A full report may be available by contacting Lawrence J. Bonassar.